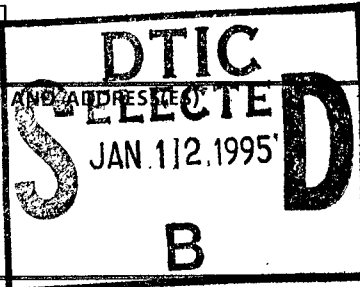
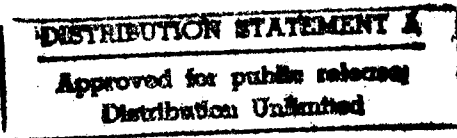


JRC-36-94

ULTRASONIC STUDIES OF LIQUID/SOLID
SEISMOACOUSTIC WAVE PHENOMENA

Jacques R. Chamuel
November 1994

19950109 162

REPORT DOCUMENTATION PAGE			Form Approved OMB No. 0704-0188	
Public reporting burden for this collection of information is estimated to average 1 hour per response, including the time for reviewing instructions, searching existing data sources, gathering and maintaining the data needed, and completing and reviewing the collection of information. Send comments regarding this burden estimate or any other aspect of this collection of information, including suggestions for reducing this burden, to Washington Headquarters Services, Directorate for Information Operations and Reports, 1215 Jefferson Davis Highway, Suite 1204, Arlington, VA 22202-4302, and to the Office of Management and Budget, Paperwork Reduction Project (0704-0188), Washington, DC 20503.				
1. AGENCY USE ONLY (Leave blank)	2. REPORT DATE November 1994	3. REPORT TYPE AND DATES COVERED Final Report Apr 92-Oct 94		
4. TITLE AND SUBTITLE Ultrasonic Studies of Liquid/Solid Seismoacoustic Wave Phenomena			5. FUNDING NUMBERS C - N00014-92-C-0028	
6. AUTHOR(S) Jacques R. Chamuel				
7. PERFORMING ORGANIZATION NAME(S) AND ADDRESS(ES) Sonoquest Advanced Ultrasonics Research P. O. Box 81153 Wellesley Hills, MA 02181-0001			8. PERFORMING ORGANIZATION REPORT NUMBER JRC-36-94	
9. SPONSORING/MONITORING AGENCY NAME(S) AND ADDRESS(ES) Office of Naval Research			10. SPONSORING/MONITORING AGENCY REPORT NUMBER	
				
11. SUPPLEMENTARY NOTES ONR POC - Thomas B. Curtin (703) 696-4119				
12a. DISTRIBUTION/AVAILABILITY STATEMENT Approved for Public Release			12b. DISTRIBUTION CODE Distribution Unlimited	
				
13. ABSTRACT (Maximum 200 words) New ultrasonic modeling findings are presented contributing to ten fundamental problems related to low-frequency seismoacoustic wave phenomena resulting from the interaction of underwater acoustic waves with heterogeneous elastic boundaries such as the ice cover and/or ocean bottom. The results are described in ten independent sections covering the following problems: 1) backscattering of Scholte waves and grazing underwater acoustic waves by a trench at a liquid/solid interface, 2) explanation for observed underwater acoustic backscatter from the Canada Basin near 73.2°N, 139°W where recent bathymetric charts do not reveal the existence of large bathymetric highs nearby, 3) effect of a thin low-velocity layer underneath a floating plate on flexural wave dispersion, 4) effect of viscous waves from suspended particles in a thin layer under sea ice on low-frequency underwater acoustic wave reflectivity, 5) comparison of experimental and theoretical results on the dispersion of antisymmetric edge waves along apex of truncated elastic wedge, 6) wave propagation along apex of free and immersed elastic wedge with range-dependent apex angle and cross section, 7) shear wave coupling to ice cores, 8) ultrasonic characterization of sea ice cores, 9) monostatic seismic profiling using scattering from 45° oblique cylindrical hole in ice plate using one compressional transducer, and 10) sea ice finger-raftering and ice thickness.				
14. SUBJECT TERMS Underwater acoustics, sea ice, flexural waves, wedge waves, Canada Basin bathymetry, Scholte waves, seismic profiling			15. NUMBER OF PAGES 74	
			16. PRICE CODE	
17. SECURITY CLASSIFICATION OF REPORT Unclassified	18. SECURITY CLASSIFICATION OF THIS PAGE Unclassified	19. SECURITY CLASSIFICATION OF ABSTRACT Unclassified	20. LIMITATION OF ABSTRACT	

GENERAL INSTRUCTIONS FOR COMPLETING SF 298

The Report Documentation Page (RDP) is used in announcing and cataloging reports. It is important that this information be consistent with the rest of the report, particularly the cover and title page. Instructions for filling in each block of the form follow. It is important to *stay within the lines* to meet *optical scanning requirements*.

Block 1. Agency Use Only (Leave blank).

Block 2. Report Date. Full publication date including day, month, and year, if available (e.g. 1 Jan 88). Must cite at least the year.

Block 3. Type of Report and Dates Covered. State whether report is interim, final, etc. If applicable, enter inclusive report dates (e.g. 10 Jun 87 - 30 Jun 88).

Block 4. Title and Subtitle. A title is taken from the part of the report that provides the most meaningful and complete information. When a report is prepared in more than one volume, repeat the primary title, add volume number, and include subtitle for the specific volume. On classified documents enter the title classification in parentheses.

Block 5. Funding Numbers. To include contract and grant numbers; may include program element number(s), project number(s), task number(s), and work unit number(s). Use the following labels:

C - Contract	PR - Project
G - Grant	TA - Task
PE - Program Element	WU - Work Unit Accession No.

Block 6. Author(s). Name(s) of person(s) responsible for writing the report, performing the research, or credited with the content of the report. If editor or compiler, this should follow the name(s).

Block 7. Performing Organization Name(s) and Address(es). Self-explanatory.

Block 8. Performing Organization Report Number. Enter the unique alphanumeric report number(s) assigned by the organization performing the report.

Block 9. Sponsoring/Monitoring Agency Name(s) and Address(es). Self-explanatory.

Block 10. Sponsoring/Monitoring Agency Report Number. (If known)

Block 11. Supplementary Notes. Enter information not included elsewhere such as: Prepared in cooperation with...; Trans. of...; To be published in... When a report is revised, include a statement whether the new report supersedes or supplements the older report.

Block 12a. Distribution/Availability Statement. Denotes public availability or limitations. Cite any availability to the public. Enter additional limitations or special markings in all capitals (e.g. NOFORN, REL, ITAR)

DOD - See DoDD 5230.24, "Distribution Statements on Technical Documents."

DOE - See authorities.

NASA - See Handbook NHB 2200.2.

NTIS - Leave blank.

Block 12b. Distribution Code.

DOD - Leave blank.

DOE - Enter DOE distribution categories from the Standard Distribution for Unclassified Scientific and Technical Reports.

NASA - Leave blank.

NTIS - Leave blank.

Block 13. Abstract. Include a brief (*Maximum 200 words*) factual summary of the most significant information contained in the report.

Block 14. Subject Terms. Keywords or phrases identifying major subjects in the report.

Block 15. Number of Pages. Enter the total number of pages.

Block 16. Price Code. Enter appropriate price code (*NTIS only*).

Blocks 17. - 19. Security Classifications. Self-explanatory. Enter U.S. Security Classification in accordance with U.S. Security Regulations (i.e., UNCLASSIFIED). If form contains classified information, stamp classification on the top and bottom of the page.

Block 20. Limitation of Abstract. This block must be completed to assign a limitation to the abstract. Enter either UL (unlimited) or SAR (same as report). An entry in this block is necessary if the abstract is to be limited. If blank, the abstract is assumed to be unlimited.

National Technical Information Service
Accession Report No.

JRC-36-94

ULTRASONIC STUDIES OF LIQUID/SOLID
SEISMOACOUSTIC WAVE PHENOMENA

Jacques R. Chamuel
November 1994

Sonoquest Advanced Ultrasonics Research
P.O. Box 81153, Wellesley Hills, Massachusetts 02181-0001, USA

© Sonoquest Advanced Ultrasonics Research, 1994

This report is available from National Technical Information Service, U.S. Dept. of Commerce, 5285 Port
Royal Road, Springfield, VA 22161 Tel. (703) 487-4650

ABSTRACT

New ultrasonic modeling findings are presented contributing to ten fundamental problems related to low-frequency seismoacoustic wave phenomena resulting from the interaction of underwater acoustic waves with heterogeneous elastic boundaries such as the ice cover and/or ocean bottom. The results are described in ten independent sections covering the following problems: 1) backscattering of Scholte waves and grazing underwater acoustic waves by a trench at a liquid/solid interface, 2) explanation for observed underwater acoustic backscatter from the Canada Basin near 73.2°N, 139°W where recent bathymetric charts do not reveal the existence of large bathymetric highs nearby, 3) effect of a thin low-velocity layer underneath a floating plate on flexural wave dispersion, 4) effect of viscous waves from suspended particles in a thin layer under sea ice on low-frequency underwater acoustic wave reflectivity, 5) comparison of experimental and theoretical results on the dispersion of antisymmetric edge waves along apex of truncated elastic wedge, 6) wave propagation along apex of free and immersed elastic wedge with range-dependent apex angle and cross section, 7) shear wave coupling to ice cores, 8) ultrasonic characterization of sea ice cores, 9) monostatic seismic profiling using scattering from 45° oblique cylindrical hole in ice plate using one compressional transducer, and 10) sea ice finger-raftering and ice thickness.

Accession For	
NTIS GRA&I	<input checked="" type="checkbox"/>
DTIC TAB	<input type="checkbox"/>
Unannounced	<input type="checkbox"/>
Justification	
By	
Distribution/	
Availability Codes	
Dist	Avail and/or Special
A-1	

ACKNOWLEDGEMENTS

The research presented in this report was sponsored by the U.S. Office of Naval Research (ONR) Code 322HL under Contract No. N00014-92-C-0028. The author is indebted to R. F. Obrochta and T. B. Curtin / ONR for making this research possible. The author would like to thank W. B. Tucker III / U. S. Army Cold Regions Research and Engineering Laboratory for providing ice core samples, T. B. Curtin for inspiring discussions on sea ice mechanics, I. Dyer / Massachusetts Institute of Technology for providing valuable references on backscattering of sound in the Arctic Ocean and bringing to my attention observed anomalous acoustic backscatter, N. Z. Cherkis / Naval Research Laboratory for contributing detailed bathymetric maps, and A. Grantz / U.S. Geological Survey for sharing helpful information on the bathymetry of the Canada Basin and providing critical ocean bottom seismic data.

TABLE OF CONTENTS

	Page
ABSTRACT	v
ACKNOWLEDGEMENTS	vi
TABLE OF CONTENTS	vii
1 BACKSCATTERING OF SCHOLTE WAVES AND GRAZING UNDERWATER ACOUSTIC WAVES BY A TRENCH AT A LIQUID/SOLID INTERFACE	1
2 EXPLANATION FOR ACOUSTIC BACKSCATTERING FROM CANADA BASIN NEAR 73.2°N, 139°W WHERE NO KNOWN BATHYMETRIC HIGHS EXIST	4
3 EFFECT OF A THIN LOW-VELOCITY LAYER UNDERNEATH A FLOATING PLATE ON FLEXURAL WAVE DISPERSION	12
4 EFFECT OF VISCOUS WAVES FROM SUSPENDED PARTICLES UNDER SEA ICE ON LOW-FREQUENCY ACOUSTIC WAVE REFLECTIVITY	21
5 DISPERSION OF ANTISYMMETRIC EDGE WAVES ALONG APEX OF TRUNCATED ELASTIC WEDGE	28
6 ELASTIC WEDGE WITH RANGE-DEPENDENT APEX ANGLE AND CROSS SECTION	
6.1 Range-Dependent Antisymmetric Edge Waves Along Curved Elastic Wedge with Variable Cross Section	37
6.2 Edge Waves Along Immersed Elastic Elliptical Wedge with Range- Dependent Apex Angle	45
7 SHEAR WAVE COUPLING TO ICE CORES	51
8 ULTRASONIC CHARACTERIZATION OF ARCTIC ICE CORES	53
9 SEISMIC PROFILING USING ONE COMPRESSIONAL TRANSDUCER AND MONOSTATIC SCATTERING FROM 45° OBLIQUE CYLINDRICAL HOLE	55
10 SEA ICE FINGER-RAFTING AND ICE THICKNESS	63
SUMMARY	69

Backscattering of Scholte Waves and Near-Grazing Underwater Acoustic Waves by a Trench at a Liquid/Solid Interface

Jacques R. Chamuel

Abstract— Ultrasonic modeling results are presented on backscattering of broadband pulsed Scholte waves and grazing underwater acoustic waves from a trench at a liquid/solid interface. The backscattered waves are characterized by interference of diffracted waves reflected from the trench bottom and the trailing steep side. The effects of trench width and depth are demonstrated.

I. INTRODUCTION

LABORATORY ultrasonic modeling results are presented on monostatic backscattering of pulsed Scholte waves (also known as Stoneley waves [1]) and near-grazing underwater acoustic waves from a trench at a liquid/solid interface to provide physical insight into seismoacoustic wave propagation in an ocean with range-dependent boundary topography [2]–[4]. The basic findings pertain to the general problem of wave propagation in waveguides with outward boundary deformations [4] such as in shallow water, boreholes with fractures, electromagnetic waveguides [5], and sound barriers [6]. References [7]–[9] provide other examples on the interaction of Scholte waves with topographic features.

II. RESULTS

Experimental studies were conducted on laboratory ultrasonic models of a trench at a liquid/solid interface using glass models immersed in water as shown in Fig. 1. The trench was modeled using a downstep followed by an upstep. The trench depth is denoted by h and its width d . Broadband pulsed ultrasonic waves were generated and detected using a 2.54 cm diameter 1 MHz compressional transducer connected to a Pulser Receiver Panametrics Model No. 5055PR. Scholte waves and near-grazing underwater acoustic waves were obtained by placing the transducer at the water/glass interface and orienting it to radiate horizontally parallel to the interface towards the trench. The described method of producing pulsed Scholte waves is practical for liquid/solid interfaces where most of the Scholte wave energy is in the liquid and the Scholte wave speed is only about 0.2% smaller than the liquid compressional wave speed. The model dimensions and results are given in terms of acoustic wavelength in the water at 1 MHz based on a compressional sound wave speed $c_w = 1466$

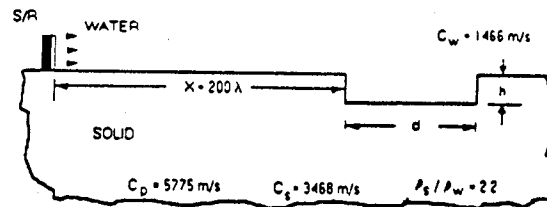


Fig. 1. A Schematic diagram of the experimental configuration showing trench model parameters and source/receiver transducer.

m/s. The glass density, compressional and shear wave speeds were 2.2×10^3 kg/m³, 5775 m/s, and 3468 m/s, respectively. The distance x between the transducer and the leading side of the trench was fixed at 200λ . The calculated Scholte wave speed for the water/glass model was $C_{Sch} = 1462$ m/s.

The waveform of backscattered waves received from a model with $d = 20\lambda$, and $h = 8.3\lambda$ is displayed in Fig. 2. The first received small pulse "A" is the reflected component from the leading steep side of the trench. The second large pulse "B" is the reflection from the trailing steep side of the trench. The third small pulse "C" is a backscattered component reflecting from both the trench horizontal bottom and trailing steep side. The relative amplitude of pulses B and C depends on d and h . Fig. 3(a) displays the measured relative amplitude of the backscattered waves plotted versus d/λ for three different values of h (3.9λ , 6.5λ and 8.3λ). No corrections were made on the amplitude of the backscattered waves to account for attenuation and geometrical spreading. Each of the three curves of Fig. 3(a) has an inflection. The inflection location moves to greater values of d/λ as the trench depth is increased. The inflection is caused by destructive interference between pulses B and C. The time delay between pulses B and C was calculated from the approximate expression:

$$T = 2(\sqrt{h^2 + 4d^2/9} + \sqrt{d^2/9 + h^2/4} - \sqrt{h^2/4 + d^2})/C_w \quad (1)$$

The first term in the numerator of (1) is the distance from "P1" the top corner of the leading side of the trench to "P2" the reflection point along the bottom of the trench. The second term is the distance from "P2" to "P3" the midpoint along the vertical trailing side of the trench. The third term is the distance from P1 to P3. Interference between pulses B and C occurs when T is less than the $2.4 \mu\text{s}$ duration of the pulsed waveform. Fig. 4(a) presents the calculated time delay between pulses B and C plotted versus d/λ for

Manuscript received March 22, 1994; revised and accepted July 18, 1994. This work was supported by the Office of Naval Research.

The author is with Sonoquest Advanced Ultrasonics Research, Wellesley Hills, MA 02181-0001 USA.

IEEE Log Number 9405240.

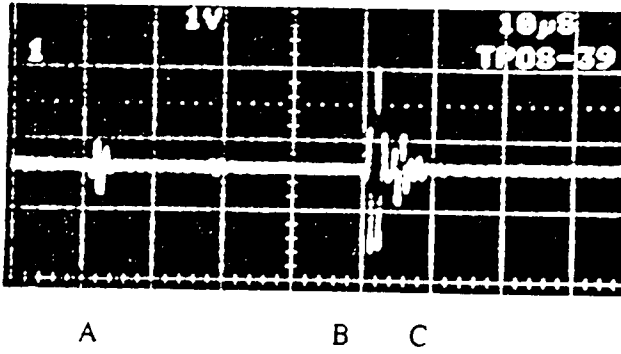


Fig. 2. Waveform of received backscattered waves with $d = 20\lambda$ and $h = 6.3\lambda$ obtained from contoured air/water/glass model.

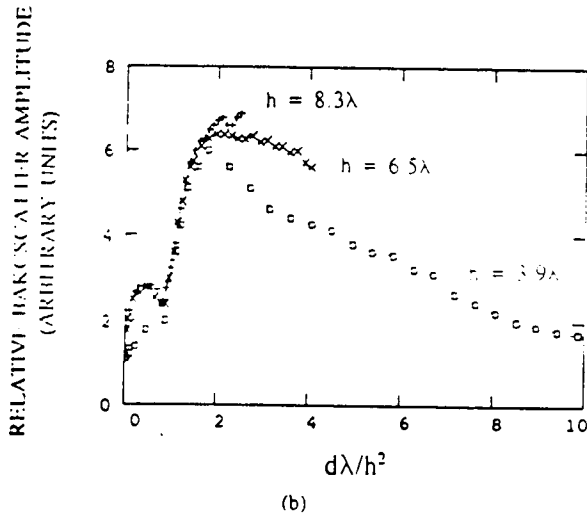
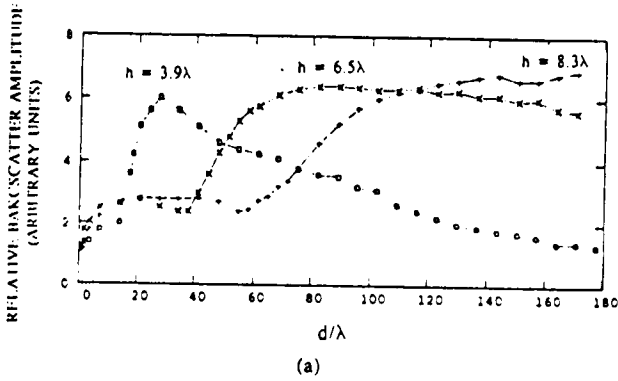


Fig. 3. Measured relative amplitude of received backscattered waves from trench plotted versus d/λ in (a) and plotted versus $d\lambda/h^2$ in (b). The results are not corrected for attenuation or geometrical spreading.

$h = 3.9\lambda, 6.5\lambda$ and 8.3λ . The intersection of each curve with the horizontal $2.4 \mu s$ line, representing the waveform duration, occurs at $d/\lambda = 12, 35,$ and 58 nearly matching the inflection locations shown in Fig. 3(a). The experimental backscatter amplitude results of Fig. 3(a) are replotted versus $d\lambda/h^2$ in Fig. 3(b) showing that the inflection occurs at about $d\lambda/h^2 = 0.9$ for all three curves. For the given range of parameters and for $T < 5 \mu s$, the three time delay curves of Fig. 4(a) become almost superimposed on each other when replotted versus $d\lambda/h^2$ as illustrated in Fig. 4(b).

The observed large backscattered waves are mainly due to having a penetrable elastic boundary that allows seismo-

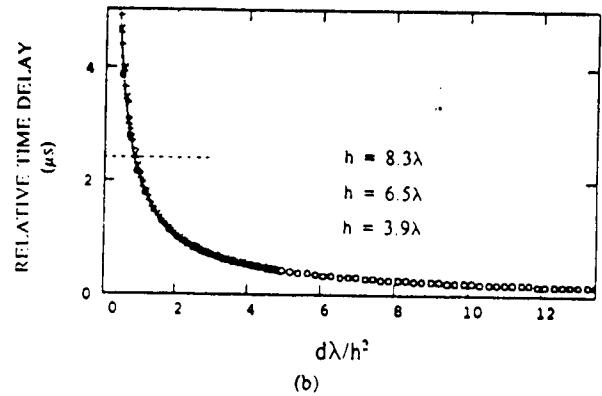
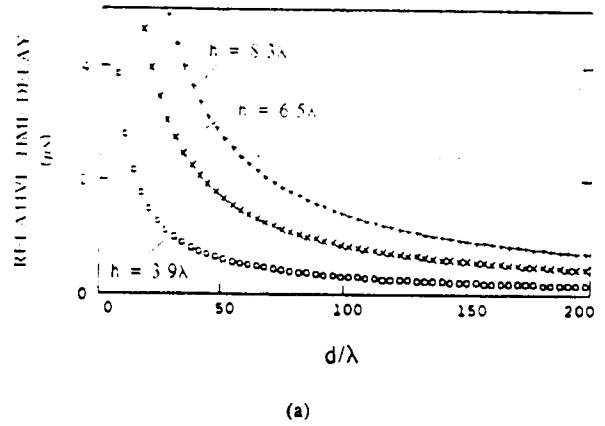


Fig. 4. Calculated time delay between pulses B and C plotted versus d/λ in (a) and plotted versus $d\lambda/h^2$ in (b). The $2.4 \mu s$ horizontal line corresponds to waveform duration.

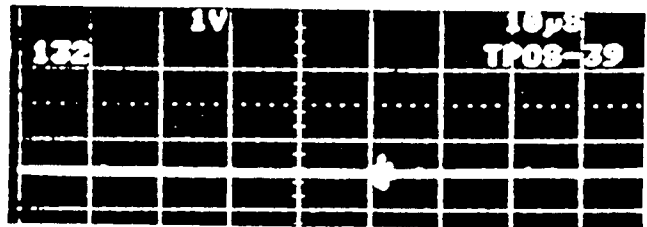


Fig. 5. Waveform of received backscattered waves with $d = 20\lambda$ and $h = 6.3\lambda$ obtained from contoured air/water/air pressure-release model.

acoustic interface wave conversion insonifying the shadow zone. Fig. 5 demonstrates the relatively small backscattered diffracted acoustic wave obtained when the solid glass is replaced with a contoured pressure-release boundary. A contoured pressure-release boundary was achieved by placing a $300 \mu m$ thick plastic membrane between the water and the glass to trap a thin air layer following the trench profile to decouple the acoustic waves in the water from the solid and create a contoured "free" pressure-release boundary. The time of arrival of the backscattered diffracted acoustic wave shown in Fig. 5 is approximately equal to the time of arrival of pulse B (Fig. 2).

III. CONCLUSION

Experimental results have been presented on backscattering of Scholte waves and near-grazing underwater acoustic waves from a trench at a liquid/solid interface. The backscattered

waves are characterized by interference of waves reflecting from the trench bottom and the distant steep side.

The results indicate that significant backscatter may be obtained from an object located in a shadow zone when penetrable boundaries are involved. The findings relate to interpretation of underwater acoustic wave data as applied to remote mapping of ocean bottom bathymetry, transmission loss prediction, acoustic imaging, and nondestructive testing.

ACKNOWLEDGMENT

The author would like to thank the anonymous reviewers for their suggestions.

REFERENCES

- [1] L. M. Brekhovskikh, *Waves in Layered Media*. New York: Academic, 1960.
- [2] S. A. Chin-Bing, D. B. King, J. A. Davis, and R. B. Evans, Eds., *PE Workshop II-Proceedings of the Second Parabolic Equation Workshop*. Mississippi: Naval Research Lab., Stennis Space Center, 1993.
- [3] R. A. Stephen, "Solutions to range-dependent benchmark problems by the finite-difference method," *J. Acoust. Soc. Amer.*, vol. 87, no. 4, 1527-1534, 1990.
- [4] T. W. Dawson and J. A. Fawcett, "A boundary integral equation method for acoustic scattering in a waveguide with nonplanar surfaces," *J. Acoust. Soc. Amer.*, vol. 87, no. 3, 1110-1125, 1990.
- [5] G. A. Kriegsmann and P. G. Petropoulos, "An approximate method for the study of transverse discontinuities in waveguides," *Wave Motion*, vol. 13, pp. 123-131, 1991.
- [6] A. D. Pierce, "Acoustics—An Introduction to its physical principles and applications," *Acoust. Soc. Amer.*, 1989.
- [7] J. R. Chamuel and G. H. Brooke, "Transient Scholte wave transmission along rough liquid-solid interface," *J. Acoust. Soc. Amer.*, vol. 83, no. 4, 1336-1344, 1988.
- [8] F. Luppé, "Interaction entre une onde de Scholte-Stoneley et un défaut du solide," *J. Acoustique* 3, 311-320, 1990.
- [9] J. R. Chamuel, "Ultrasonic studies of transient seismoacoustic waves in bounded solids and liquid/solid interfaces, Sonoquest Advanced Ultrasonics Research," Wellesley Hills, MA, *Rep. No. JRC-34-91*, 1991 (NTIS, U.S. Dept. of Commerce, Order No. AD-A24-3441).

SECTION 2

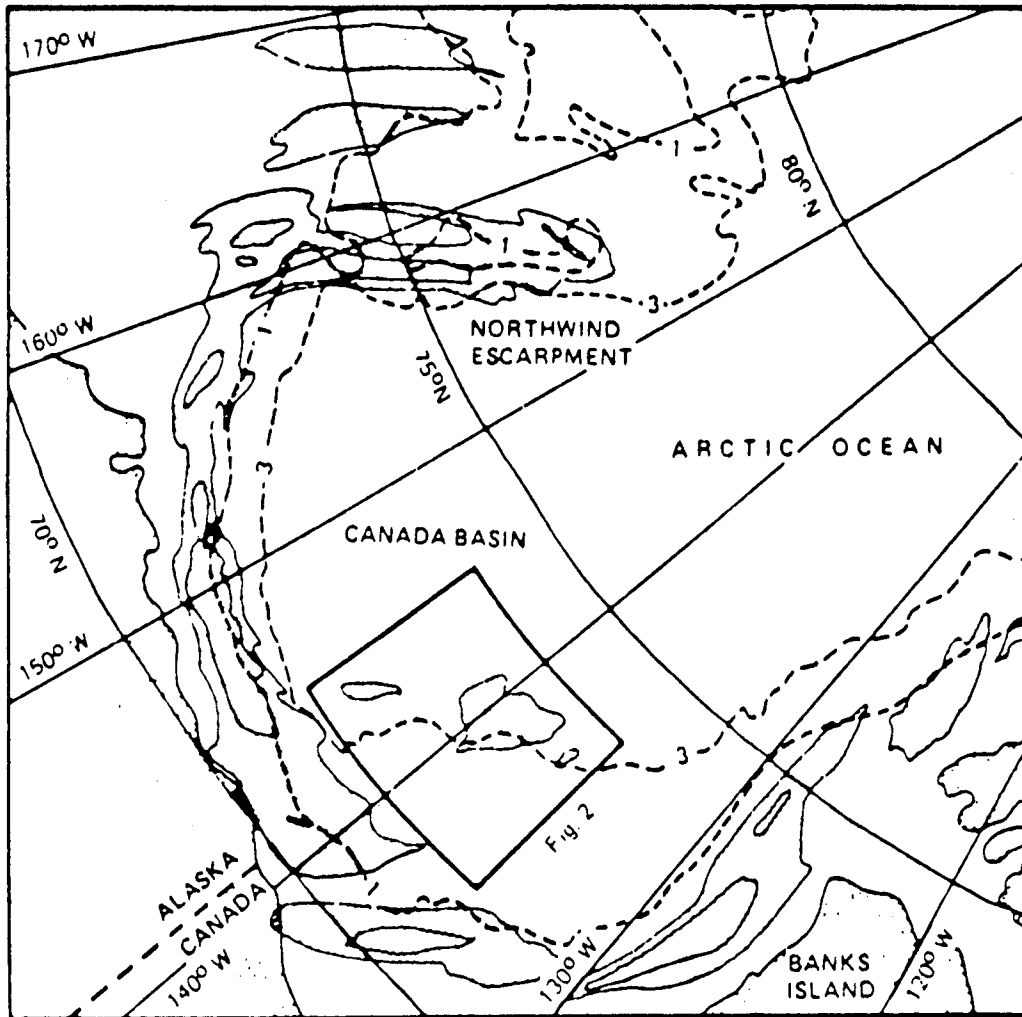
2 EXPLANATION FOR ACOUSTIC BACKSCATTERING FROM CANADA BASIN NEAR 73.2°N, 139°W WHERE NO KNOWN BATHYMETRIC HIGHS EXIST

Low-frequency acoustic backscattering from underwater topographic features has been used to characterize ocean boundaries over long ranges. A survey of low-frequency acoustic backscattering experiments was reported in 1986 by Baggeroer and Dyer [2.1]. Spindel and Heirtzler [2.2] used directional towed array receivers near the Bahamas and correlated the acoustic backscatter with topographic features. In the Arctic Ocean, Dyer, Baggeroer, Zittel, and Williams [2.3-2.5] used two-dimensional hydrophone arrays to identify individual bathymetric features in azimuth and range, and superbly correlated low-frequency acoustic backscattering data with known topographic highs such as mid-oceanic ridges, escarpments, and continental margins for ranges over 1000 km. Jiang [2.6] presented other low-frequency acoustic backscattering data obtained from the eastern Arctic Ocean.

The Canada Basin Acoustic Reverberation Experiment (CANBARX) results reported by Dyer et al. [2.3] also generated new localized acoustic backscatter which were interpreted as originating from a region near 73°N latitude, 139°W longitude in an area of the Canada Basin with no previously known bathymetric highs [2.3, 2.7, 2.8]. Grantz and Hart [2.7] charted the anomalous acoustic backscatter as a cluster of three isolated features (at about 73.2°N, 139°W, at 72.6°N, 145.5°W, and at 73.4°, 144°W) as shown in Fig. 2.1 and pointed out that the backscatter is not produced by bathymetric highs in the vicinity. In this report, the large central anomalous acoustic feature shown in Fig. 2.1 will be referred to as "F1", and the second largest feature as "F2". Grantz and Hart obtained new seismic reflection data in 1993 [2.9-2.10] indicating the absence of large bathymetric highs or geologic features in the vicinity of 73°N, 139°W (Fig. 2.2). Three segments of the seismic reflection data (Line 9318) are displayed in Fig. 2.2. The beginning and end of Line 9318 are marked on the bottom map.

An explanation is needed to comprehend the origin of the puzzling localized anomalous backscatter observed by Dyer et al. [2.3]. Chamuel [2.11] hypothesized that focused multiple scattering can explain the anomalous backscatter observed by Dyer et al. as explained below.

Two-dimensional hydrophone array data provide azimuth and range information. Range is calculated from the round trip propagation time along a straight line, and azimuth angle is determined from the observed angle θ_1 of the returning acoustic waves incident on the array. Range can be overestimated when acoustic waves propagate first in different directions towards a remote major topographic feature that focuses the reflected waves onto a much closer scatterer that in turn reflects the large amplitude focused waves back towards the source/receiver with the azimuth angle θ_1 . When focused multiple scattering are not taken into consideration, late-arriving backscattered waves approaching the receiver from the azimuth direction θ_1 can be misinterpreted as originating from a remote large scatterer at the same azimuth angle θ_1 .



Generalized bathymetric map of the western Arctic Ocean showing location of acoustic backscattering features [Dyer *et al.*, [1982] and their spatial relation to the continental margin. Shaded area shows iso-backscatter levels of -36 dB and higher. Contours show iso-backscatter levels of -36 dB and -30 dB. Isobaths, in kilometers, from Johnson *et al.* [1982].

Fig. 2.1 Diagram copied from A. Grantz and Hart [J. Geophys. Res. 89(C2), 2105(1984)] depicting cluster of three observed anomalous acoustic backscattering features near 73° N latitude, 139° W longitude where no known bathymetric highs exist.

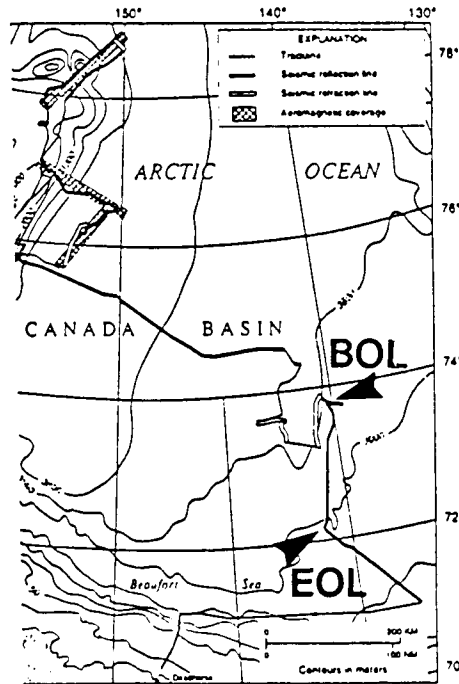
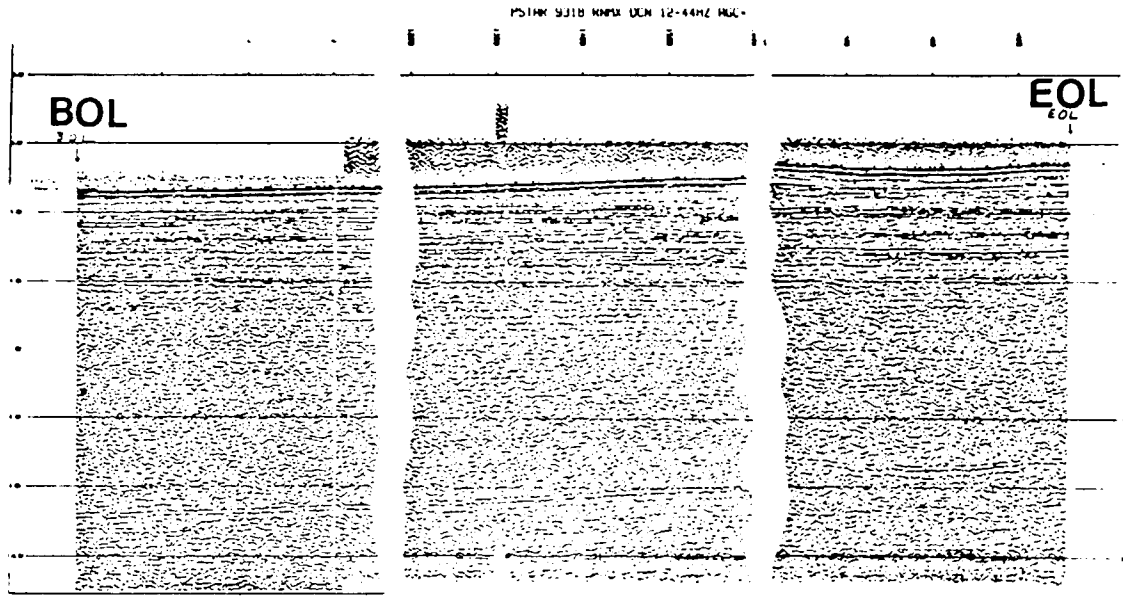


Fig. 2.2 Seismic reflection profile (line 9318) by Hart and Grantz (1994) demonstrating absence of bathymetric or geologic features in the vicinity that could explain the localized cluster of anomalous acoustic backscatter [Dyer et al. 1982]. The map shows the beginning and end of line 9318 [Grantz 1994].

Fig. 2.3 shows two general bathymetry maps of the Beaufort Sea. The anomalous acoustic backscattering feature F1 (range 353 km) is marked on the top map, and feature F2 (range 275 km) is marked on the bottom map. According to Chamuel's hypothesis [2.11], F1 is caused by scattering from the near-elliptical boundary B1 (stretching from 71.32°N, 148.5°W to 71.86°N, 152.63°W, Fig. 2.3(a) focused on a bathymetric feature A1 (73.5°N, 140.4°W) located at a much closer range (210 km) than F1 as shown. Similarly, F2 is caused by focused multiple scattering between another near-elliptical boundary B2 (Fig. 2.3(b)) and feature A2 located at a much closer distance (192 km) than F2. The range of these features can be overestimated by 43-68% when focused multiple scattering is ignored.

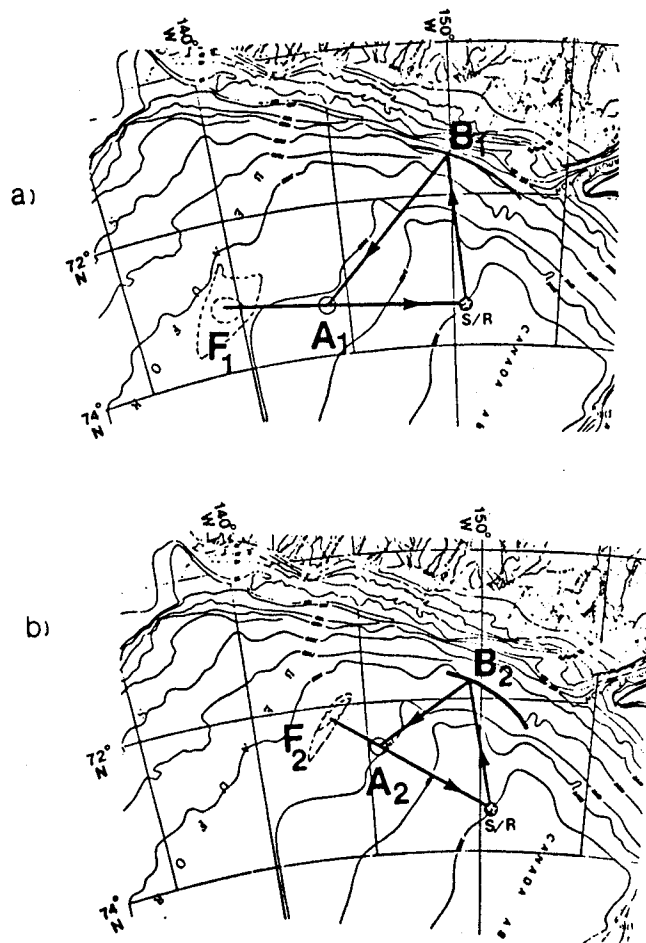


Fig. 2.3 Anomalous acoustic backscatter F1 (where no known bathymetric highs exist) may be the result of scattering by a major near-elliptical boundary B1 focused onto a much closer bottom feature A1. Both S/B1/A1/R and S/F1/R wave components have the same total round trip travel time and the same return azimuth angle. A similar hypothesis can be used to explain the second observed anomalous acoustic backscatter F2 shown in the bottom map, where the waves are focused by B2 onto a second closer bottom feature A2.

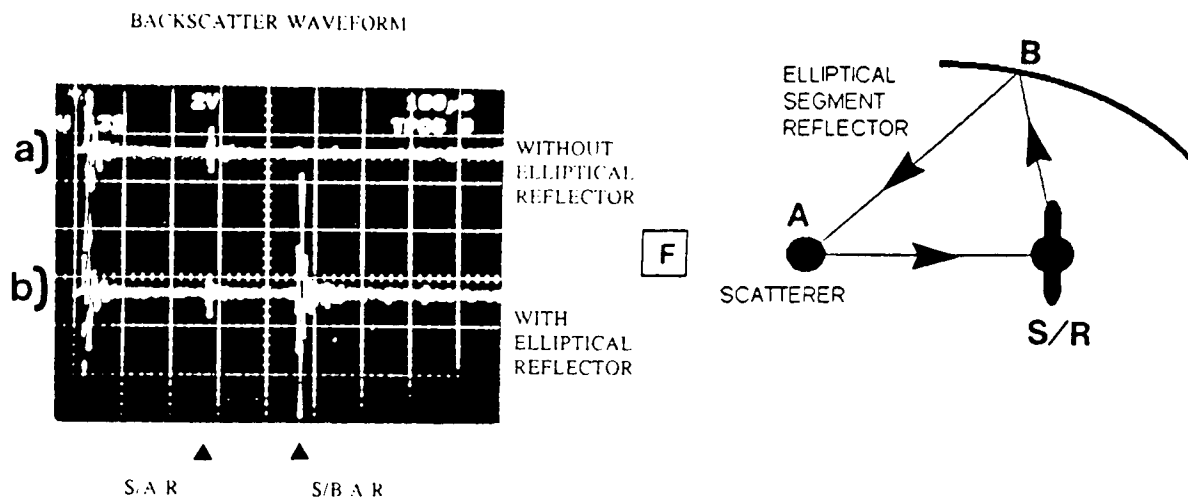


Fig. 2.4 Ultrasonic modeling results (Scale 1:1,200,000) comparing the relative amplitude and time of arrival of direct backscattered wave component S/A/R and late-arriving focused multiple scattering component S/B/A/R.

Scaled laboratory ultrasonic modeling experiments were conducted to verify Chamuel's hypothesis and provide an explanation for the anomalous acoustic backscatter observed by Dyer et al. . The author chose the simplest scaled ultrasonic model possible to clearly isolate the dominant phenomena involved and compare direct backscattered waves and multiple backscattered acoustic waves focused by a large elliptical reflector segment on the scatterer. Fig. 2.4 presents the experimental setup configuration and the results obtained from the scaled ultrasonic model (horizontal scale 1:1,200,000). The ultrasonic model consisted of a) a 2-D water waveguide , b) a small scatterer "A" positioned in the water at one focal point of an ellipse in the plane of the waveguide, c) a source and directional receiver "S/R" placed at the second focal point of the ellipse, and d) a segment of an elliptical reflector "B" approximately modeling the near-elliptical bathymetry profile between 71.32°N, 148.5°W to 71.86°N, 152.63°W positioned as shown in Fig. 2.4. The elliptical reflector was an air-backed vertical boundary intersecting the entire cross section of the water waveguide. The receiver was oriented towards the scatterer and the source (3 mm diameter) was excited with a single broadband pulse. The received signal was amplified, filtered, and displayed on a digital oscilloscope. Fig. 2.4.(a) displays the direct backscattered wave "S/A/R" obtained without the elliptical reflector. The horizontal time scale was 100 μ s/div. , and the water compressional wave velocity was 1480 m/s. The waveform shown in Fig. 2.4(b) was acquired with the elliptical reflector in place as shown. The amplitude of the direct reflection "S/A/R" was

small compared to the late-arriving focused backscattered component "S/B/A/R". The propagation time for S/A/R and S/B/A/R was 277 μ s and 457 μ s respectively. The position and orientation of the elliptical reflector followed the geometry of Fig. 2.3.(a) simulating the B1 boundary. If one attempts to interpret the waveform (Fig. 2.4(b)) without taking focused multiple scattering into consideration, the large backscattered wave S/B/A/R can be misinterpreted as originating from direct backscattering from a remote large scatterer "F" at the same azimuth angle as diagrammed in Fig. 2.4.

Another experiment was conducted using an irregular near-elliptical segment reflector following the 1500 m-depth contour derived from the Arctic Ocean Bathymetry map [2.12] (Fig. 2.5). The amplitude of the late-arriving backscattered wave focused by the irregular reflector was still substantially greater than the direct backscattered wave. The results of this experiment also suggest that in view of the averaging effect of the processor time window used by Dyer et al., variation in the position of source/receiver due to drift of the ice camp for example would have a moderate effect on the corresponding backscattered focused waves. A time window of 20s is equivalent to about 15 km variation in the reflecting boundary profile.

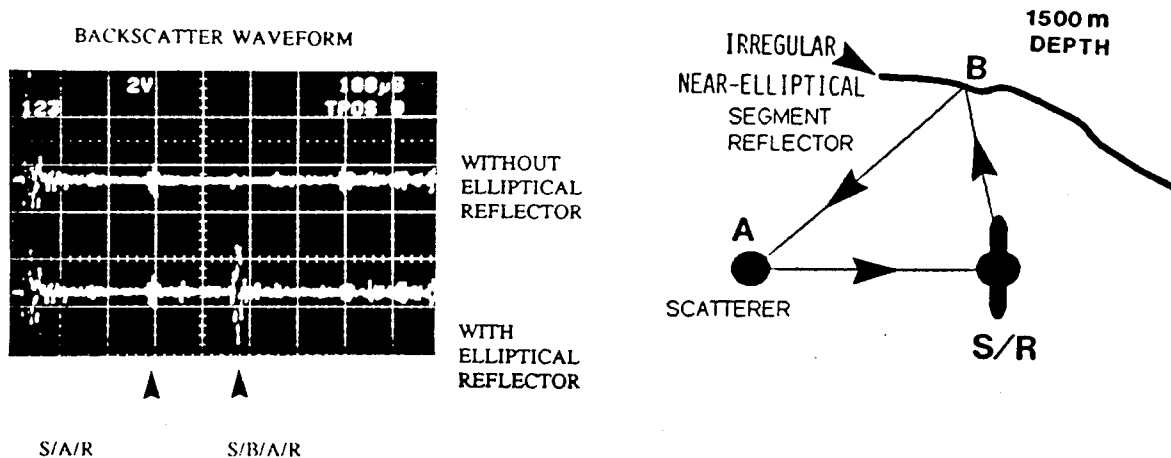


Fig. 2.5 Ultrasonic modeling results similar to previous figure obtained using an irregular near-elliptical reflector following the actual 1500 m depth map profile.

One important question to be answered is: If Chamuel's hypothesis is correct, then, scatterers A1 and A2 predicted by the hypothesis should have produced detectable direct backscattering signals in the original Arctic field data. The author examined the acoustic backscattering data in References [2.1, 2.3-2.5, 2.7, 2.8] searching for clues on the existence of the hypothesized ocean bottom features at A1 and A2. The author was gratified to find in one of the 9Hz figures in Williams' thesis [2.5] two backscattering signals originating from 73.3°N, 142.8°W and 72.6°N, 145.5°W corresponding precisely to locations A1 and A2 predicted by Chamuel's hypothesis as shown in Fig. 2.6.

Ultrasonic modeling results were presented indicating that focused multiple scattering should not be disregarded in interpreting two-dimensional hydrophone array underwater acoustic data. Future bathymetric measurements need to be conducted near 73.5°N, 140.4°W and 72.9°N, 147.4°W to verify the existence of the scattering features predicted by the proposed hypothesis.

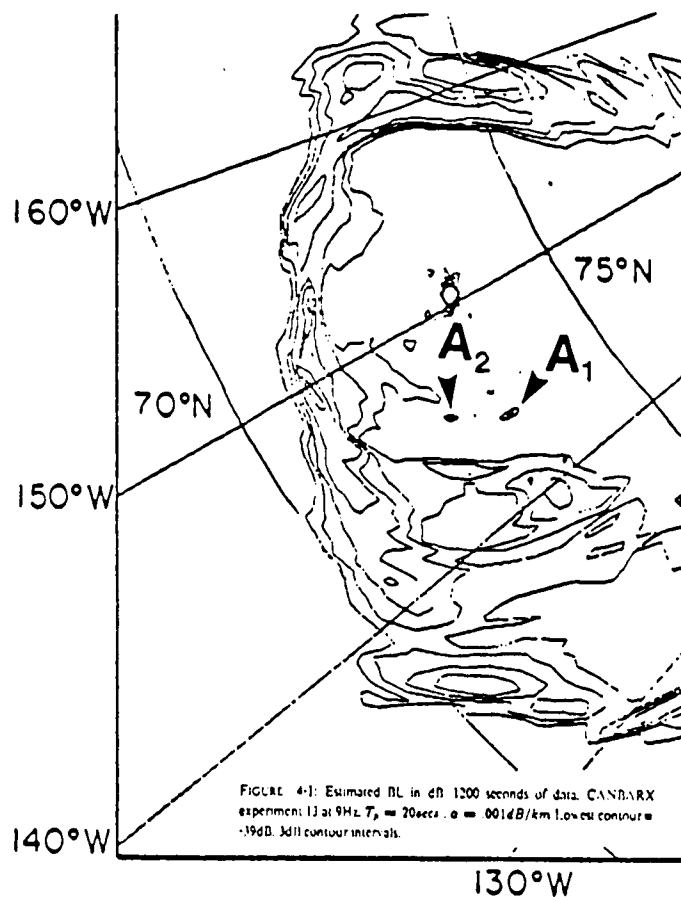


Fig. 2.6 Acoustic backscatter data with lowest contour = - 39 db [copied from fig. 4.1 by Williams 1981] revealing the existence of two backscattering features precisely at the locations A1 and A2 as predicted by Chamuel's focused multiple scattering hypothesis [1994].

2.1 References

- [2.1] A. B. Baggeroer and I. Dyer, "Long range, low frequency acoustic backscattering: a Survey," *Ocean Seismoacoustics*, Akal and Berkson, Plenum Press, NATO Conference Series IV:16, 313-326 (1986).
- [2.2] R. Spindel and J. H. Heirtzler, "Long range echo rangings," *J. Geophys. Res.* 77(35), 7073-7088 (1972).
- [2.3] I. Dyer, A. B. Baggeroer, J. D. Zittel, and R. J. Williams, "Acoustic backscattering from the basin and margins of the Arctic Ocean," *J. Geophys. Res.* 87, 9477-9488 (1982).
- [2.4] J. D. Zittel, "Ocean basin reverberation," Thesis, M.I.T., Cambridge, Mass. and Woods Hole Oceanographic Inst., Woodshole, Massachusetts (1979).
- [2.5] R. J. Williams, "Backscattering of low frequency sound from the topographic features of the Arctic Ocean Basin," M. S. Thesis, M. I. T., Cambridge, Massachusetts (1981).
- [2.6] Sheng-li Jiang, "Backscattering of sound in the eastern Arctic Ocean," Ph. D. Thesis, M. I. T., Cambridge, Massachusetts (1988).
- [2.7] A. Grantz and P. E. Hart, "Are there large bathymetric highs near 73°N, 139°W in the Arctic Basin? Comment on "Acoustic Backscattering from the Basin and Margins of the Arctic Ocean," by I. Dyer et al.," *J. Geophys. Res.* 89(C2), 2105-2108 (1984).
- [2.8] I. Dyer, "Reply," *J. Geophys. Res.* 89(C2), 2109 (1984).
- [2.9] A. Grantz, P. E. Hart, R. L. Phillips, M. McCormick, R. G. Perkin, R. Jackson, A. Gagnon, S. Li, C. Byers, and K. R. Schwartz, "Cruise report and preliminary results U.S. Geological Survey Cruise P1-93-AR Northwind Ridge and Canada Basin, Arctic Ocean aboard USCGC Polar Star August 16-September 15, 1993," U.S. Department of the Interior, U. S. Geological Survey, Open-File Report 93-389 (1994).
- [2.10] A. Grantz and P.E. Hart, "Seismic reflection profile line No. 9318 data," U.S. Geological Survey data 5 January 1994. Private Communication.
- [2.11] J. R. Chamuel, "On the interpretation of observed anomalous high acoustic backscatter from Arctic Basin using 2-D horizontal hydrophone array," *J. Acoust. Soc. Am.* 95(5), Pt.2, 3aAO4, 2883 (1994).
- [2.12] R. K. Perry, H. S. Fleming, J. R. Weber, Y. Kristoffersen, J. K. Hall, A. Grantz, G. L. Johnson, N. Z. Cherkis, and B. Larsen, Naval Research Lab. - Acoustics Division, Bathymetry of the Arctic Ocean, 1986.

SECTION 3

3 EFFECT OF A THIN LOW-VELOCITY LAYER UNDERNEATH A FLOATING PLATE ON FLEXURAL WAVE DISPERSION

3.1 Abstract

Theoretical and experimental results from a layered ultrasonic model are presented providing an explanation for previously reported 10-40% discrepancies between theoretical and measured Arctic field results by Hunkins [3.1] on the dispersion of flexural waves in sea ice between 50-500 Hz. The presence of a thin low-velocity fluid layer underneath a floating plate can substantially decrease the flexural wave group velocity maximum U_{max} of the Scholte wave branch and the velocity of higher frequency components [3.2]. Theoretical calculations indicate that, within a nominal range of sea ice parameters, the observed deviation of Arctic field data flexural wave dispersion is due to prevailing effects of the compressional velocity and thickness of this low velocity layer.

3.2 Introduction

Sea ice is a complex heterogeneous structure [3.3-3.4]. Hunkins' seismic studies on sea ice [3.1] revealed two discrepancies between measured and calculated flexural wave group velocity dispersion. The first discrepancy observed by Hunkins was that sea ice thickness determined from flexural wave dispersion is generally lower than the actual thickness. The second discrepancy in Hunkins field results is originating from flexural wave components to the right of U_{max} (meaning higher frequencies) having 10-40 % lower velocities than predicted (Fig. 3.1).

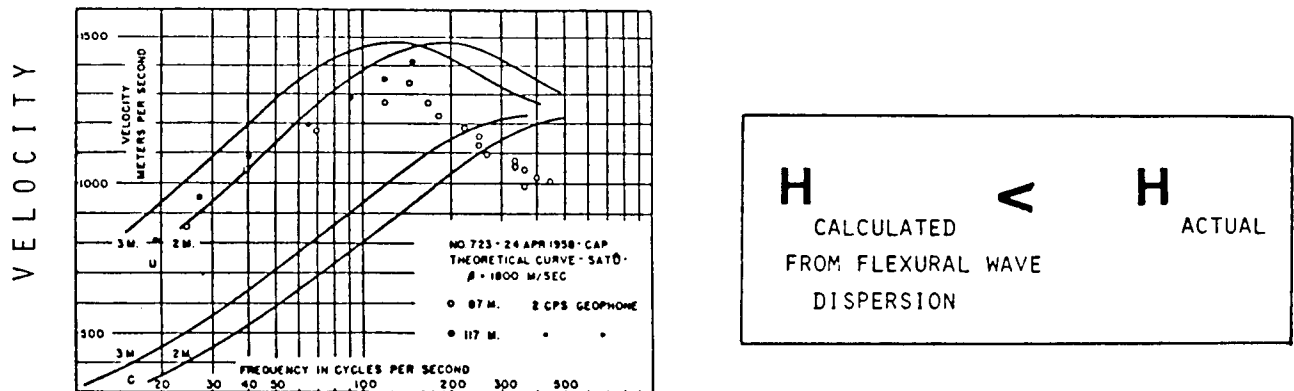


Fig. 12. Comparison of observed and theoretical dispersion for record 723, April 24, 1958.

FREQUENCY

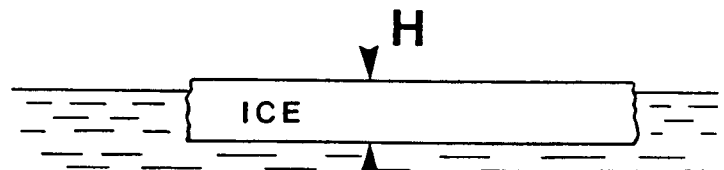


Fig. 3.1 Hunkins' results on flexural wave dispersion in floating sea ice [data copied from J. Geophys. Res. 65(10), 3469 (1960)].

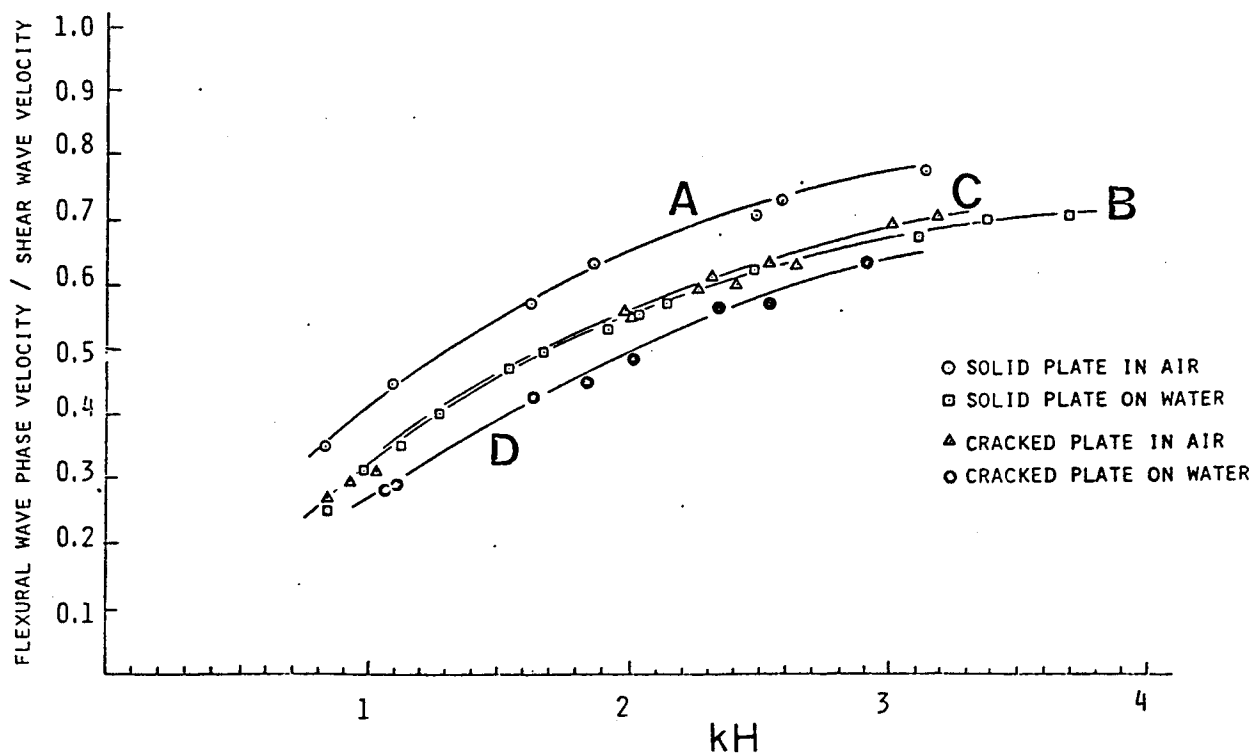


Fig. 3.2 Effect of water loading and shallow surface cracks on decreasing the flexural wave velocity. Model consisted of Plexiglas plate (thickness $H = 2.26$ mm) on water. Average crack spacing $s = 5$ mm, and crack depth $g = H/3$.

Previous ultrasonic modeling studies [3.5-3.6] provided an explanation for the first discrepancy by demonstrating that the presence of a large number of shallow cracks in a floating plate reduces the flexural wave group velocity and shifts the corresponding dispersion curves towards the behavior of an "effective" thinner plate. Fig. 3.2 illustrates the decrease in flexural wave phase velocity by multiple shallow surface cracks and water loading in a floating Plexiglas plate.

The second discrepancy on flexural waves in Hunkins' results cannot be resolved by simply changing the ice plate thickness to match the theoretical and field results. The author believes that by adding a thin low velocity layer underneath Hunkins' sea ice plate model a much closer agreement between the measured and predicted flexural wave results can be obtained. Bogorodskii et al. [3.7] reported that during the rapid growth of the ice cover, there are two longitudinal wave velocity minima across the thickness of a snow-covered ice pack. One minimum is at the snow cover with a velocity less than the velocity of sound in air, and the second minimum is at the "clear-ice" layer at the ice/water interface with a velocity of about 1050 m/s which is less than the sound velocity in water.

3.3 Theory

Kheisin [3.8] studied guided wave propagation due to a discontinuity in the ocean sound wave velocity underneath the ice cover, where a water layer about twice as thick as the

ice plate with a compressional wave velocity of 1450 m/s resting on a water half-space with a velocity of 1500 m/s. Kheisin's paper focused on determining the required minimum layer thickness at which unattenuated waveguide propagation is still possible for a given ice plate thickness. The current paper is concerned with the water/ice thin layer transition zone (about one tenth the ice plate thickness) where the longitudinal wave velocity may be lower than the water compressional wave velocity [3.7]. The shear wave speed is assumed to be zero in the low-velocity layer.

The theoretical results presented in this paper are based on expanding Kheisin's characteristic determinant D_2 from reference [3.8] for an isotropic solid plate floating on a layered fluid half-space with a low-velocity upper layer.

Upon expanding Kheisin's determinant D_2 , the following characteristic equation was obtained:

$$\frac{M^2 - NM [\tanh\phi \coth\theta + \tanh\theta \coth\phi] + N^2}{M [\coth\phi + \tanh\theta] - N [\coth\theta + \tanh\phi]} = \Gamma$$

where,

$$\Gamma = \frac{V^4 \rho_a \left[1 - \frac{V^2}{\alpha^2}\right]^{0.5} \left[\frac{\rho_w}{\rho_a} + \left[1 - \frac{V^2}{c^2}\right]^{0.5} \left[1 - \frac{V^2}{v^2}\right]^{-0.5} \tanh\psi \right]}{2\beta^4 \rho_s \left[1 - \frac{V^2}{v^2}\right]^{0.5} \left[\frac{\rho_w}{\rho_a} \tanh\psi + \left[1 - \frac{V^2}{c^2}\right]^{0.5} \left[1 - \frac{V^2}{v^2}\right]^{-0.5} \right]}$$

$$M = 4 \left[1 - \frac{V^2}{\alpha^2}\right]^{0.5} \left[1 - \frac{V^2}{\beta^2}\right]^{0.5}$$

$$N = \left[2 - \frac{V^2}{\beta^2}\right]^2$$

$$\phi = (\pi fH/V) \left[1 - \frac{V^2}{\beta^2}\right]^{0.5}$$

$$\theta = (\pi fH/V) [1 - V^2/\alpha^2]^{0.5}$$

$$\psi = (2\pi fd/V) [1 - V^2/v^2]^{0.5}$$

f = frequency, H = plate thickness, V = phase velocity, α = plate compressional wave velocity, β = plate shear wave velocity, ρ_p = plate density, d = layer thickness, v = layer sound wave velocity, ρ_w = layer density, c = compressional wave velocity of liquid half-space, and ρ_w = density of liquid half-space.

The group velocity U was calculated from the fundamental relation

$$U = V + k \, dV/dk \quad ,$$

where k is the wavenumber.

3.4 Results

In order to investigate the effect of a low velocity layer underneath a floating plate on flexural waves, laboratory experiments were conducted on a layered ultrasonic model as described below.

Fig. 3.3(a) shows a diagram of the ultrasonic model. A 2.3 mm thick glass plate was placed on top of a water "half-space". Source and receiver transducers were placed on the free surface of the glass plate to generate and detect flexural waves. The source and receiver transducers were piezoelectric broadband compressional transducers (Sonoquest 3 mm diameter) placed on the top surface of the glass plate separated by the distance $x = 15$ cm. The source was excited with a single broadband pulse (30 KHz-1 MHz) and the received waveform was recorded on a digital oscilloscope (Tektronix 7D20). The plate dimensions and water depth were selected large enough to avoid interference from edge reflections. The general experimental setup was previously described elsewhere [3.5,3.8]. The waveform of the received dispersive flexural wave is presented in Fig. 3.3(b).

The experiment was repeated with an alcohol layer between the glass plate and water (Fig. 3.3 (c)). A 0.1 mm thick acetate membrane was used to separate the alcohol from the water. The edges of the membrane were bonded to the bottom surface of the glass plate forming a sealed chamber filled with alcohol. The alcohol was introduced through a 1 mm diameter hole predrilled in the glass. The hole was located away from the direct wave path. The alcohol volume was controlled to produce the desired layer thickness. The alcohol layer thickness "d" was 0.7 mm. The waveform of the received flexural wave with the alcohol layer is shown in Fig. 3.3(d). The alcohol layer slowed down the flexural wave. The effect of the membrane on the flexural wave dispersion was negligible. The measured

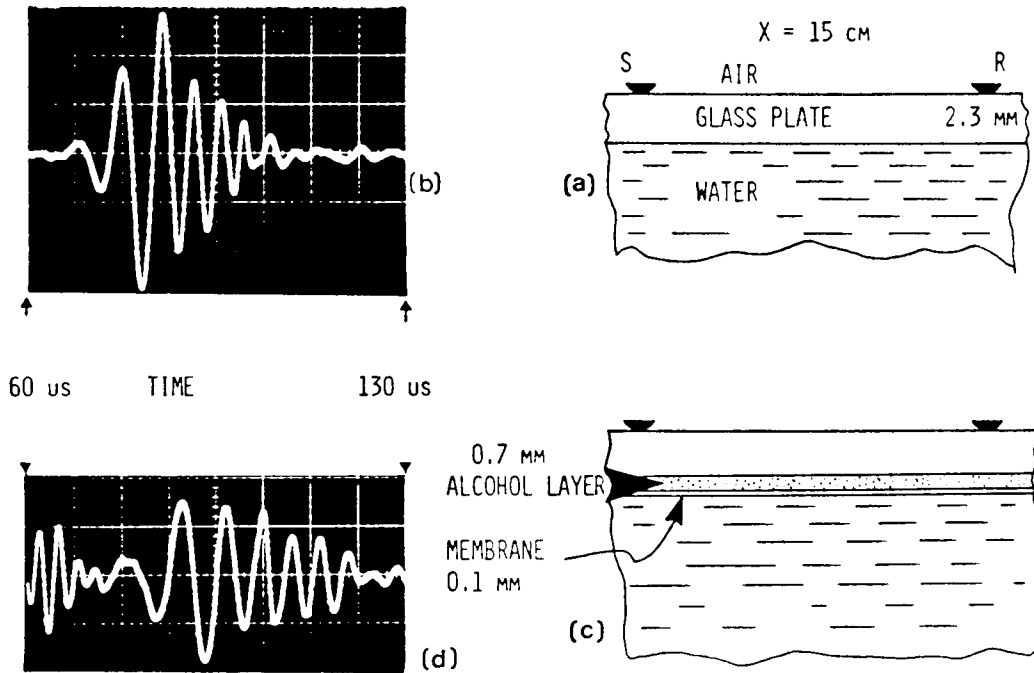


Fig. 3.3 Ultrasonic modeling results. **Top:** waveform of flexural wave from glass/water model. **Bottom:** waveform from glass/alcohol/water model. The effect of the 0.1 mm thick acetate membrane used to separate the alcohol from the water is negligible.

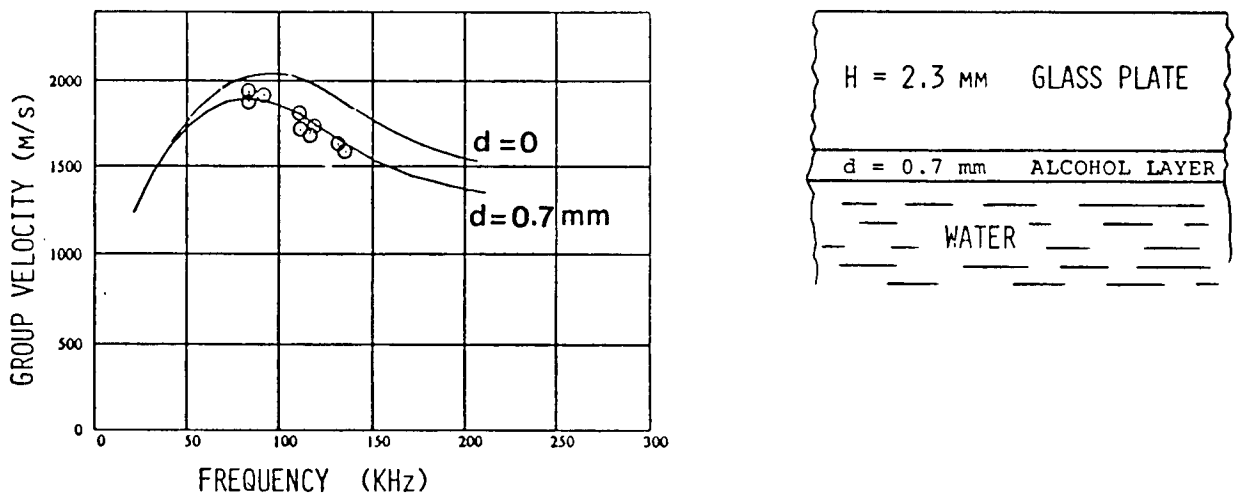


Fig. 3.4 Effect of a thin low-velocity layer underneath a floating plate on flexural wave group velocity dispersion. Theoretical results (solid lines). Experimental results from layered model with $d = 0.7 \text{ mm}$ (open circles).

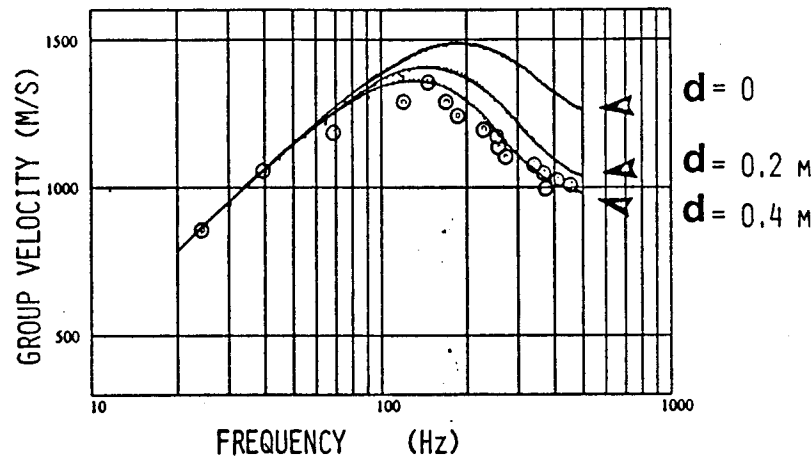


Fig. 3.5 Effect of varying the thickness d of the low-velocity layer on the flexural wave group velocity. The model parameters are: $\alpha = 3500$ m/s, $\beta = 1856$ m/s, $H = 2$ m, $\rho_a = 0.89 \times 10^3$ kg/m³, $v = 1005$ m/s, $\rho_u = 0.8 \times 10^3$ kg/m³, $c = 1440$ m/s, and $\rho_w = 1 \times 10^3$ kg/m³. The open circles are from Hunkins' sea ice flexural wave data.

compressional wave speeds of the glass plate, alcohol, and water were 5830, 1207, and 1480 m/s, respectively. The shear wave speed of the plate was 3413 m/s. The densities in the same order were 2.25 , 0.8 , and 1.0×10^3 Kg/m³.

The flexural wave group velocity experimental results are compared with theoretical dispersion curves in Fig. 3.4. The experimental and theoretical results agree reasonably well. The low-frequency components are practically unaffected by the presence of the thin alcohol layer. The group velocity of the higher frequency components decreased similar to Hunkins' sea ice flexural wave field data.

Fig. 3.5 displays three theoretical sea ice flexural wave group velocity curves plotted as function of frequency for three low-velocity layer thicknesses $d = 0$, 0.2 , and 0.4 m. The open circles results in FIG. 3 were obtained from Hunkins' Arctic field data [3.1]. The top curve is similar to the theoretical curve provided by Hunkins. One notes that the theoretical curve ($d=0$) deviates by almost 40 % from the field results to the right of the group velocity maximum. The plot dimensions and scales were selected to match Hunkins' plots. The theoretical curves were based on the following parameters: $\alpha = 3500$ m/s, $\beta = 1856$ m/s, $\rho_a = 0.89 \times 10^3$, $H = 2$ m, $v = 1005$ m/s, $\rho_u = 0.8 \times 10^3$, $d = 0.2$ m, $c = 1440$ m/s, and $\rho_w = 1 \times 10^3$.

Other theoretical results were calculated to demonstrate the effect of varying the compressional wave speed V and density ρ_a of the low-velocity layer (Fig. 3.6 - Fig. 3.7). Variations in V or d produced similar effects on the flexural wave. Nominal changes in ρ_a had little effect on the flexural wave dispersion (Fig. 3.7). For comparison, Fig. 3.8 displays the effect of the ice shear wave speed on the flexural wave group velocity of the floating plate.

3.5 Conclusions

Theoretical and laboratory experimental results presented in this paper demonstrated the effect of a thin low-velocity layer underneath a floating plate on reducing the group velocity of low-frequency flexural waves and provided an explanation for previously reported discrepancies on flexural wave dispersion in sea ice [3.1] between 50-500 Hz. The results demonstrated that a 15 cm layer under a 2 m thick ice plate can reduce the group velocity of flexural wave components by as much as 40% although the flexural wavelength is greater than the ice plate thickness. Parametric studies revealed that the trend observed in Hunkins flexural wave field data was matched by varying the thickness of the low-velocity layer and its compressional wave velocity. The findings contribute to fundamental understanding of high latitude underwater acoustic wave phenomena.

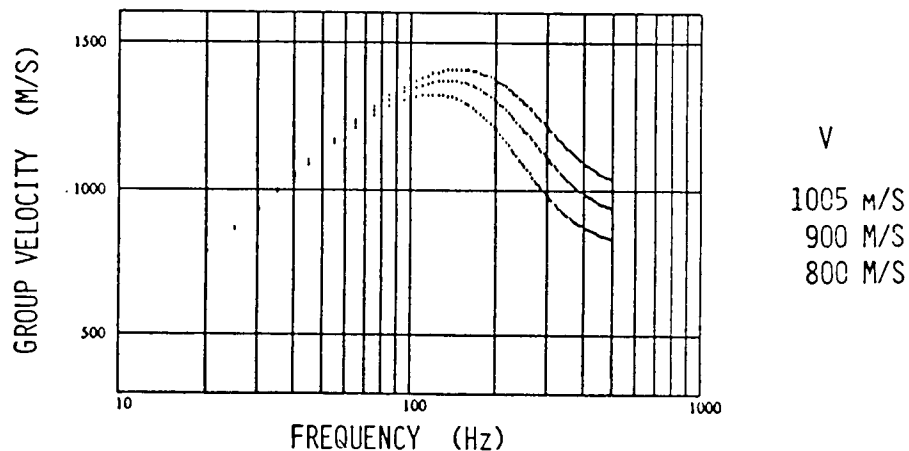


Fig. 3.6 Effect of varying the compressional wave velocity of the low-velocity layer on the flexural wave group velocity. The model parameters are: $\alpha = 3500$ m/s, $\beta = 1856$ m/s, $H = 2$ m, $\rho_s = 0.89 \times 10^3$ kg/m³, $d = 0.2$ m, $\rho_a = 0.8 \times 10^3$ kg/m³, $c = 1440$ m/s, and $\rho_w = 1 \times 10^3$ kg/m³.

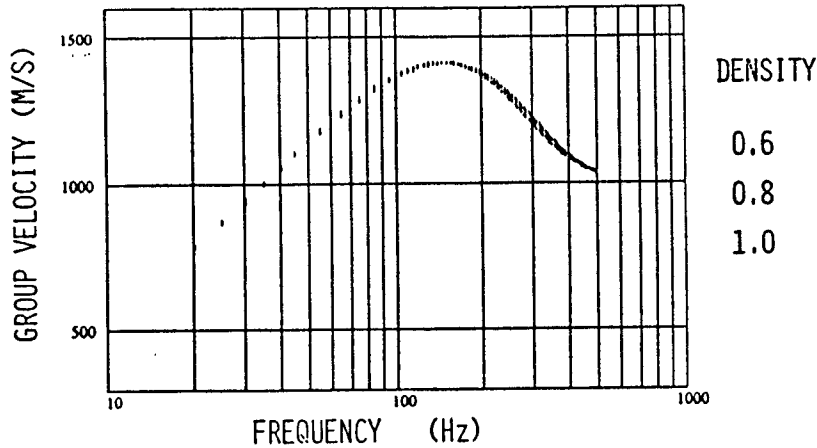


Fig. 3.7 Effect of varying the density of the low-velocity layer on the flexural wave group velocity. **Top:** $\rho_u = 0.6 \times 10^3 \text{ kg/m}^3$, **middle:** $\rho_u = 0.8 \times 10^3 \text{ kg/m}^3$, and **bottom:** $1.0 \times 10^3 \text{ kg/m}^3$. The model parameters are: $\alpha = 3500 \text{ m/s}$, $\beta = 1856 \text{ m/s}$, $H = 2 \text{ m}$, $\rho_s = 0.89 \times 10^3 \text{ kg/m}^3$, $v = 1005 \text{ m/s}$, $d = 0.2 \text{ m}$, $c = 1440 \text{ m/s}$, $\rho_w = 1 \times 10^3 \text{ kg/m}^3$.

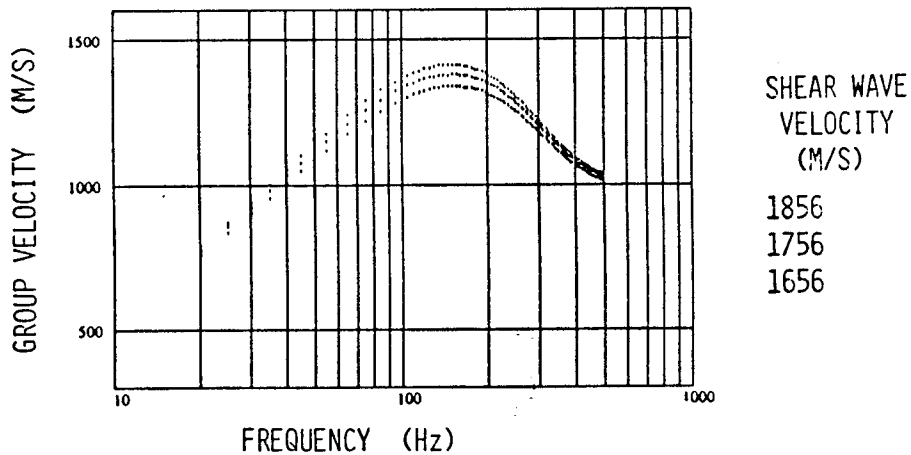


Fig. 3.8 Effect of ice shear wave speed on flexural wave group velocity. **Top:** $\beta = 1856 \text{ m/s}$, **middle:** $\beta = 1756 \text{ m/s}$, and **bottom:** $\beta = 1656 \text{ m/s}$. The model parameters are: $\alpha = 3500 \text{ m/s}$, $H = 2 \text{ m}$, $\rho_s = 0.89 \times 10^3 \text{ kg/m}^3$, $v = 1005 \text{ m/s}$, $d = 0.2 \text{ m}$, $\rho_u = 0.8 \times 10^3 \text{ kg/m}^3$, $c = 1440 \text{ m/s}$, $\rho_w = 1 \times 10^3 \text{ kg/m}^3$.

3.6 References

- [3.1] K. Hunkins, "Seismic studies of sea ice," J. Geophys. Res. vol. 65, 3459-3472, Fig.12, (1960).
- [3.2] J. R. Chamuel, "Effect of a thin low-velocity layer underneath a floating plate on flexural waves," J. Acoust. Soc. Am. 92(4), Pt.2, 2342 (1992).
- [3.3] J. Schwarz and W. F. Weeks, "Engineering properties of sea ice," J. Glaciology 19, 499-531 (1977).
- [3.4] A. J. Gow and W. B. Tucker III, Physical and Dynamic Properties of Sea Ice in the Polar Oceans, U.S. Army Corps of Engineers, Cold Regions Research & Engineering Lab., Monograph 91-1 (September 1991). Available from NTIS U.S. Department of Commerce, Springfield, Virginia.
- [3.5] J. R. Chamuel and G. H. Brooke, "Low-frequency transmission losses and effective flexural rigidity of cracked ice cover," J. Acoust. Soc. Am. S1 79, S57 (1986).
- [3.6] J. R. Chamuel, "Arctic acoustics Ultrasonic Modeling Studies," Sonoquest Advanced Ultrasonics Research, Report No. JRC-10-90, (March 1990). Available from National Technical Information Service U.S. Dept. of Commerce, Springfield, Virginia, Accession Report No. AD-A224165.
- [3.7] V. V. Bogorodskii, V. P. Gavriilo, and V.A. Nikitin, "Sound propagation in ice crystallized from salt water," Soviet Physics - Acoustics vol. 22, 158-159 (1976).
- [3.8] D.E. Kheisin, "Waveguide propagation of oscillations in a floating solid plate and a contiguous compressible fluid layer," Soviet Physics 16, 495-499 (1971).
- [3.9] J. R. Chamuel and G. H. Brooke, "Transient Scholte wave transmission along rough liquid-solid interfaces," J. Acoust. Soc. Am. 83, 1326-1344 (1988).
- [3.10] J. R. Chamuel, "Ultrasonic studies of transient seismo-acoustic waves in bounded solids and liquid/solid interfaces," Sonoquest Report No. JRC-34-91, (Nov. 1991). Available from National Technical Information Service U.S. Dept. of Commerce, Springfield, Virginia, Accession Report No. AD-A243441.

SECTION 4

4 EFFECT OF VISCOUS WAVES FROM SUSPENDED PARTICLES UNDER SEA ICE ON LOW-FREQUENCY ACOUSTIC WAVE REFLECTIVITY

The Arctic ice cover affects the propagation of underwater acoustic waves, and contributes to the characteristics of underwater ambient noise. It is essential to accurately model sea ice to be able to predict long range underwater acoustic wave propagation.

Hunkins [4.1] revealed discrepancies between Arctic field data and theoretical flexural wave velocity dispersion curves from sea ice. The calculated ice thickness from flexural wave dispersion was about 20 % smaller than the actual thickness. Also, the measured sea ice flexural wave group velocity for frequencies above about 100 Hz was about up to 40 % smaller than theoretically predicted. In the previous section of this report (Section 3), the effect of a low-velocity layer underneath floating sea ice on flexural wave dispersion was discussed. Theoretical and experimental results were presented giving an explanation for observed discrepancies between Hunkins' flexural wave field data [4.1] and theoretical predictions. By introducing a low-velocity fluid layer underneath floating sea ice, theoretical results were obtained matching the flexural wave dispersion field results [4.2]. Regarding under ice acoustic wave reflectivity, Yang and Votaw [4.3] obtained Arctic field results revealing frequency dependent under ice reflectivity data that could not be matched with any known theoretical modeling results.

Fig. 4.1 compares Yang and Votaw's field measurements with theoretical reflectivity calculations obtained by the author using a thin low-velocity fluid layer between the ice and the water half-space as shown. The theoretical results were obtained using the model parameters given in Fig. 4.1. One notices that the theoretical and field reflectivity results do not coincide. The introduction of a low-velocity fluid layer under the ice does not fully satisfy

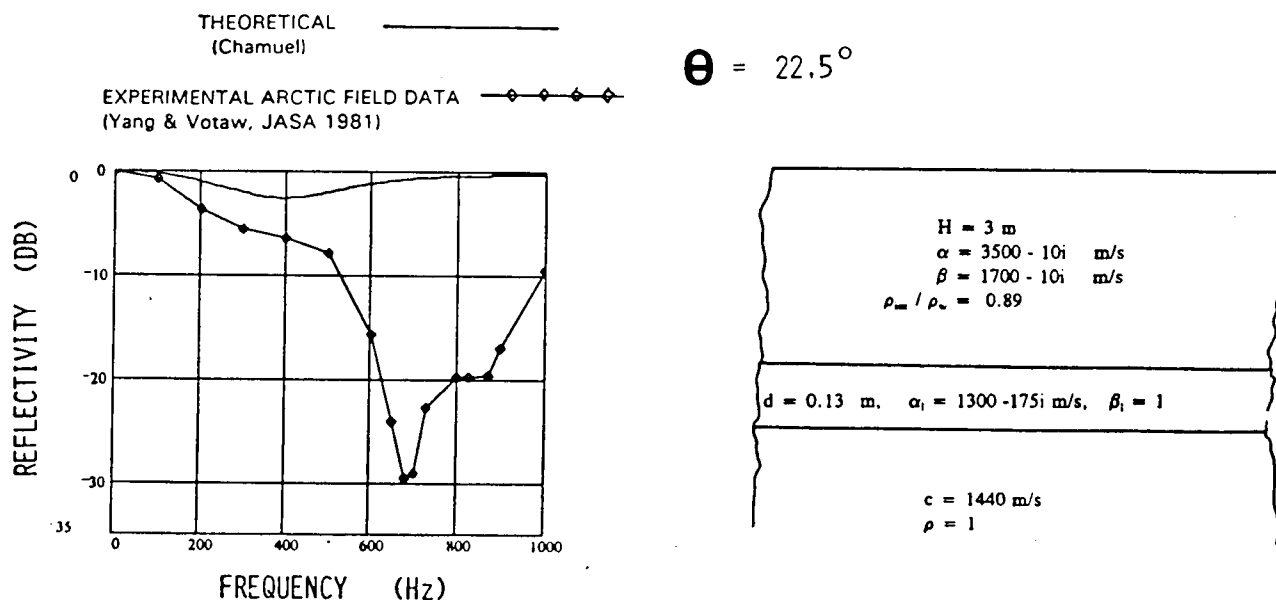


Fig. 4.1 Under ice reflectivity field data compared with theoretical calculations from ice model with low velocity fluid layer under floating plate. $\Theta = 22.5^\circ$.

the reflectivity data. The equations used in this section to calculate the reflection coefficient were derived by Folds and Loggins [4.4]. The reflectivity results presented in Fig. 4.1 were determined using a shear wave speed $\beta_1 = 1$ m/s instead of zero in the low-velocity layer to be able to compare these results with the ones described below (identical reflectivity plots were obtained with $\beta_1 = 0$ or 1 m/s).

McCammon and McDaniel [4.5] computed frequency dependent under ice theoretical reflectivity results from a layered ice model. Yew and Weng [4.6] modeled sea ice as a transversely isotropic porous medium and included a thin porous skeletal layer with large pore size and higher porosity. Their theoretical results are compared with Yang and Votaw's field data [Fig. 4.2]. Qualitative agreement is observed between the field and calculated results. Stanton et al. [4.7] used reflections of 100-800 kHz normally incident underwater acoustic waves to characterize the permeable dendritic structure near the ice/water interface. Williams et al. [4.8] conducted in-situ experiments to determine the acoustic properties of the skeletal layer at the water/ice interface.

Chin-Bing [4.9], Posey et al. [4.10], and Lawrence et al. [4.11] calculated high frequency under ice reflectivity from a layered ice model with a water-to-ice transition layer. The ice model parameters used by Chin-Bing are given in Table 4.1. Notice the low shear wave velocity in this transition layer model has a corresponding negligible shear wave attenuation coefficient (Table 4.1).

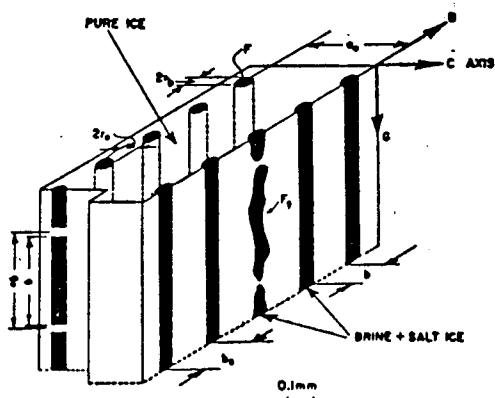


FIG. 3. Idealized sea-ice structure (Schwarz and Weeks, 1977).

C. H. Yew and X. Weng: Reflection and refraction from sea ice 343

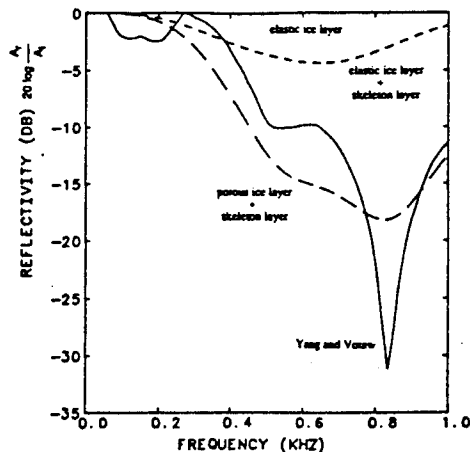


FIG. 17. Comparison with experimental results. $\alpha = 66.6$ deg (grazing angle = 23.4 deg), elastic ice layer ($H = 1$ m, $\beta_1 = 0$), porous ice layer ($H = 1$ m, $\beta_2 = 0.1$), skeleton layer ($h = 0.2$ m, $\beta_3 = 0.5$).

Fig. 4.2 Underice reflectivity field data compared with theoretical calculations by Yew and Weng's [4.6] based on sea ice modeled as a transversely isotropic porous medium. $\Theta = 23.4^\circ$.

Table 4.1 Layered ice and transition layer parameters used by Chin-Bing [4.9]. Notice negligible shear wave attenuation in transition layer. (Table copied from Reference 4.9)

TABLE I

LAYER TYPE	LAYER THICKNESS (M)	DENSITY (GM/CC)	COMPRES. SPEED (M/SEC)	SHEAR SPEED (M/SEC)	COMPRES. ATTENUATION (DB/M-KHZ)	SHEAR ATTENUATION (DB/M-KHZ)
WATER	INFINITE	1.02	1500.0	0.0	0.00	0.00
ICE	0.015	0.75	1300.0	650.0	0.06	0.22
ICE	0.015	0.88	1500.0	750.0	0.06	0.28
ICE	0.020	0.90	1700.0	850.0	0.06	0.29
ICE	0.020	0.90	1900.0	950.0	0.06	0.30
ICE	0.025	0.90	2100.0	1050.0	0.06	0.31
ICE	0.030	0.90	2300.0	1150.0	0.06	0.32
ICE	0.040	0.90	2600.0	1300.0	0.06	0.33
ICE	0.065	0.90	2900.0	1450.0	0.06	0.34
ICE	0.080	0.90	3200.0	1600.0	0.06	0.35
ICE	0.050	0.90	3400.0	1750.0	0.06	0.36
ICE	0.050	0.90	3600.0	1800.0	0.06	0.36
ICE	0.070	0.90	3700.0	1850.0	0.06	0.36
ICE	1.070	0.90	3500.0	1900.0	0.06	0.36
ICE	0.070	0.90	3700.0	1850.0	0.06	0.36
ICE	0.060	0.90	3600.0	1800.0	0.06	0.36
ICE	0.050	0.90	3400.0	1700.0	0.06	0.36
ICE	0.085	0.90	3200.0	1600.0	0.06	0.36
ICE	0.070	0.90	3000.0	1500.0	0.06	0.36
ICE	0.055	0.90	2800.0	1400.0	0.06	0.36
ICE	0.040	0.90	2700.0	1350.0	0.06	0.36
ICE	0.020	0.90	2600.0	1300.0	0.06	0.36
SLUSH	0.015	0.91	2500.0	1250.0	0.06	0.10
SLUSH	0.010	0.92	2400.0	700.0	0.06	0.04
SLUSH	0.010	0.93	2300.0	150.0	0.06	0.01
SLUSH	0.005	0.93	2200.0	20.0	0.06	0.00
SLUSH	0.005	0.94	2000.0	0.0	0.06	0.00
SLUSH	0.002	0.94	1700.0	0.0	0.06	0.00
SLUSH	0.002	0.95	1400.0	0.0	0.06	0.00
SLUSH	0.001	0.96	1150.0	0.0	0.06	0.00
SLUSH	0.003	0.98	1060.0	0.0	0.06	0.00
SLUSH	0.004	0.99	1030.0	0.0	0.06	0.00
SLUSH	0.005	1.00	1020.0	0.0	0.06	0.00
SLUSH	0.008	1.00	1015.0	0.0	0.06	0.00
SLUSH	0.006	1.01	1030.0	0.0	0.06	0.00
SLUSH	0.005	1.01	1040.0	0.0	0.06	0.00
SLUSH	0.005	1.01	1060.0	0.0	0.06	0.00
SLUSH	0.005	1.01	1100.0	0.0	0.06	0.00
SLUSH	0.005	1.01	1160.0	0.0	0.06	0.00
SLUSH	0.005	1.01	1200.0	0.0	0.06	0.00
WATER	INFINITE	1.02	1500.0	0.0	0.00	0.00

Lindrose [4.12] used shear ultrasonic waves to monitor the curing process of epoxy resin. His results showed that before curing, the epoxy shear wave speed was very low, however, the corresponding shear wave attenuation was very high (Fig. 4.3). As the epoxy cured, the shear wave speed increased and the shear wave attenuation decreased rapidly. The author believes that there is a similarity between curing epoxy and solidifying ice. The author was able to match Yang and Votaw's reflectivity results [4.3] by incorporating the effect of shear viscous waves in the low-velocity layer under the ice with an **extremely high** shear wave attenuation coefficient. Figure 4.4 compares Yang and Votaw's results with Chamuel's numerical results [4.2] calculated with grazing angle $\Theta = 22.5^\circ$. Very good agreement between the predicted and measured results was obtained when the shear wave speed of 1 m/s in the low-velocity layer was replaced with an assumed complex shear wave velocity equal to $1 - 650i$ m/s. No attempt was made here to model the viscoelastic properties of ice particles suspensions. The rheology of suspensions is beyond the scope of the present effort.

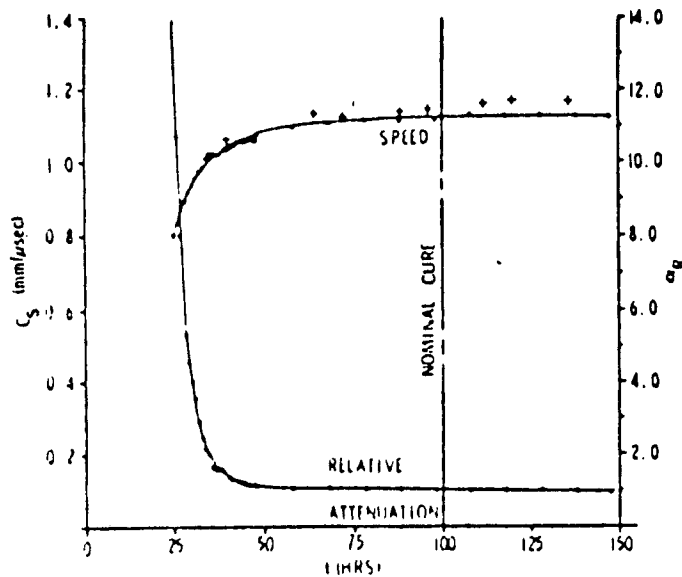


Fig. 5—Shear-wave speed and relative attenuation vs. epoxy cure time : • present data; + preliminary data

Fig. 4.3 Shear wave speed and relative attenuation plotted vs cure time [copied from Lindrose, Experimental Mechanics, 1978].

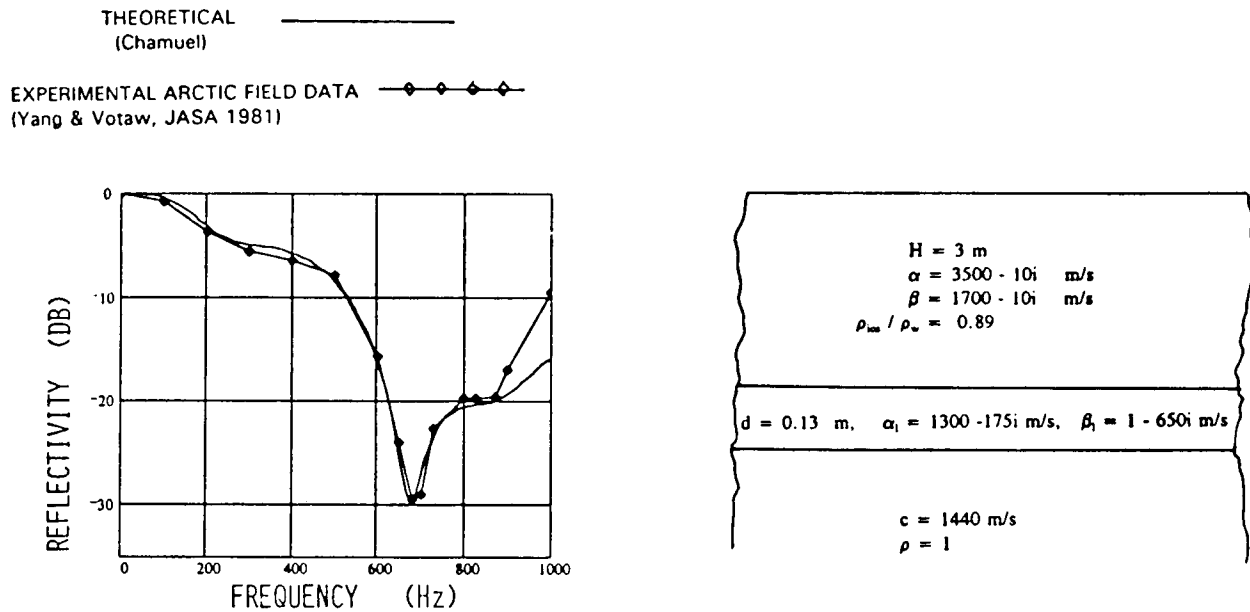


Fig. 4.4 Under ice reflectivity field data compared with theoretical calculations based on ice model with viscous waves in layer under floating ice. $\Theta = 22.5^\circ$.

Yang and Votaw's reflectivity plots depend on frequency and angle of incidence of the acoustic waves. If the model proposed by Chamuel is correct, it should satisfy the reflectivity dependency on both frequency and grazing angle. Three reflectivity curves plotted as function of frequency with three grazing angles $\Theta = 18.3^\circ$, 22.5° , and 23.4° from Yang and Votaw's results are compared in Fig. 4.5 with theoretical curves obtained with the assumed parameters shown in Fig. 4.6. The thickness of the low-velocity layer d was 9.61 cm for both the 23.4° and 22.5° grazing angle cases. d was increased to 16.2 cm to generate the reflectivity curve at $\Theta = 18.3^\circ$. The geometrical configuration of the field experiment conducted by Yang and Votaw caused the acoustic waves to reflect from different horizontal locations along the ice/water interface as the grazing angle was changed. For example, as Θ was changed from 18.6° to 23.4° , the reflection point shifted by 52 m horizontally along the water/ice interface. In the Arctic, the thickness of the low-velocity layer is range dependent. It is reasonable to assume that the thickness of the low-velocity layer with viscous waves changed in thickness from 9.6 cm to 16.2 cm between the two locations. Considering that there are several variables and unknowns in this problem, it is remarkable to have been able to match the calculated results to Yang and Votaw's field results for the first time both in frequency and grazing angle (Fig. 4.5).

The presence of a low-velocity layer supporting shear viscous waves under sea-ice may explain the observed excessive low-frequency long-range transmission loss. Future Arctic field experiments need to include in-situ measurements of viscous waves in a thin layer near the water/ice interface.

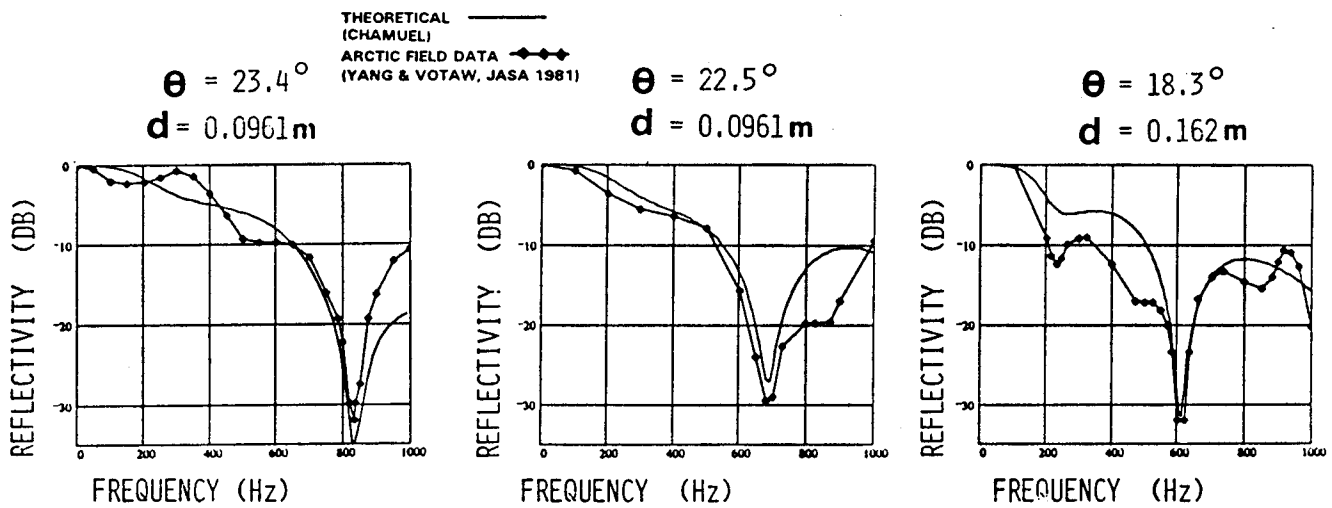


Fig. 4.5 Underice reflectivity field data [4.3] compared with theoretical results based on ice model with assumed viscous layer under floating ice.

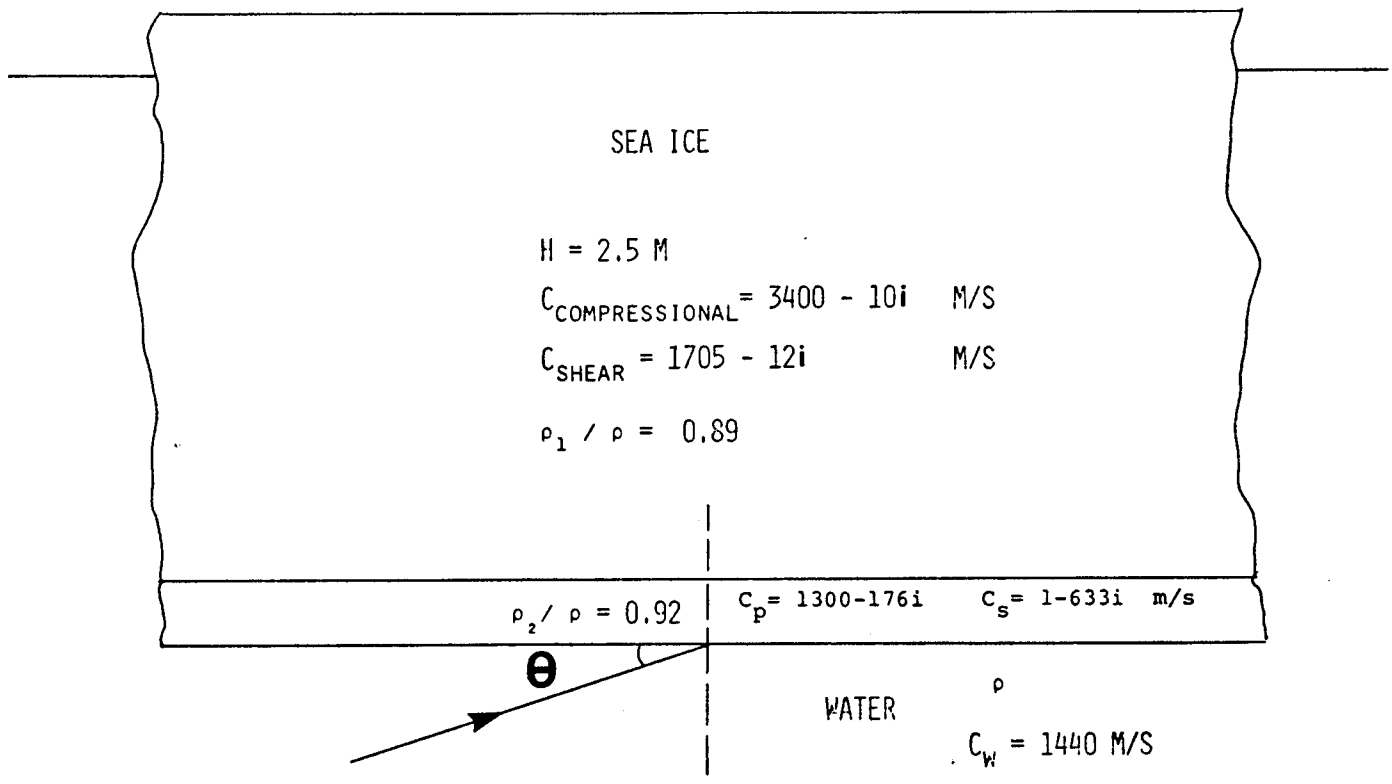


Fig. 4.6 Ice model parameters.

4.1 References

- [4.1] K. Hunkins, "Seismic studies of sea ice," *J. Geophys. Res.* vol. 65, 3459-3472, Fig.12, (1960).
- [4.2] J. R. Chamuel, "Effect of a thin low-velocity layer underneath a floating plate on flexural waves," *J. Acoust. Soc. Am.* 92(4), Pt.2, 2342 (1992).
- [4.3] T. C. Yang and C. W. Votaw, "Under ice reflectivities at frequencies below 1 kHz," *J. Acoust. Soc. Am.* 70(3) 841-851 (1981).
- [4.4] D. L. Folds and C. D. Loggins, "Transmission and reflection of ultrasonic waves in layered media," *J. Acoust. Soc. Am.* 62(5), 1102-1109 (1977).
- [4.5] D. F. McCammon and S. T. McDaniel, "The influence of the physical properties of ice on reflectivity," *J. Acoust. Soc. Am.* 77(2) 499-507 (1985).
- [4.6] C. H. Yew and X. Weng, "A study of reflection and refraction of waves at the interface of water and porous sea ice," *J. Acoust. Soc. Am.* 82(1) 342-353 (1987).
- [4.7] T. K. Stanton, K. C. Jezek, and A. J. Gow, "Acoustical reflection and scattering from the underside of laboratory grown sea ice: Measurements and predictions," *J. Acoust. Soc. Am.* 80, 1486-1494 (1986).
- [4.8] K. L. Williams, G. R. Garrison, and P. D. Mourad, "Experimental examination of growing and newly submerged sea ice including acoustic probing of the skeletal layer," *J. Acoust. Soc. Am.* 92(4), 2075-2092 (1992).
- [4.9] S. A. Chin-Bing, "The effect of physical properties of ice on the high frequency acoustic backscatter from an ice keel model," *Proceedings of the Arctic Oceanography Conf. & Workshop, June 11-14, 1985, Naval Ocean Res. and Dev. Activity and Commander, Naval Oceanography Command 59-70 (1985).*
- [4.10] J. W. Posey, G. H. Branch, S. A. Chin-Bing, and G. Tango, "High frequency acoustic reflection from flat sea ice," *Proceedings of the Arctic Oceanography Conference & Workshop, June 11-14, 1985, Naval Ocean Res. and Dev. Activity and Commander, Naval Oceanography Command 80-89 (1985).*
- [4.11] T. N. Lawrence and G. Tango, "Numerical modeling of acoustic ice interaction in the Arctic," *Proceedings of the Arctic Oceanography Conference & Workshop, June 11-14, 1985, Naval Ocean Research and Development Activity and Commander, Naval Oceanography Command 138-148 (1985).*
- [4.12] A. M. Lindrose, "Ultrasonic wave and moduli changes in a curing epoxy resin," *Experimental Mech.* 227-232 (1978).

SECTION 5

5 DISPERSION OF ANTISYMMETRIC EDGE WAVES ALONG APEX OF TRUNCATED ELASTIC WEDGE

5.1 Introduction

Edge waves propagating along the apex of an elastic wedge were discovered in 1972 independently by Lagasse [5.1] and by Maradudin et al. [5.2]. These edge waves will be referred to as wedge waves in this report in order not to confuse them with flexural edge waves propagating along the edge of a plate [5.3-5.5]. The results presented in this section are limited to the study of antisymmetric wedge waves. Fundamental understanding of wedge waves is essential for nondestructive testing, underwater acoustics, acoustoelectronics, seismology, acoustic imaging, and noise control. Wedge waves can propagate for example along edges of propeller blades, finite crystals, cutting tools, mountains, Arctic ice, cracks, airfoils, underwater fins, and ridges.

Lagasse predicted the existence of wedge waves using the finite element method [5.6]. Fig. 5.1 shows Lagasse's results revealing the computer-generated wave motion along the wedge apex and the velocity of antisymmetric wedge modes plotted as function of wedge apex angle θ . Lagasse obtained an empirical relationship for the antisymmetric wedge mode velocity

$$V = V_R \sin(n\theta), \quad n = 1, 2, 3, \dots, \quad n\theta < 90^\circ$$

where V_R is the Rayleigh wave velocity on a half-space, and n is an integer representing the mode order. The antisymmetric wedge modes are nondispersive and the number of existing

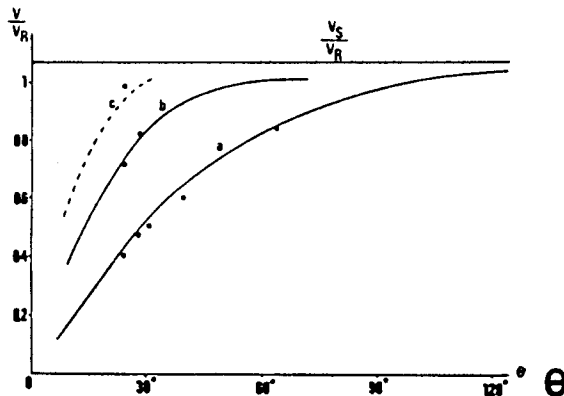
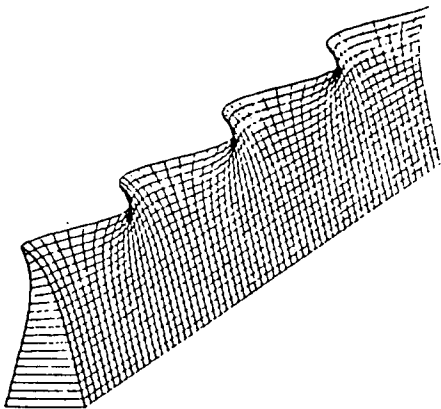


Fig. 8. The effect of varying apex angle on the propagation velocity of the three lowest order nondispersive wedge waves. Curves were computed using fourth-order finite elements for Duralumin 175. Circles represent experimental results.

Fig. 5.1 Wave motion and velocity of antisymmetric flexural wedge waves plotted as function of apex angle θ . [Copied from P.E. Lagasse, Reference 5.6].

modes depends on Θ . As the wedge apex angle decreases, the number of antisymmetric wedge modes increases. Experimental results using broadband pulses were presented in References [5.5 and 5.13]. Quantitative studies [5.4, 5.7, 5.8] revealed that a more accurate wedge mode velocity was obtained when V_R in the above equation was replaced with the edge Rayleigh wave velocity V_{RE} existing along the edge of a quarter-space ($\Theta = 90^\circ$).

Other studies on wedge waves have been reported in several papers. Krylov and Raguzina [5.9] investigated the scattering of wedge waves by notches. Krylov and Shanin [5.10] determined the effect of anisotropy on wedge waves. Krylov [5.11] investigated curved wedges and wedges with arbitrary cross-section. Krylov and Parker [5.12] developed a theory for nonlinear interactions of wedge waves. Chamuel [5.13] investigated the effect of water loading on wedge waves, range-dependent apex angle [5.7-5.8] and immersed 90° wedge [5.5]. Jia et al. [5.14 - 5.15] observed unexplained dispersive behavior of flexural wedge waves using laser generation and detection.

McKenna et al. [5.16] and Lagasse [5.17] obtained theoretical and numerical results demonstrating the influence of apex truncation on dispersion of antisymmetric wedge modes. Fig. 5.2 shows a normalized phase velocity curve, copied from Reference [5.16], for the lowest order mode on a truncated wedge plotted as function of $X_0\beta$, where X_0 is the distance from the "ideal" apex to the truncated apex surface, and β is the wavenumber. Quantitative

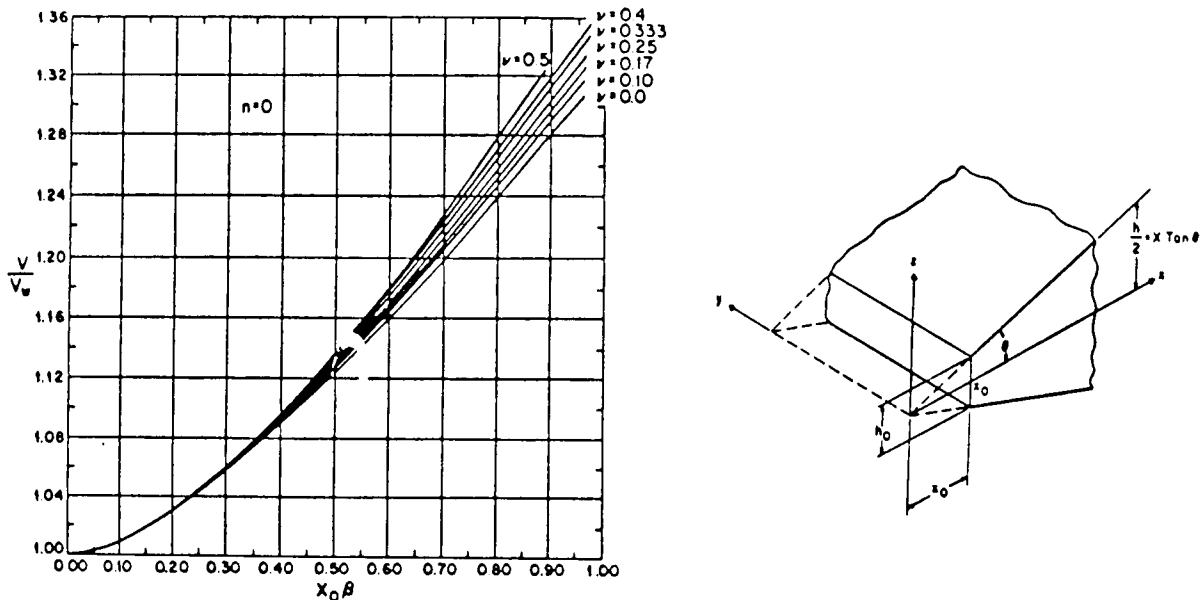


Fig. 6. Normalized phase velocity for the lowest order mode on a truncated wedge as functions of $x_0\beta$ in the interval [0, 1] for $\nu = 0.0, 0.1, 0.17, 0.25, 0.333, 0.4, 0.6$.

Fig. 5.2 Phase velocity for the lowest order anitymmetric flexural wedge mode propagating along apex of truncated wedge. [Copied from McKenna et al., Reference 5.16].

experimental results obtained using laser ultrasonics [5.14-5.15] produced dispersion behavior of antisymmetric wedge modes not predicted by theoretical models. The purpose of this section is to present quantitative experimental results characterizing the dispersion of antisymmetric wedge waves propagating along wedges with truncated apex using contactless electromagnetic acoustic detection. Contactless electromagnetic acoustic detection of antisymmetric wedge waves provided dispersion results in agreement with the theoretical predictions by McKenna et al. [5.16].

5.2 Experimental setup

Aluminum 6061 was used to fabricate a wedge with an apex angle $\theta = 26.7^\circ$. The dimensions of the wedge were chosen to separate in time any wave reflections from the surfaces and corners of the wedge base and sides. Ultrasonic wedge waves were generated with a 1.5 mm diameter compressional piezoelectric transducer positioned to excite flexural antisymmetric wedge modes. A contactless broadband electromagnetic acoustic transducer was used to detect the wedge waves propagating along the apex. The principle of electromagnetic acoustic transducers was described in a paper by Thompson [5.19]. The geometrical configuration of the detector was a U shaped loop similar to the one described in Reference [5.20] for magnetostrictive ultrasonic models. The received signal was displayed on a digital oscilloscope. Waveform and dispersion data were obtained from the initially sharp wedge (3 μm apex) representing the "ideal" wedge. The apex was then truncated successively in steps, and corresponding dispersion results were recorded.

5.3 Results

Waveforms of the antisymmetric flexural wedge modes were obtained with the source excited with a single broadband pulse. Phase velocity dispersion plots were obtained from gated sinusoidal signals (30-500 KHz) and wavelength measurements were averaged over 10-20

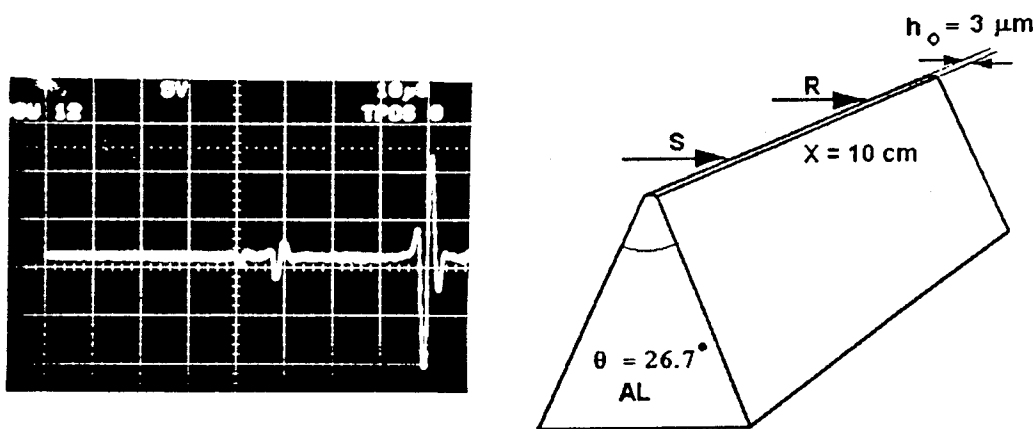


Fig. 5.3 Experimental setup configuration and waveform of nondispersive antisymmetric flexural wedge waves from sharp aluminum wedge with $h_0 = 3 \mu\text{m}$.

wavelengths. The received waveform from the sharp wedge ($h_o = 3 \mu\text{m}$) is displayed in Fig. 5.3. Three practically nondispersed pulses were received representing the three allowed modes for the 26.7° wedge. The distance X between source and receiver was 10 cm. Fig. 5.4 shows dispersed waveforms obtained from the truncated wedge with $h_o = 88 \mu\text{m}$ at $X = 14.5$ and $X = 20.5$ cm. A highly dispersive wavetrain was produced by the truncated wedge with $h_o = 200 \mu\text{m}$ (Fig. 5.5). The single broadband pulse was transformed into this highly dispersive wavetrain.

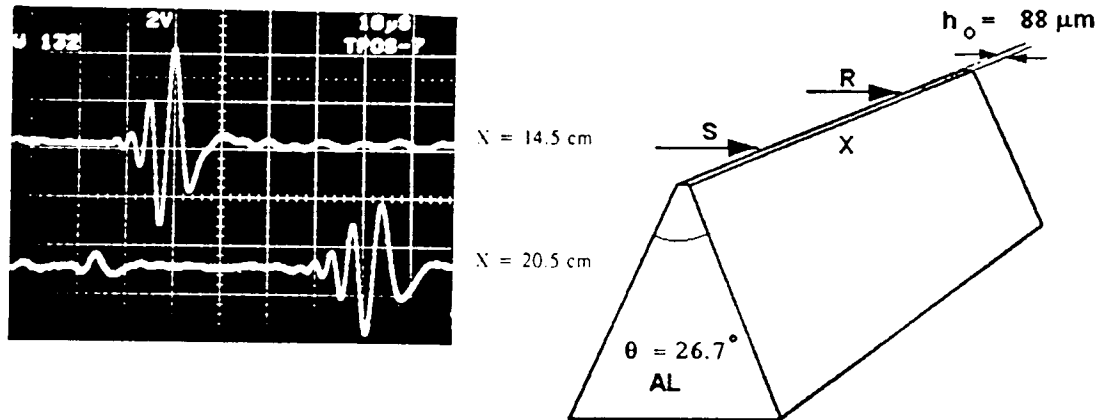


Fig. 5.4 Waveform of dispersed slowest antisymmetric flexural wedge wave from truncated apex ($h_o = 88 \mu\text{m}$).

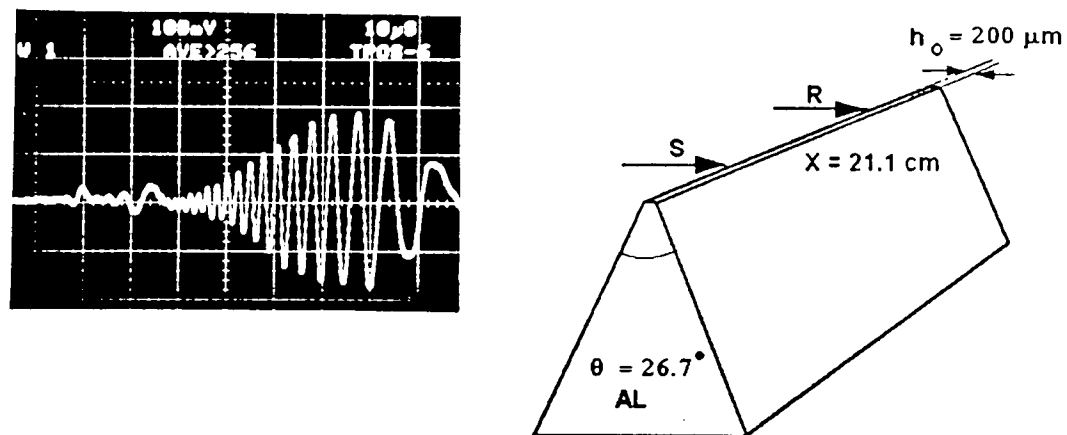


Fig. 5.5 Waveform of highly dispersed antisymmetric flexural wedge wave from truncated apex ($h_o = 200 \mu\text{m}$).

Fig. 5.6-5.9 show the measured dispersion of antisymmetric wedge waves obtained from the 26.7° aluminum wedge truncated with $h_0 = 30, 88, 140,$ and $200 \mu\text{m}$. The ratio of truncated wedge phase velocity V to the "ideal" wedge V_w was plotted as function of frequency. The velocity of the high frequency components increased substantially as h_0 was increased. The repeatability of the velocity data points was better than 10^{-4} up to about 500 kHz. Above 500 kHz, the signal-to-noise ratio dropped drastically and the accuracy of the data points obtained from the truncated wedge with $h_0 = 30 \mu\text{m}$ was questionable (Fig. 5.6). Notice the vertical scale is different in Fig. 5.6-5.9.

In order to compare the experimental results on the effect of apex truncation on the dispersion of the slowest antisymmetric flexural wedge mode with the theoretical predictions by McKenna et al. [5.16], Fig. 5.10 was generated. The ratio V/V_w was plotted vs $X_0\beta$ as presented in Reference [5.16]. The experimental data gathered with the contactless electromagnetic acoustic transducer compared somewhat favorably with the theoretical results. The anomalous laser ultrasonics experimental data described in Reference [5.15] with $\Theta = 30^\circ$ are replotted in Fig. 5.10.

5.3 Conclusions

Accurate quantitative results were presented characterizing the dispersive behavior of antisymmetric flexural wedge waves propagating along the apex of a truncated elastic wedge. Contactless electromagnetic acoustic detection of antisymmetric wedge waves produced dispersion results generally in agreement with theoretical predictions by McKenna et al. [5.16].

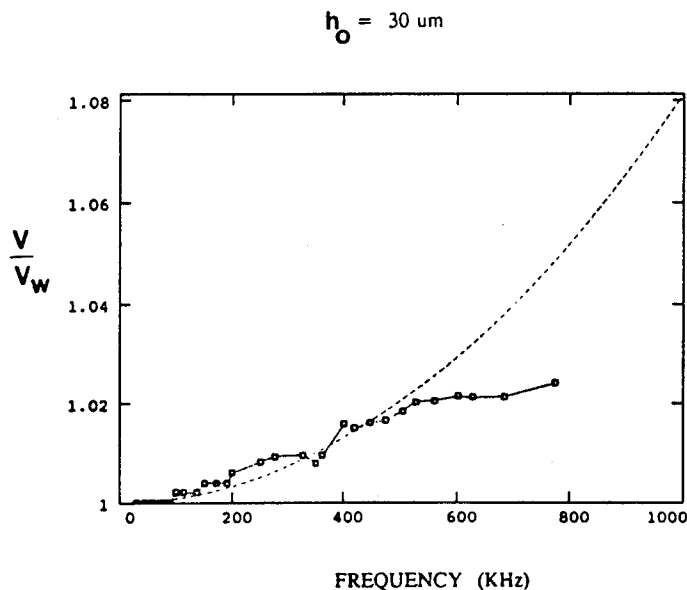


Fig. 5.6 Measured dispersion of antisymmetric wedge waves obtained from truncated aluminum wedge ($h_0 = 30 \mu\text{m}$).

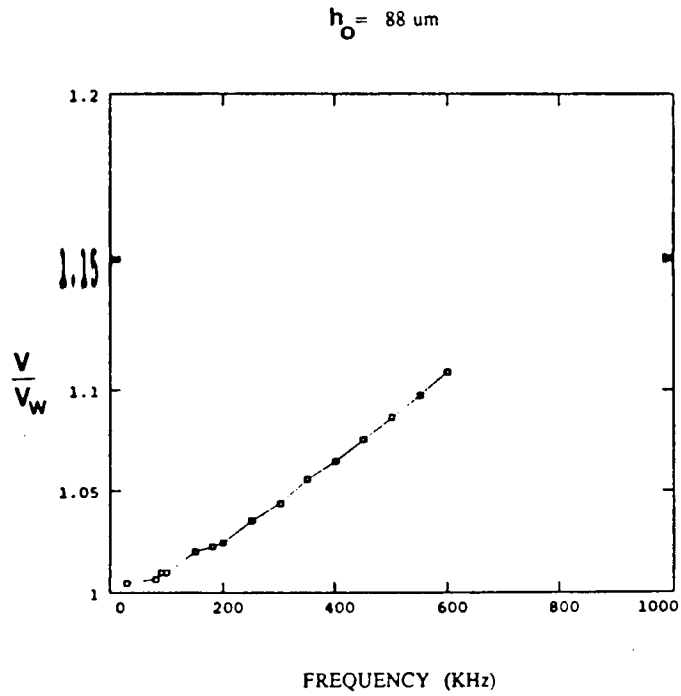


Fig. 5.7 Measured dispersion of antisymmetric wedge waves obtained from truncated aluminum wedge ($h_0 = 88 \text{ } \mu\text{m}$).

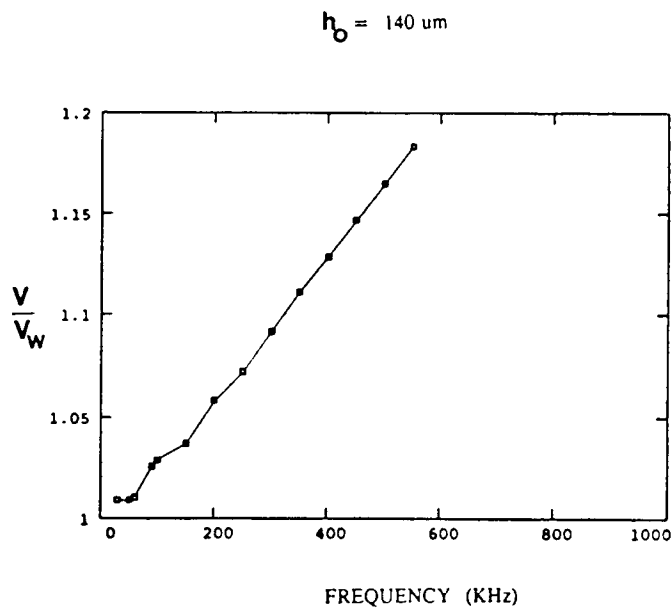


Fig. 5.8 Measured dispersion of antisymmetric wedge waves obtained from truncated aluminum wedge ($h_0 = 140 \text{ } \mu\text{m}$).

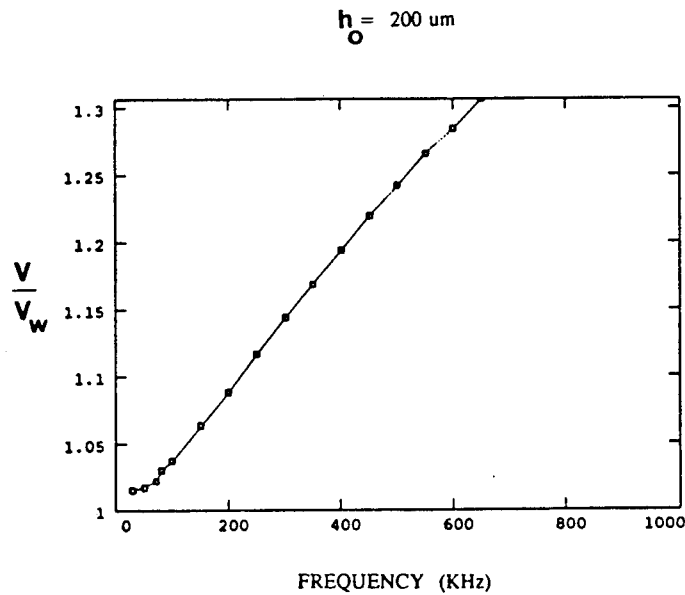


Fig. 5.9 Measured dispersion of antisymmetric wedge waves obtained from truncated aluminum wedge ($h_0 = 200 \mu\text{m}$).

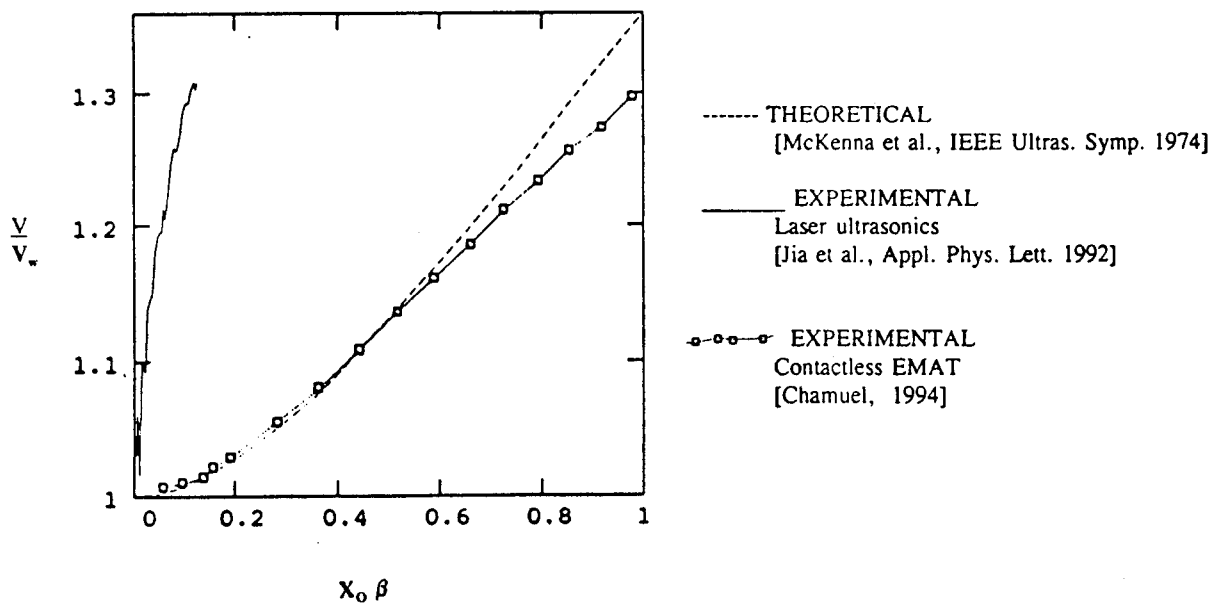


Fig. 5.10 Experimental results on effect of apex truncation on dispersion of the slowest antisymmetric flexural wedge mode compared with theoretical results by McKenna et al. [5.16]. The anomalous laser ultrasonics experimental data with $\theta = 30^\circ$ from Reference [5.15] are also plotted.

5.4 References

- [5.1] P. E. Lagasse, "Analysis of a dispersionfree guide for elastic waves," *Electronics Letters* 8(15) 372-373 (1972).
- [5.2] A. A. Maradudin, R. F. Wallis, D. L. Mills, and R. L. Ballard, "Vibrational edge modes in finite crystals," *Physical Rev. B* 6(4) 1106-1111 (1972).
- [5.3] Y. K. Konenkov, "A Rayleigh-type flexural wave," *Sov. Phys. Acoust.* (6) 122-124 (1960).
- [5.4] R. N. Thurston, "Flexural acoustic waves along the edge of a plate," *IEEE Trans. Sonics Ultrason.* SU-21(4) 296-297 (1974).
- [5.5] J. R. Chamuel, Arctic Acoustics Ultrasonic Modeling Studies, Sonoquest Advanced Ultrasonics Research, Wellesley, Massachusetts, Report No. JRC-10-90, March 1990, NTIS Accession No. ADA224165/1/GAR.
- [5.6] P. E. Lagasse, I. M. Mason, and E. A. Ash, "Acoustic surface waveguides - Analysis and Assessment," *IEEE Trans. Microwave Theory and Tech.* MTT21(4) 225-236, Fig. 8-9 (1973).
- [5.7] J. R. Chamuel, "Range-dependent antisymmetric edge waves along curved elastic wedge with variable cross section," *Review of Progress in Quantitative Nondestructive Evaluation*, Vol. 13, Edited by D. O. Thompson and D. E. Chimenti, Plenum Press, N.Y. 1423-1430 (1994).
- [5.8] J. R. Chamuel, "Edge waves along immersed elastic elliptical wedge with range dependent apex angle," *Proc. IEEE 1993 Ultrasonics Symposium* 313-318 (1993).
- [5.9] V. V. Krylov and I. V. Raguzina, "Scattering of acoustic wedge modes," *Sov. Phys. Acoust.* 34(5) 546-547 (1988).
- [5.10] V. V. Krylov and A. V. Shanin, "Influence of elastic anisotropy on the velocities of acoustic wedge modes," *Sov. Phys. Acoust.* 37(1) 65-67 (1991).
- [5.11] V. V. Krylov, "Wedge acoustic waves: New theoretical and experimental results," *Proc. 2nd Int. Symp. Surface Waves in Solids and Layered Structures and 4th Int. Scientific Conf. Acoustoelectronics 1989*, M. Borisson et al. (ed.), World Scientific, Varana, Bulgaria 174-189 (1990).
- [5.12] V. V. Krylov and D. F. Parker, "Harmonic generation and parametric mixing in wedge acoustic waves," *Wave Motion* 15 185-200 (1992).

- [5.13] J. R. Chamuel, Ultrasonic Studies of Transient Seismo-Acoustic Waves in Bounded Liquid/Solid Interfaces. Sonoquest Advanced Ultrasonics Research, Wellesley, Massachusetts, Report No. JRC-34-91, November 1991, NTIS Accession No. AD-A243441.
- [5.14] X. Jia and M. de Billy, "Observation of the dispersion behavior of surface acoustic waves in a wedge waveguide by laser ultrasonics," *Appl. Phys. Lett.* 61(25) 2970-2972 (1992).
- [5.15] X. Jia, D. Auribault, M. de Billy, and G. Quentin, "Laser generated flexural acoustic waves traveling along tip of a wedge," *Proceedings IEEE 1993 Ultrasonics Symposium*, 637-640 (1993).
- [5.16] J. McKenna, G. D. Boyd, and R. Thurston, "Plate theory solution for guided flexural acoustic waves along tip of a wedge," *IEEE Trans. Son. Ultrason.* SU-21(3) 178-186 (1974).
- [5.17] P. E. Lagasse, M. Cabus, and M. Verplanken, "The influence of truncation on dispersion of wedge guides," *Proceedings IEEE 1974 Ultrasonics Symposium*, 121-124 (1974).
- [5.18] J. R. Chamuel, "Contactless characterization of antisymmetric edge wave dispersion along truncated wedge using electromagnetic acoustic transducer," *J. Acoust. Soc. Am.* 95(5), Pt.2, (1994).
- [5.19] R. B. Thompson, "A Model for the electromagnetic generation and detection of Rayleigh and Lamb waves," *IEEE Trans. Sonics Ultrason.* SU-20(4), 340-346 (1973).
- [5.20] J. R. Chamuel, "Position sensing readout," U. S. Patent No. 4,035,762, Fig. 3(b), 12 July (1977).

SECTION 6

6 ELASTIC WEDGE WITH RANGE-DEPENDENT APEX ANGLE AND CROSS SECTION

The following two papers summarize new findings obtained on edge wave propagation along wedges with range-dependent apex angle and cross section.

6.1 RANGE-DEPENDENT ANTISYMMETRIC EDGE WAVES ALONG CURVED ELASTIC WEDGE WITH VARIABLE CROSS SECTION

Jacques R. Chamuel
Sonoquest Advanced Ultrasonics Research
P.O. Box 153
Wellesley Hills, MA 02181-5339

INTRODUCTION

Flexural waves in isotropic plates are known to be dispersive [1]. Edge flexural waves propagating along the edge of a semi-infinite plate are slower than conventional flexural waves and are also dispersive [2]. The only known nondispersive flexural waves are antisymmetric edge waves propagating along the apex of a sharp elastic wedge discovered by Lagasse [3]. The present paper focuses on antisymmetric edge waves propagating along the apex of an elastic wedge with a range-dependent apex angle. Edge waves exist in a large number of geometrical configurations and may propagate along ridges, faults, propeller blades, sea-ice features, mountain apex, oblique cracks in cores, boreholes intersecting oblique boundaries, ripple marks in sediments, and helical drills. Edge waves can be generated by conventional acoustic sources or by acoustic emission from fractures. This research is aimed at developing fundamental physical understanding of coupling between underwater acoustic waves and elastic waves in finite solids with oblique boundaries and range-dependent effective elastic properties. Results on edge waves along immersed wedges were presented elsewhere [4-5].

WEDGE EDGE WAVES

Along the apex of an elastic wedge, nondispersive localized antisymmetric edge waves (also known as line acoustical waves [6]) exist. Their particle displacement decays exponentially away from the boundary. Of all the different types of elastic waves known, nondispersive wedge edge flexural waves have the highest energy density and largest strain. Lagasse [7] introduced a simple empirical equation for the phase velocity V of each antisymmetric edge mode

$$V = V_R \sin(m\theta), \quad m = 1, 2, 3, \dots, \quad m\theta < 90^\circ \quad (1)$$

where V_R is the Rayleigh wave velocity, θ is the wedge apex angle, and m is the mode order. The author found that a more accurate expression is obtained when V_R in equation (1) is replaced with the slower edge Rayleigh wave velocity V_{RE} existing along the edge of a solid quarter space [8-9], $V = V_{RE} \sin(m\theta)$.

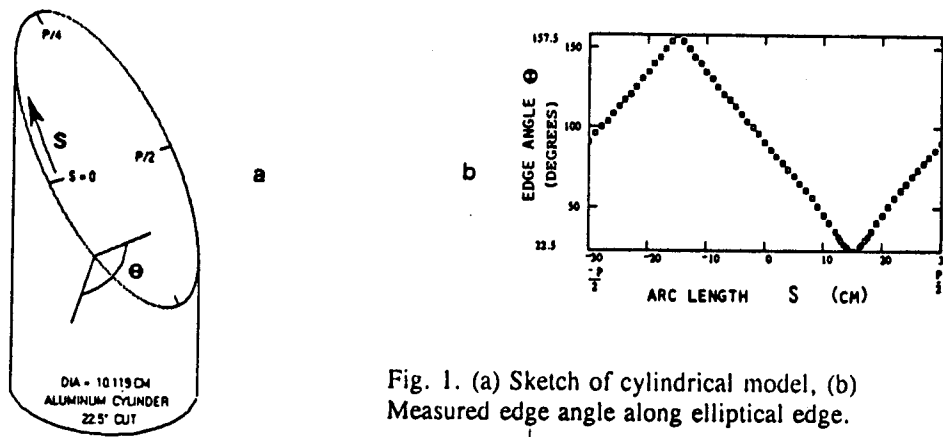


Fig. 1. (a) Sketch of cylindrical model, (b) Measured edge angle along elliptical edge.

EXPERIMENTAL SETUP

The experiments were performed on two basic geometrical configurations: a) truncated obliquely cut cylinder and (b) obliquely truncated borehole. The models were machined from 6061 aluminum. The diameter D of the models was 10.119 cm and the cut was at an angle of $\phi = 22.5^\circ$. Broadband pulsed ultrasonic edge waves were generated and detected using 1.5 mm piezoelectric compressional wave transducers.

RESULTS AND DISCUSSION

Fig. 1 shows a sketch of the cylindrical model and the measured edge angle θ as function of arc length S . The reference point $S = 0$ was located at $\theta = 90^\circ$ with the positive direction towards the acute apex as shown. θ continuously varied between 22.5° and 157.5° . The velocity of antisymmetric edge modes were calculated as function of apex angle for the range-independent flat wedge case (Fig. 2(a)). The ratio of V/V_{RE} was plotted as function of θ up to $\theta = 90^\circ$. Note that the number of wedge modes increased as θ decreased. The waveform of edge waves propagating along the direction of increasing θ were compared with waves along decreasing θ (Fig. 2(b)). The source was located at $S = 0$ ($\theta = 90^\circ$). At $S = -15$ cm, θ was 157.5° and only one edge wave mode propagating near the Rayleigh wave velocity was observed (Fig. 2(b) bottom trace). At $S = +15$ cm, θ was 22.5° and three modes were detected. During the mode conversion process, most of the energy was concentrated in the slowest mode.

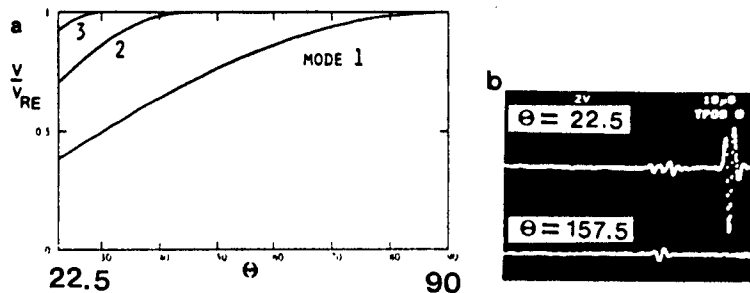


Fig. 2. (a) Velocity of antisymmetric wedge modes as function of flat wedge apex angle, (b) Comparison of edge waves at $S = +15$ cm (top trace) and -15 cm (bottom trace).

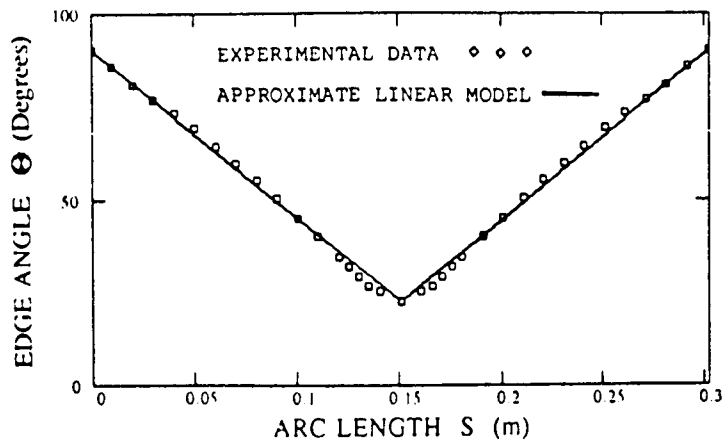


Fig. 3. Measured edge angle vs arc length compared with approximated linear segments.

A plot of the measured edge angle as function of arc length is shown in Fig. 3. Two linear segments were used to approximate $\theta(S)$. For the first quarter of the ellipse,

$$\theta = -7.811S + \pi/2 . \quad (2)$$

Taking x as the principal axis of the ellipse and $x = 0$ at its center, the x -intercepts are $\pm D/2 \sin \phi$. The edge wave velocity was calculated using the approximate linear segments and the modified Lagasse's equation with $V_{RH} = 2886$ m/s (Fig. 4) instead of $V_R = 2951$ m/s. The arc length was determined from the expression

$$S = \int_0^x \left[1 + \sqrt{\sin^2 \phi \left(\frac{D^2}{4x^2 \sin^2 \phi} - 1 \right)} \right]^{-1} dx , \quad (3)$$

and the average edge wave velocity (Fig. 4) was computed from

$$v = S \left[\int_0^S \frac{ds}{V} \right]^{-1} , \quad (4)$$

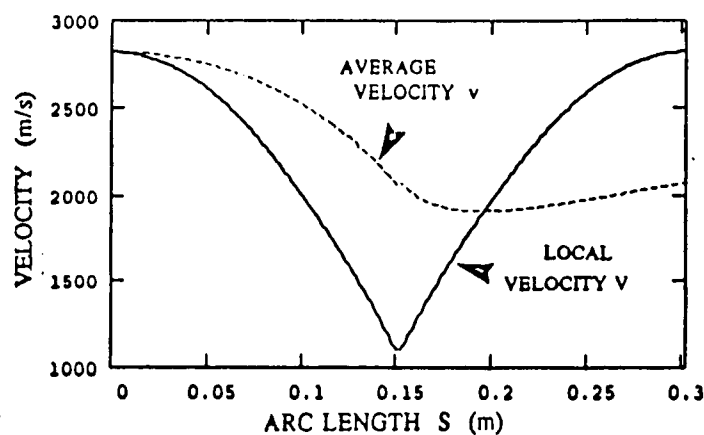


Fig. 4. Calculated edge wave velocity and average velocity for the slowest mode.

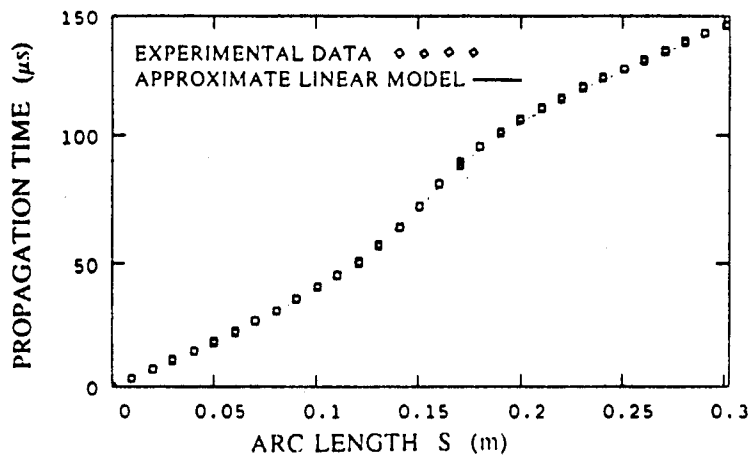


Fig. 5. Comparison of measured and calculated time of arrival of slowest edge wave component.

Fig. 5 reveals the nonlinear characteristics of edge wave propagation time and compares the measured and calculated time $t = S / v$ for the slowest edge wave pulse. Edge waves are elastic waves localized near the edge of the solid and decay exponentially inside the solid. In these range-dependent models, the degree of localization of wedge waves is also variable since it depends on the edge wave velocity. Near $\theta = 22.5^\circ$, the edge wave is more localized than at $\theta = 90^\circ$. Fig. 6 demonstrates the decay of the edge wave with distance from the edge by displaying the spectrum of the slowest edge wave component as function of the distance h from the edge. The high frequency components were attenuated more rapidly than the low frequency components as h was increased.

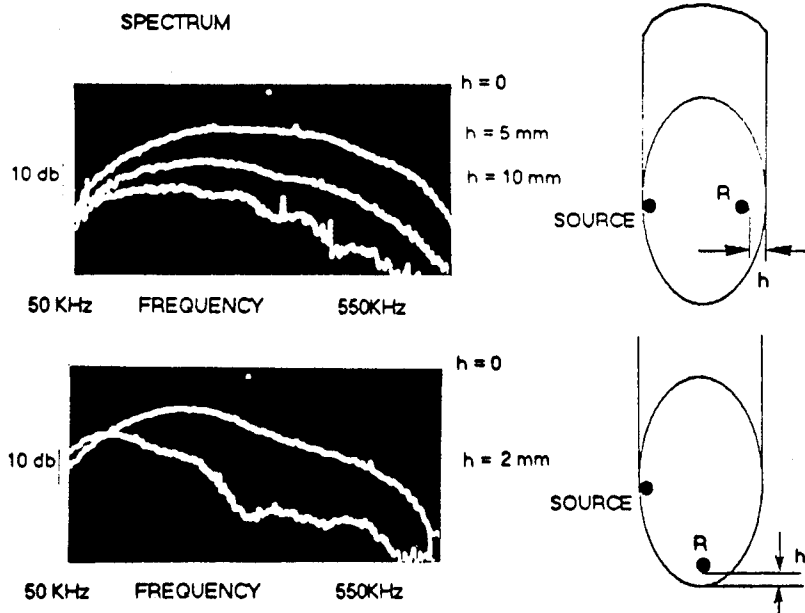


Fig. 6. Decay of edge wave with distance from edge demonstrating localization. Top: at $\theta = 90^\circ$, Bottom: at $\theta = 22.5^\circ$. Note greater localization near acute edge angle.

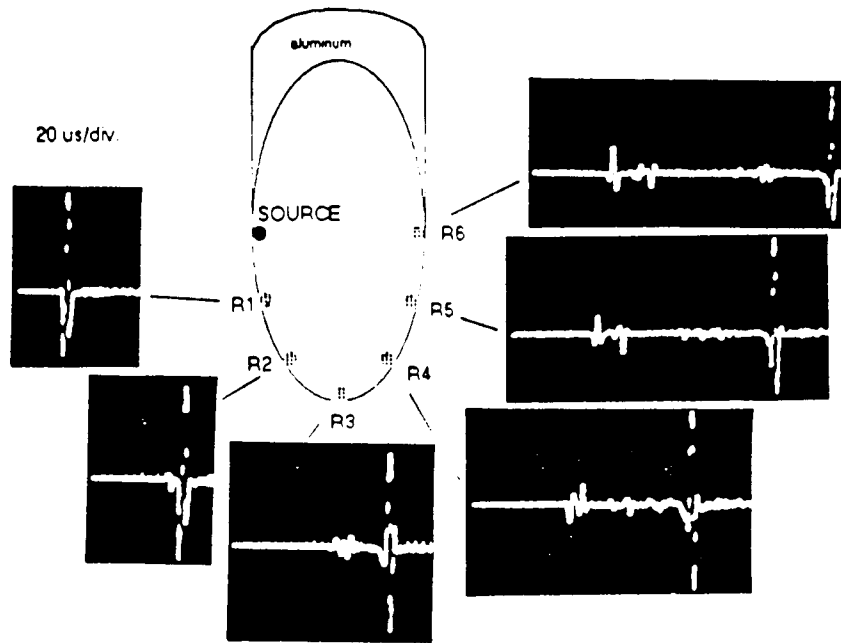


Fig. 7. Waveforms recorded at different ranges along the elliptical path.

A collection of ultrasonic waveforms recorded at different ranges $S = 5, 10, 15, 20, 25,$ and 30 cm is presented in Fig. 7. In addition to the edge waves, a direct Rayleigh wave arriving before the edge waves and propagating across the flat elliptical surface was detected. The waveforms demonstrate the continuous mode conversion as the edge waves propagated from a 90° wedge angle to 22.5° and again to 90° . The relative amplitude of the edge wave particle velocity in the direction normal to the flat plane was measured and plotted as function of S (Fig. 8). The amplitude first increased and then dipped near $\theta = 12^\circ$ - 18° . The waveshape of the slowest edge mode near the acute apex is closely examined in Fig. 9.

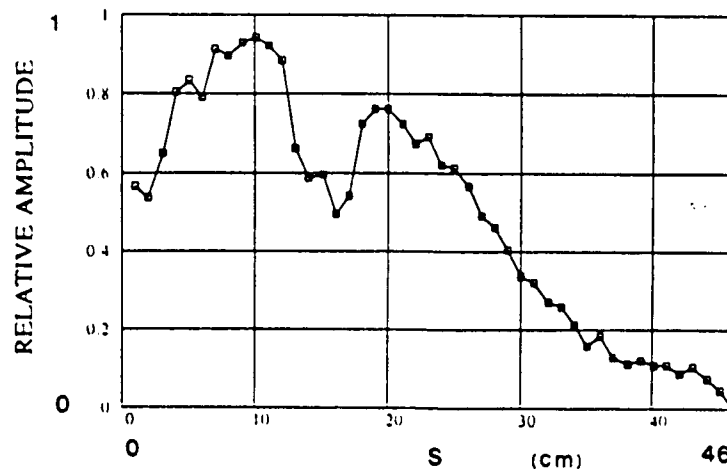


Fig. 8. Measured amplitude of the slowest wave component along the elliptical edge.

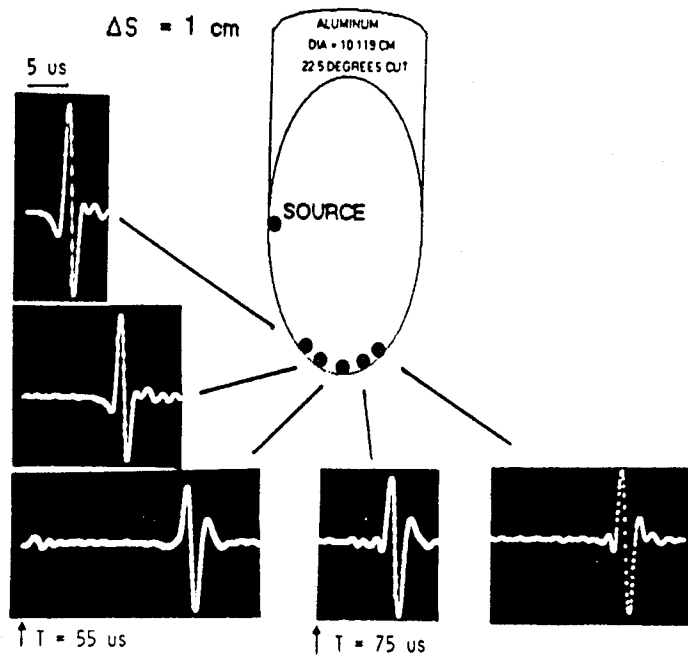


Fig. 9. Waveshape of slowest antisymmetric edge wave near acute angle curved edge.

Experimental results from the elliptical edge of a truncated borehole gave practically the same type of edge wave characteristics in the used frequency range. Time of arrival data from the borehole overlapped the results of Fig. 3(c) from the truncated cylinder. The direct Rayleigh wave component crossing the minor axis of the ellipse was obviously absent in the borehole case. Fig. 10 compares the waveforms obtained from the cut solid cylinder and oblique borehole. A high frequency component was observed at the onset of the waveform from the cylinder. Further studies on edge waves are in progress.

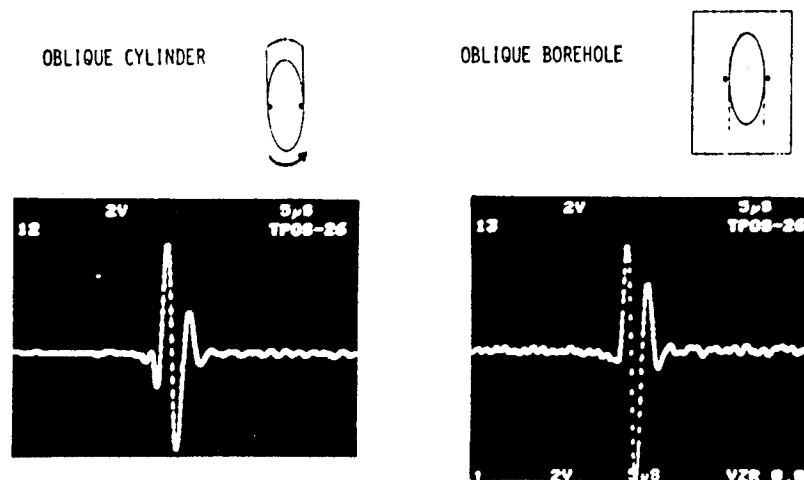


Fig. 10. Comparison of slowest antisymmetric edge wave from oblique borehole and solid cylinder cut at 22.5°. Source located at $S = 0$ and receiver at $S = 30.16$ cm.

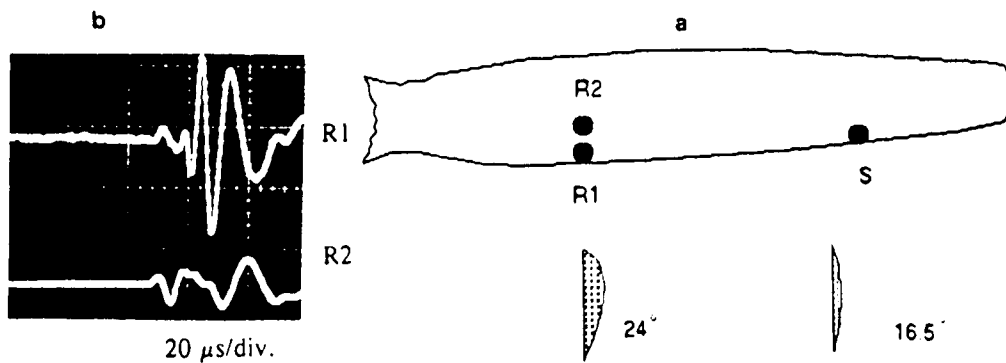


Fig. 11. Range-dependent antisymmetric edge waves along propeller blade edge.

A preliminary experiment was conducted on the edge of a model airplane plastic propeller (Windsor Propeller No.1080) to demonstrate the existence of edge waves (Fig. 11(a)). Source and receiver transducers were placed along an edge of the propeller blade as shown separated by 5 cm. The detected antisymmetric edge wave was large and dispersive. Edge wave dispersion was due to truncation of the propeller edge. Dispersion effects of truncating the apex of a wedge were previously investigated [10-11]. Localization of the antisymmetric edge wave was demonstrated by the large attenuation of the wave as the receiver R2 was placed 7 mm away from the edge (Fig. 11(b)).

SUMMARY AND CONCLUSIONS

This paper presented the first results on range-dependent broadband pulsed antisymmetric edge waves propagating along the sharp edge of a curved elastic wedge with variable cross section. Experimental results from truncated oblique cylinders and truncated oblique boreholes revealed that the velocity, amplitude, and number of existing antisymmetric edge modes continuously changed as the waves propagated along the range dependent edge. The antisymmetric edge waves remained nearly nondispersive over a wide frequency range. For a 10 cm diameter aluminum cylinder obliquely cut at 22.5°, the edge angle around the elliptical path varied almost linearly as function of arc length between 22.5° and 90°. As the apex angle increased, the number of edge modes decreased. An example was given on edge waves propagating along the edge of a propeller. In view of space limitations, several references on edge waves along fixed angle wedges were not mentioned. The reader may refer to publications by Krylov [12]. The new findings contribute to the physical understanding of 3-D range dependent liquid/solid seismoacoustic wave phenomena and propeller noise.

ACKNOWLEDGMENTS

This work was supported by ONR.

REFERENCES

1. K. F. Graff, *Wave Motion in Elastic Solids*, Ohio State University Press (1975).

2. Y.K. Kononkov, "A Rayleigh-type flexural wave," *Sov. Phys. Acoust.* 6, 122-3, (1960).
3. P. E. Lagasse, "Analysis of a dispersion-free guide for elastic waves," *Electronics Letters*, 8(15), 372-373 (1972).
4. J. R. Chamuel, *Ultrasonic Studies of Transient Seismo-Acoustic Waves in Bounded Solids and Liquid/Solid Interfaces*, Sonoquest Advanced Ultrasonics Research Report No. JRC-34-91, November 1991. Available from National Technical Information Center, U.S. Dept. of Commerce, document No. AD-A243441.
5. J.R. Chamuel, "New range-dependent antisymmetric edge waves along immersed curved elastic wedge with variable cross section," *J. Acoust. Soc. Am.* 93(4), 2321 (1993).
6. S. Datta and B. J. Hunsinger, "Analysis of line acoustical waves in general piezoelectric crystals," *Physical Review B* 16(10), 4224-4229 (1977).
7. P.E. Lagasse, I. M. Mason, and E. A. Ash, "Acoustic surface waveguides-analysis and assessment," *IEEE Trans. Microwave Theory and Tech.* MTT21(4), 225-236 (1973).
8. J. R. Chamuel, *Arctic Acoustics Ultrasonic Modeling Studies*, Sonoquest Advanced Ultrasonics Research report no. JRC-10-90, March 1990. Available from National Technical Information Center, U.S. Dept. of Commerce, No. ADA224165/1/GAR.
9. J. R. Chamuel and G. H. Brooke, "Propagation of Rayleigh and Scholte waves along edge of quarter-space," *J. Acoust. Soc. Am. Suppl.* 1, 85, S88 (1989).
10. J. McKenna, G. D. Boyd, and R. N. Thurston, "Plate theory solution for guided flexural acoustic waves along the tip of a wedge," *IEEE Transactions on Sonics and Ultrasonics* SU-21(3), 178-186 (1974).
11. P.E. Lagasse, M. Cabus, M. Verplanken, "The influence of truncation on dispersion of wedge guides," *IEEE 1974 Ultrasonics Symposium*, 121-124 (1974).
12. V. V. Krylov, "Wedge acoustic waves: New theoretical and experimental results," *II International Symposium on Surface Waves in Solids and Layered Structures and IV International Scientific Tech. Conf. Acoustoelectronics '89*, Varna, Bulgaria, World Scientific 174-189 (1989).

Jacques R. Chamuel

Sonoquest Advanced Ultrasonics Research
P.O. Box 153, Wellesley Hills, MA 02181-5339

ABSTRACT

Experimental results are presented revealing the characteristics of wedge waves propagating along the edge of free and immersed curved elastic wedges with variable cross section and range-dependent apex angle. Broadband pulsed wedge waves from the elliptical edge of obliquely cut solid cylinders and boreholes are compared. The velocity and number of existing edge modes continuously vary along the wave path. Leaky edge waves radiate in the water with continuously varying angles depending on the local edge wave velocity. Antisymmetric edge waves remained nearly nondispersive over a wide frequency range. The new findings provide physical insight in understanding range-dependent liquid/solid wave phenomena and propeller noise.

INTRODUCTION

Nondispersive flexural wedge waves propagating along the apex of an ideal sharp elastic wedge were discovered in 1972 by Lagasse [1] and have been studied by several researchers since [2]. The terms edge or wedge waves will be used interchangeably in the text. The particle displacement of these localized nondispersive antisymmetric edge waves decays exponentially away from the boundary. Of all the different types of elastic waves known, nondispersive wedge flexural waves have the highest energy density and largest strain. The present paper focuses on curved elastic wedges with variable cross section and range-dependent apex angle. Wedge waves exist in a large number of geometrical configurations and may propagate along ridges, sea-ice features, mountains, oblique cracks in cylindrical cores, oblique boundaries intersecting boreholes, ripple marks in sediments, helical drills, and propeller blades. Edge waves may be generated by conventional acoustic sources or by acoustic emission from cracking. This research is aimed at developing fundamental physical understanding of the coupling between underwater acoustic waves and elastic

waves in finite solids with oblique boundaries and range-dependent effective elastic properties. Other results on wedge waves were presented elsewhere [4-5].

Lagasse [1] introduced a simple empirical equation for the phase velocity V of each antisymmetric edge mode

$$V = V_R \sin(m\theta), \quad m = 1, 2, 3, \dots, \quad m\theta < 90^\circ \quad (1)$$

where V_R is the Rayleigh wave velocity, θ is the wedge apex angle, and m is the mode order. According to (1), the velocity of each antisymmetric mode is independent of frequency, and it decreases as the wedge angle is decreased. The author found that a more accurate expression is obtained when V_R in equation (1) is replaced with the slower edge Rayleigh wave velocity V_{RE} existing along the edge of a solid quarter space [5], $V = V_{RE} \sin(m\theta)$.

In addition to the antisymmetric wedge modes, symmetric edge waves with a velocity close to the Rayleigh wave can also exist.

EXPERIMENTAL SETUP

The experiments were performed on three basic geometrical configurations: a) a reference model consisting of a conventional triangular wedge with a fixed apex angle, b) a truncated obliquely cut cylinder and (c) an obliquely truncated borehole. The models were machined from 6061 aluminum. The triangular wedge had an apex angle $\Theta = 26.72^\circ$. The borehole and cylinder had the same diameter $D = 10.119$ cm and the cut was at an angle of $\phi = 22.5^\circ$. Broadband pulsed ultrasonic edge waves were generated and detected using 1.5 mm diameter piezoelectric compressional wave transducers.

RESULTS AND DISCUSSION

I. Fixed Wedge Angle

Antisymmetric edge waves were generated in the triangular wedge with the transducers oriented perpendicular to the apex to transversally excite the flexural wedge waves Fig. 1(a). Three antisymmetric modes were detected, however the slowest mode (mode 1) was very dispersive mainly due to the finite truncation of the wedge apex ($30 \mu\text{m}$). The effect of apex truncation on the dispersion of flexural wedge waves was previously investigated [7-8]. By sharpening the wedge, the dispersion was significantly reduced (Fig. 1(b)). The triangular wedge was fabricated by diagonally cutting and machining a 7.5 cm thick aluminum plate. The measured Rayleigh wave velocity on one face of the wedge was 0.56% smaller than the other side. Observed dispersive behavior of laser generated antisymmetric wedge waves were reported [9]. Symmetric edge waves were generated with the transducers oriented parallel to the apex (Fig. 2). The first observed pulse was a longitudinal wave followed by a large symmetric edge Rayleigh wave. The source/receiver distance x was 25.5 cm.

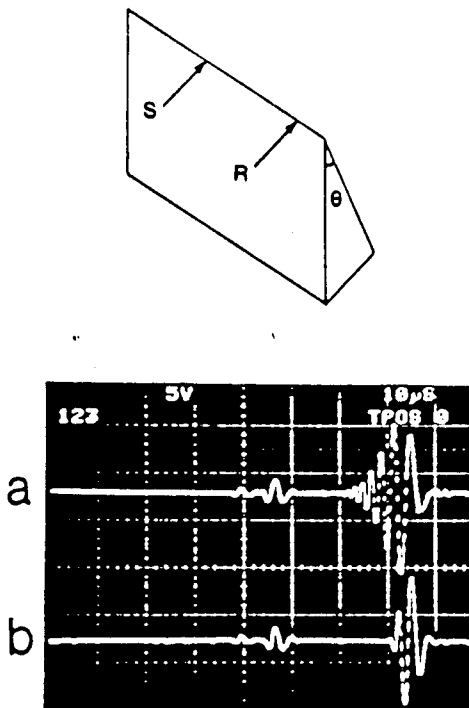


Fig. 1. Effect of wedge apex truncation on antisymmetric edge waves. Top: $30 \mu\text{m}$ wedge tip thickness. Bottom: sharp wedge tip.

Sonoquest JRC-36-94

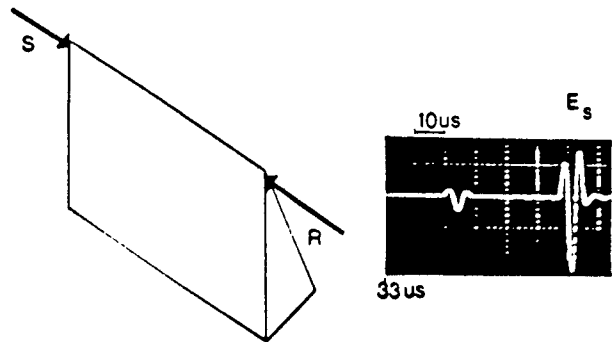


Fig. 2. Symmetric wedge waves.

II. Range-Dependent Wedge Angle

Fig.3 shows a sketch of the obliquely cut cylindrical model. The measured edge angle θ as function of arc length S is plotted in Fig. 4. θ varied continuously between 22.5° and 157.5° . The reference point $S = 0$ was located at $\theta = 90^\circ$ with the positive direction towards the acute apex as shown. The source was located at $S = 0$ on the edge. The receiver was placed on the flat elliptical surface away from the edge at a distance $r = 9$ cm. A small direct Rayleigh wave was observed as expected (Fig. 5(a)). The receiver was then moved to $S = 9$ cm on the edge to detect the edge wave displayed in Fig. 5(b)). This experiment demonstrates the relative amplitude of the direct Rayleigh wave on the flat surface and the antisymmetric edge wave.

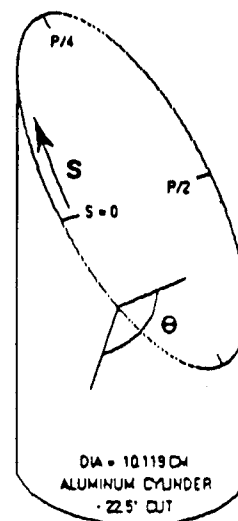


Fig. 3. Sketch of cylindrical model.

J. R. Chamuel

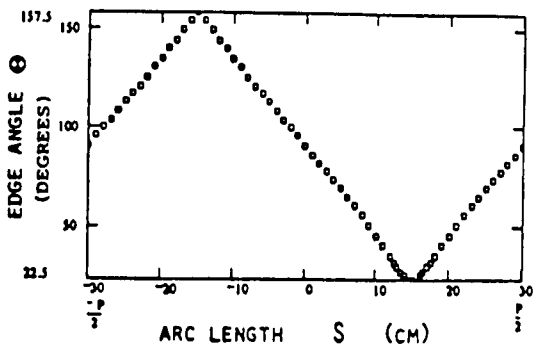


Fig. 4. Measured edge angle as function of arc length.

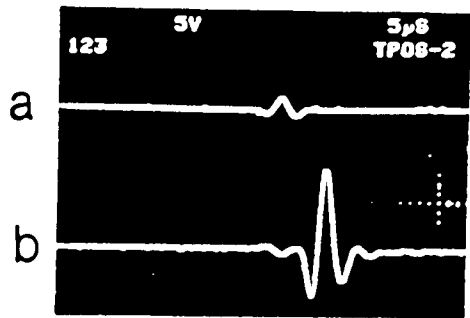


Fig. 5. Comparison of direct R wave and edge wave.

A collection of ultrasonic waveforms recorded at different ranges $S = 5, 10, 15, 20, 25,$ and 30 cm is presented in Fig. 6. In addition to the edge waves, a direct Rayleigh wave arriving before the edge waves and propagating across the flat elliptical surface was detected. The waveforms demonstrate the continuous mode conversion as the edge waves propagated from a 90° wedge angle to 22.5° and again to 90° .

Two linear segments were used to approximate $\theta(S)$. For the first quarter of the ellipse,

$$\theta = -7.811S + \pi/2 .$$

Taking x as the principal axis of the ellipse and $x = 0$ at its center, the x -intercepts are $\pm D/2 \sin \phi$. The edge wave velocity was calculated using the approximate linear segments and the modified Lagasse's equation with $V_{RE} = 2820$ m/s (Fig. 7) instead of $V_p = 2932$ m/s. The arc length was determined from the expression

$$S = \int_0^x [1 + \sqrt{\sin^2 \phi (\frac{D^2}{4x^2 \sin^2 \phi} - 1)}] dx ,$$

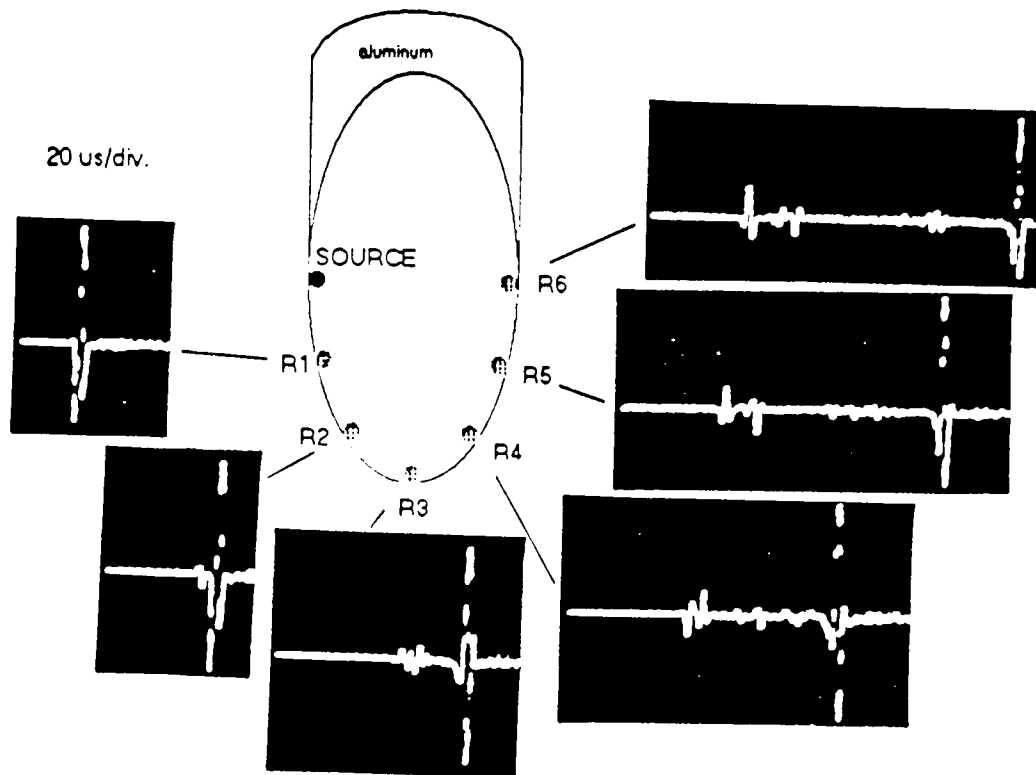


Fig. 6. Waveforms recorded at different ranges.

and the average edge wave velocity (Fig. 7) was computed from

$$v = S \left[\int_0^S \frac{ds}{V} \right]^{-1},$$

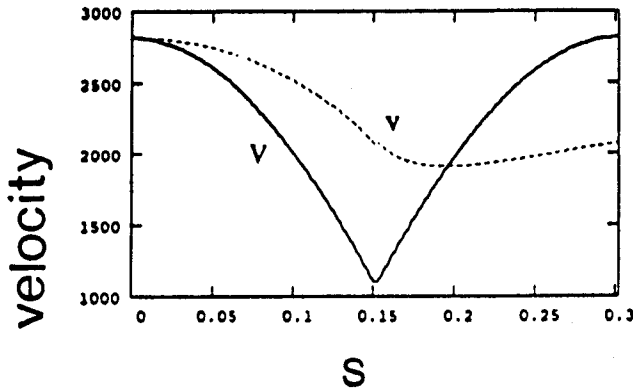


Fig. 7. Calculated edge wave velocity and average velocity for the slowest mode.

Fig. 8 reveals the nonlinear characteristics of edge wave propagation time and compares the measured and calculated time $t = S / v$ for the slowest edge wave pulse. Fig. 9 displays the calculated local velocity of the three antisymmetric modes. Edge waves are elastic waves localized near the edge of the solid and decay exponentially inside the solid. In these range-dependent models, the degree of localization of wedge waves is also variable since it depends on the edge wave velocity. Near $\theta = 22.5^\circ$, the edge wave is more localized than at $\theta = 90^\circ$.

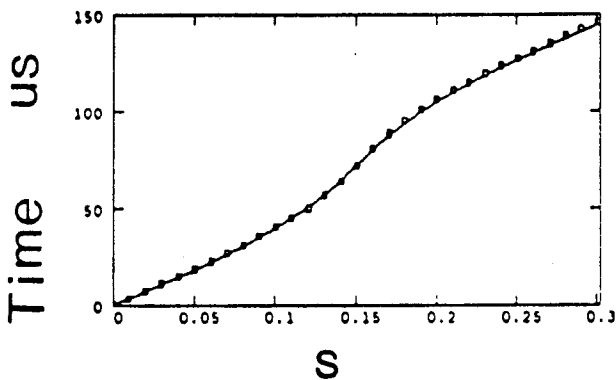


Fig. 8. Comparison of measured and calculated time of arrival of slowest antisymmetric edge wave component.

Sonoquest JRC-36-94

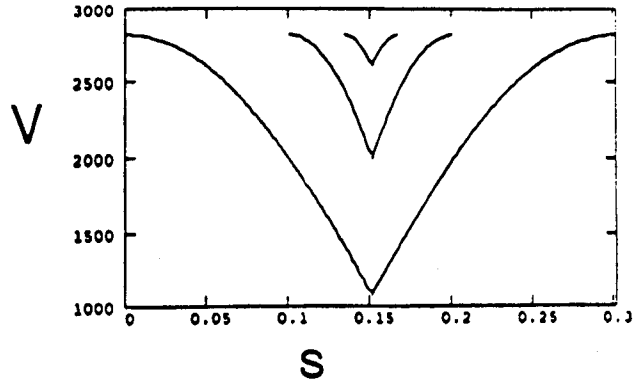


Fig. 9. Calculated local velocity of three antisymmetric edge modes.

Experimental results from the elliptical edge of a truncated borehole gave practically the same type of edge wave characteristics in the used frequency range. Time of arrival data from the slowest borehole mode nearly overlapped the results of Fig. 8 from the truncated cylinder. Fig. 10 compares the antisymmetric edge waves from the cylindrical model (Fig. 10(a)) and borehole (Fig. 10(b)) with $S = 15.08$ cm (one quarter the perimeter). The experiment was repeated with the receiver at $S = 30.16$ cm (Fig. 11). The direct Rayleigh wave component crossing the minor axis of the ellipse was obviously absent in the borehole case. Also the first-arriving antisymmetric edge waves were severely attenuated in the borehole model. This is due to leakage of these waves into body waves due to the curvature of the edge.

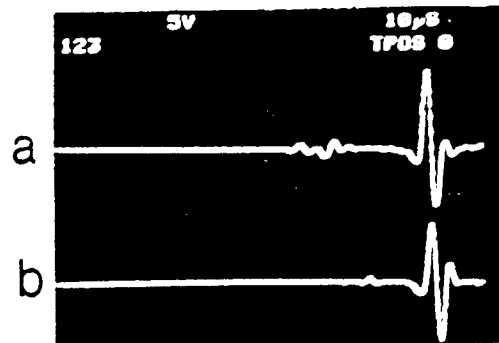
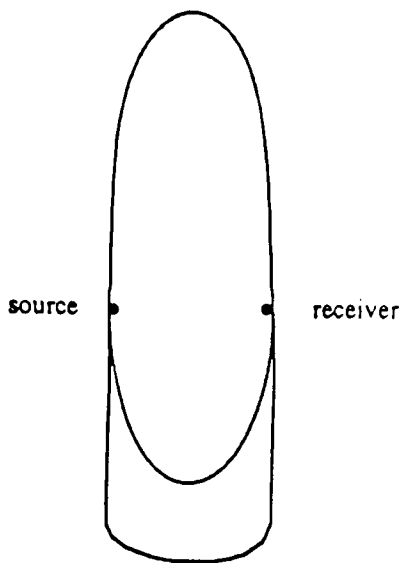


Fig. 10. Comparison of borehole and solid cylinder waveforms of antisymmetric edge waves ($S = 15$ cm).

J. R. Chamuel



Experiments were conducted on the solid cylinder and borehole models to demonstrate the effect of water loading on the slowest antisymmetric edge wave (Fig. 12-13). Water loading decreased the velocity of the slowest flexural mode and also it introduced dispersion and attenuation as shown. In these controlled experiments, the water level was increased to wet a greater portion of the wavepath. The source-receiver range was fixed 30.16 cm. The arc length S' in the figures corresponds to the distance between the source and the water level.

The velocity of the antisymmetric edge waves vary from point to point around the elliptical path. The supersonic antisymmetric wave components leak their energy to the water with different angles that depend on the local velocity. Fig. 14 shows the calculated radiation angle for the fastest mode as function of arc length assuming the free edge wave velocity.

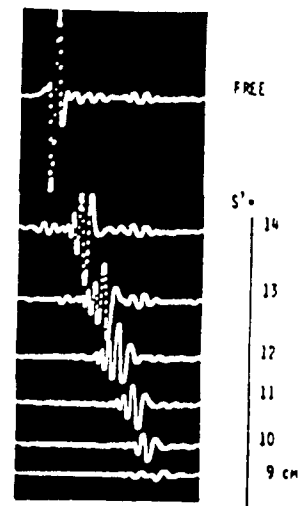
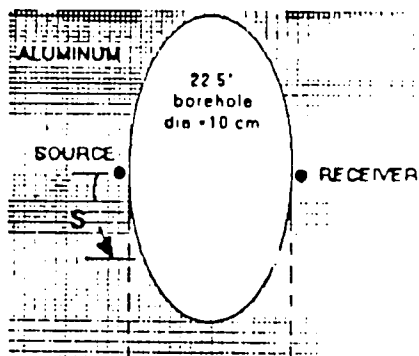
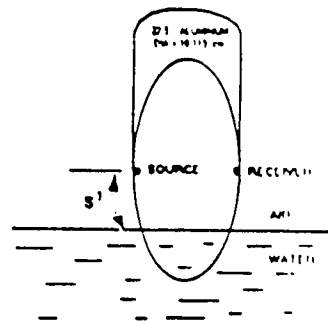
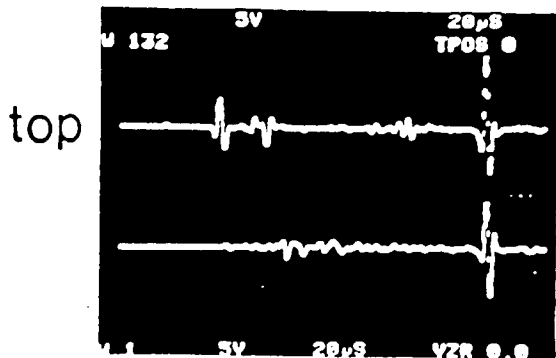


Fig. 11. Comparison of borehole and solid cylinder waveforms of antisymmetric edge waves ($S = 30$ cm).

Sonoquest JRC-36-94

Fig. 12. Effect of water loading on the slowest antisymmetric edge wave component in solid cylindrical model.

J. R. Chamuel

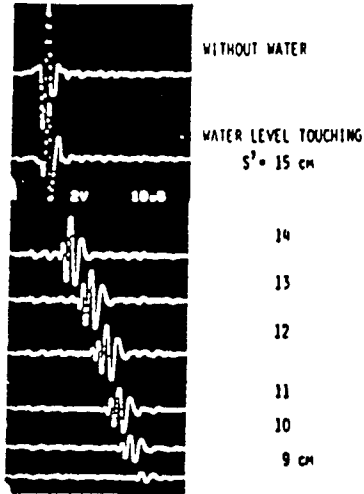
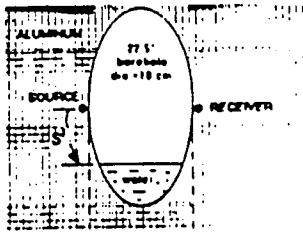


Fig. 13. Effect of water loading on the slowest antisymmetric edge wave component along borehole.

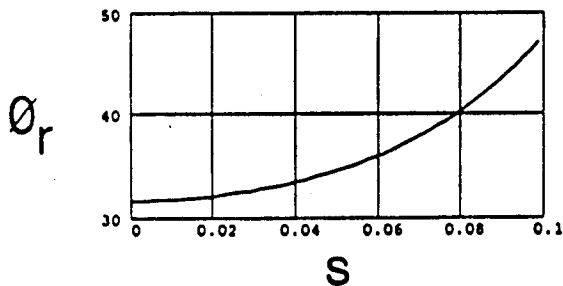


Fig. 14. Calculated radiation angle of supersonic antisymmetric edge waves as function of position along the elliptical wavepath. Aluminum/water model based on free model velocity.

SUMMARY AND CONCLUSIONS

New findings were presented on range-dependent

broadband pulsed antisymmetric edge waves propagating along the sharp edge of a curved elastic wedge with variable cross section. Experimental results from truncated oblique solid cylinders and truncated oblique boreholes revealed that the velocity, amplitude, and number of existing antisymmetric edge modes continuously changed as the waves propagated along the range dependent edge. The antisymmetric edge waves remained nearly nondispersive over a wide frequency range. For a 10 cm diameter aluminum cylinder obliquely cut at 22.5°, the edge angle around the elliptical path varied almost linearly as function of arc length between 22.5° and 90°. As the apex angle increased, the number of edge modes decreased. The effect of water loading on antisymmetric edge waves was demonstrated. The new findings contribute to the physical understanding of 3-D range dependent liquid/solid seismoacoustic wave phenomena and propeller noise.

ACKNOWLEDGMENTS

This work was supported by ONR.

REFERENCES

1. P. Lagasse, "Electron. Lett. 8(15), 372-3 (1972).
2. V. V. Krylov, II Int. Symp. Surface Waves in Solids and Layered Struct. '89, Bulgaria, World Scientific 174-189 (1989).
3. J. R. Chamuel, Ultrason. Studies of Transient Seismoacoust. Waves in Bounded Solids and Liquid/Solid Interfaces, Sonoquest Adv. Ultras. Res., Rep. No. JRC-34-91, Nov.1991. U.S.Dept. of Commerce, NTIS No. AD-A243441.
4. J.R. Chamuel, Review of Progress in Quantitative NDE, Volume 13, '93. Plenum Press, N.Y.
5. J.R. Chamuel, Arctic Acoust. Ultrason. Modeling Studies, Sonoquest Adv. Ultrason. Res. Report no. JRC-10-90, March 1990. U.S. Dept. of Commerce, NTIS No. ADA224165/1/GAR.
6. P. Lagasse, I. Mason, and E. Ash, IEEE Trans. Micro. Theory Tech. MTT21(4), 225-236 (1973).
7. J. McKenna, G. Boyd, and R. Thurston, IEEE Trans. Sonics and Ultr. SU-21(3), 178-186 (1974).
8. P.E. Lagasse, M. Cabus, M. Verplanken, IEEE 1974 Ultrason. Symp. 121-124 (1974).
9. X. Jia and M. de Billy, "Appl. Phys. Letters 61(25), 2970-2972 (1992).

SECTION 7

7 SHEAR WAVE COUPLING TO ICE CORES

One of the greatest difficulties encountered in experimental studies of sea ice is shear wave coupling between transducer and ice [7.1]. Efficient coupling of ultrasonic waves can be achieved by bonding the transducer to the surface of the solid, however, bonding may not be practical in many situations. Coupling of compressional waves can be achieved by using a liquid couplant such as water between the transducer and ice. Shear waves on the other hand are not transmitted through water and a viscous liquid such as honey for example may be used to couple shear waves to ice. Commercially available shear wave couplants (e.g. Panametrics SWC couplant) are not practical for field testing Arctic ice cores at very low temperatures because of their high viscosity and because the ice samples become contaminated. Dry coupling between the ultrasonic transducer and the solid is desirable in several applications such as testing ice cores, however, dry coupling between conventional ultrasonic shear wave transducers and ice allows little energy to be transmitted to the ice.

The author introduced a new technique for dry coupling ultrasonic shear waves between a shear transducer and ice [7.2]. The technique generates and detects shear ultrasonic waves using an abrasive interface layer composed of fine hard particles forming a sandpaper-like surface that causes gripping between the transducer and the solid as a small force is applied to the transducer normal to the surface of the solid.

The proposed method can be implemented by bonding high friction hard particles (e.g. silicon carbide, carborundum, diamond, alumina zirconia, aluminum oxide, etc...) directly to the smooth surface of a conventional ultrasonic shear transducer, or to a wear plate on the surface of the transducer. Another approach is to use a removable double-sided thin sheet coated on both sides with high friction hard particles to be inserted between a conventional ultrasonic shear wave transducer and the solid.

Experimental results verifying the proposed technique are shown in Fig. 7.1. Two identical shear wave transducers (Panametrics V152, 1 MHz, 1" diameter) were placed on opposite ends of a 10 cm thick ice block as shown. The transducers were oriented such that their polarization was in the vertical direction to generate and detect a shear vertical wave in the ice block. The source was excited with a single broadband pulse 2 μ s wide. Fig. 7.1(a) shows the waveform of the received signal (horizontal time scale 10 μ s/div.). The first-arriving pulse was a compressional wave and no significant shear wave was detected. Silicon carbide powder grit 220 was then bonded to the surface of two transducers, and the above experiment was repeated. The received waveform from the transducers coated with silicon carbide powder is displayed in Fig. 7.1(b). The first arriving pulse is a compressional wave and the second large pulse is the desired shear wave.

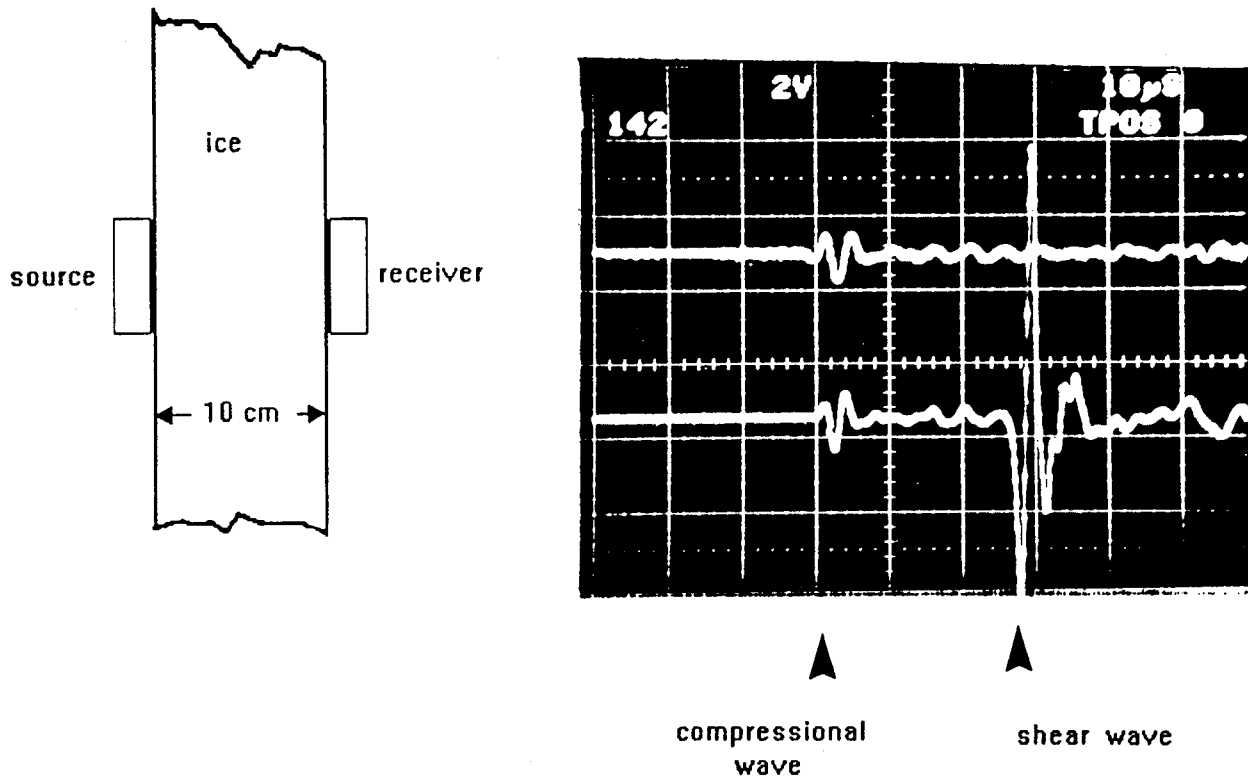


Fig. 7.1 Waveform of elastic waves generated and detected in ice. (a) using conventional shear transducer with smooth surface, (b) using shear transducer coated with silicon carbide powder.

7.1 References

- [7.1] K. L. Williams and R. E. Francois, "Sea ice elastic moduli: Determination of Biot parameters using in-field velocity measurements," *J. Acoust. Soc. Am.* 91(5) 2627-2636 (1992).
- [7.2] J. R. Chamuel, Progress Report No. 1 ONR Contract No. N00014-92-C-0028, Sonoquest Advanced Ultrasonics Research, Wellesley Hills, Massachusetts, Report No. JRC-24-92, 15 April 1992.

SECTION 8

8 ULTRASONIC CHARACTERIZATION OF ARCTIC ICE CORES

In order to develop comprehensive understanding of the physical properties of sea ice, R. Obrochta/ONR proposed the use of a portable ultrasonic system for field measurements of compressional and shear wave velocities continuously along ice cores to complement other Arctic ice studies. The author investigated a related problem on variations in shear wave velocity in cylindrical ice cores across two orthogonal diametrical paths at a given ice core depth. The purpose of this section is to present laboratory ultrasonic results revealing variations in shear wave velocity across two orthogonal diametrical paths in ice core samples [8.1-8.2].

Sea-ice core samples were provided by W. B. Tucker/ U. S. Army Cold Regions Research and Engineering Laboratory. Shear source and receiver transducers were positioned opposite each other across the core diameter. The source was excited with a 2 μ s broadband pulse and the received waveform was captured by a digital oscilloscope. One of the ice cores from the Beaufort Sea had a shear wave velocity that varied with direction as shown in Fig. 8.1. The diameter in the X direction was 10.38 cm and the shear velocity β was 1730 m/s. The diameter in the Y direction was 10.44 cm and $\beta = 1831$ m/s. Sheets of tiny air bubbles trapped in the ice core caused the observed variation in shear wave velocity.

Source and receiver transducers were shifted vertically by 1 cm along the ice core and the measurements were repeated (Fig. 8.2). The diameter in the X direction was 10.49 cm and $\beta = 1748$ m/s. The diameter in the Y direction was 10.35 cm and $\beta = 1815$ m/s.

The maximum variation in shear wave velocity along two orthogonal directions across the cylindrical core was about 6 % , while the diameter changed by only 1.3 % . The repeatability of the results was better than 5×10^{-4} . It is relevant to mention that typical studies of sea ice shear wave velocity variation with temperature deal with velocity fluctuations of about 5 %.

The previous experiments were repeated on an outdoor-pool sea ice core sample. The outdoor-pool sample was produced in a controlled environment and yielded more uniform shear velocity than the Beaufort sea-ice sample. Typical shear wave velocity variations across two orthogonal diametrical paths are shown in Fig. 8.3. The diameter in the X direction was 9.97 cm and $\beta = 1749$ m/s. The diameter in the Y direction was 9.92 cm and $\beta = 1771$ m/s.

8.1 References

- [8.1] J. R. Chamuel, "Ultrasonic Characterization of Arctic 3-D Transient Seismo-Acoustic Phenomena," in J. Fondrk and K. Dillard, Office of Naval Research Arctic Sciences Program Research Summaries 1992, ONR Report No. OCNR 1125AR93-10, May 1993, pp. 138-140.
- [8.2] J. R. Chamuel, "Ultrasonic modeling of sea ice seismoacoustic wave phenomena," J. Acoust. Soc. Am. 94(3), Pt. 2, page 1760 (1993).

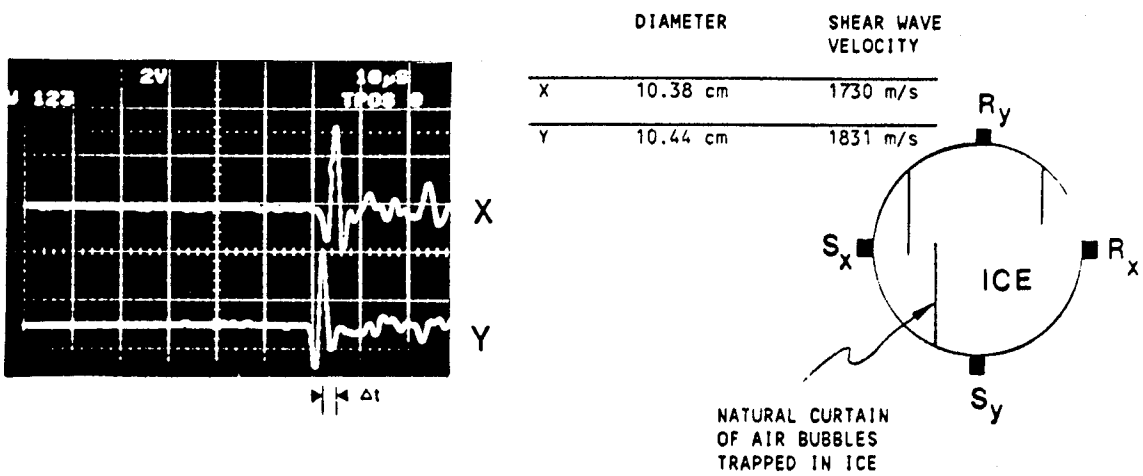


Fig. 8.1. Variation in shear wave velocity across two orthogonal diametrical paths measured from Beaufort Sea ice core sample.

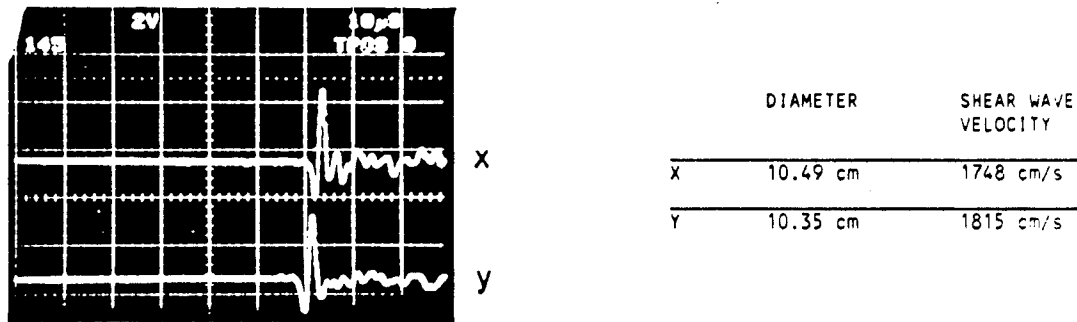


Fig. 8.2. Same as Fig.8.1 measured at $Z = Z_0 + 1$ cm.

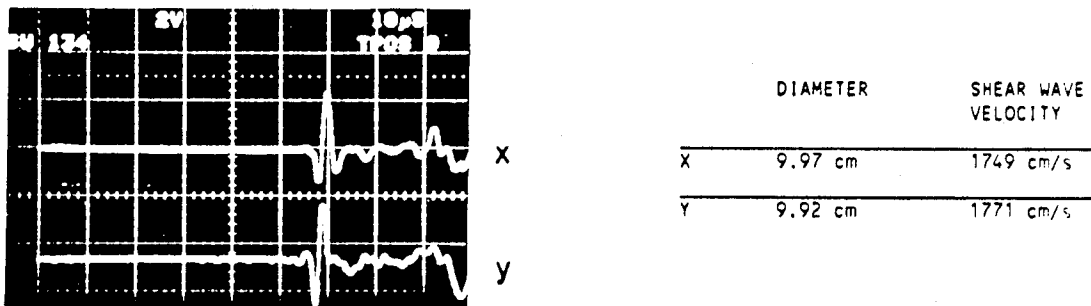


Fig. 8.3. Shear wave velocity results from an outdoor-pool sea ice core sample.

SECTION 9

9 SEISMIC PROFILING USING ONE COMPRESSIONAL TRANSDUCER AND MONOSTATIC SCATTERING FROM 45° OBLIQUE CYLINDRICAL HOLE

9.1 Introduction

Laboratory ultrasonic modeling results are presented demonstrating the use of monostatic scattered waves ($2 < ka < 8$) from a 45° oblique cylindrical hole in a solid to simultaneously determine compressional, shear, and Rayleigh wave velocities [9.1]. A vertical compressional disc transducer placed on the free surface of a solid is used to generate and detect diagonally propagating shear waves created by the vertical displacement of the disc [9.2]. Fig. 9.1 shows a diagram by R. D. Woods [9.3] revealing the diagonally propagated shear waves generated by the vertical displacement of a disc source on an elastic half-space. Backscattering results from 45° oblique boundaries in glass, ice and Plexiglas models are described. Data gathered from layered models show the effect of velocity variation with depth on ray bending and monostatic scattering. The proposed oblique hole monostatic reflection seismology method may be used to determine sea ice shear velocity using only one compressional transducer placed on the free surface of the ice, and a 45° hole bored with a coring machine such as the PICO 45° ice coring rig currently used in sea ice electromagnetic and optical oceanography experiments (W. S. Pegau et al. [9.4]). The wave propagation distance between transducer and reflection point deep inside the ice may be approximated from the free surface yielding accurate one-sided velocity measurements.

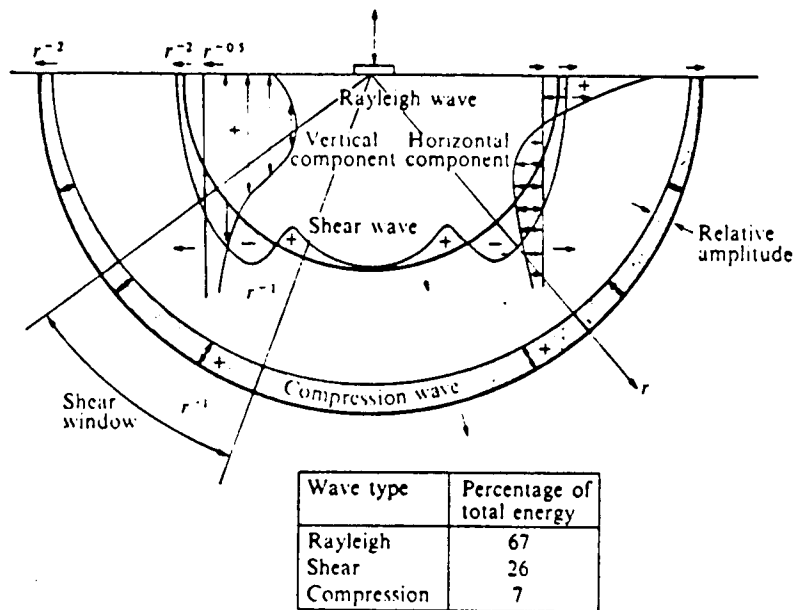


FIG. 6.19. Distribution of displacement and energy in dilatational, shear, and surface waves from a harmonic normal load on a half-space for $\nu = \frac{1}{2}$. (After Woods [44, Fig. 1].)

Fig. 9.1 Elastic waves generated by vertical displacement of disc on a solid half-space. (After R. D. Woods, copied from [9.3]). Note diagonally generated shear wave.

The basic geometrical configuration of the proposed method is diagrammed in Fig. 9.2. The velocity V is determined from the relation

$$V = \frac{X\sqrt{2}}{t}$$

where X is the horizontal distance between transducer and hole top, and t is the round trip propagation time of waves normally incident on the 45° oblique hole. The distance " d " between the transducer and the reflection point along the oblique discontinuity is equal to $0.7071X$. Readers interested in the scattering characteristics of cylindrical discontinuities may refer to papers by R. M. White [9.5] and Beattie et al. [9.6].

Other experimental results are also presented in this section on forward scattering from a combination of oblique and vertical cylindrical holes. The proposed techniques may be applicable to NDE, geophysics, and sea ice characterization.

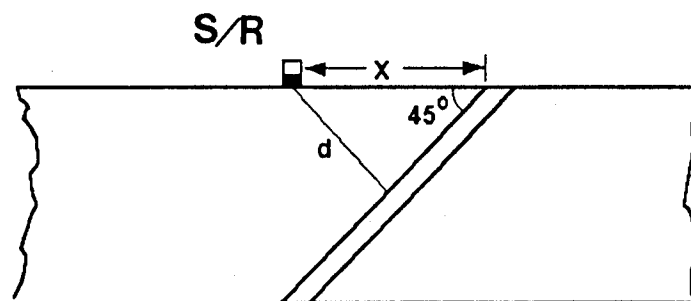


Fig. 9.2 Geometrical configuration of setup.

9.2 Experimental Setup and Results

Ultrasonic models were utilized to gain insight into the problem of monostatic scattering of compressional and shear waves inside a solid by a 45° oblique discontinuity such as a cylindrical hole. The first set of experiments were conducted on 2-D ultrasonic models as described below. A 45° wedge was cut from a 2.15 mm thick glass plate. The glass

wedge was fixed vertically with one edge levelled horizontally, and source/receiver piezoelectric compressional transducer was placed on the horizontal edge at a distance $X = 14.14$ cm from the 45° corner as shown in Fig. 9.3. The selected distance X corresponded to $d = 10$ cm (distance between the transducer and the inclined edge of the wedge). The transducer was excited with a single broadband pulse and the received signal was amplified, filtered, and displayed on a digital oscilloscope. The waveform of the received signal is displayed in Fig. 9.3. The horizontal time scale in the figure is 10 $\mu\text{s}/\text{div}$. Three reflected wave components were detected corresponding to compressional, shear and Rayleigh waves. The compressional and shear waves propagated inside the solid and reflected from point A, while the Rayleigh wave propagated along the horizontal edge and reflected from B. The velocities of the plate compressional, shear, and edge Rayleigh waves were 5415 m/s, 3413 m/s, and 3104 m/s, respectively.

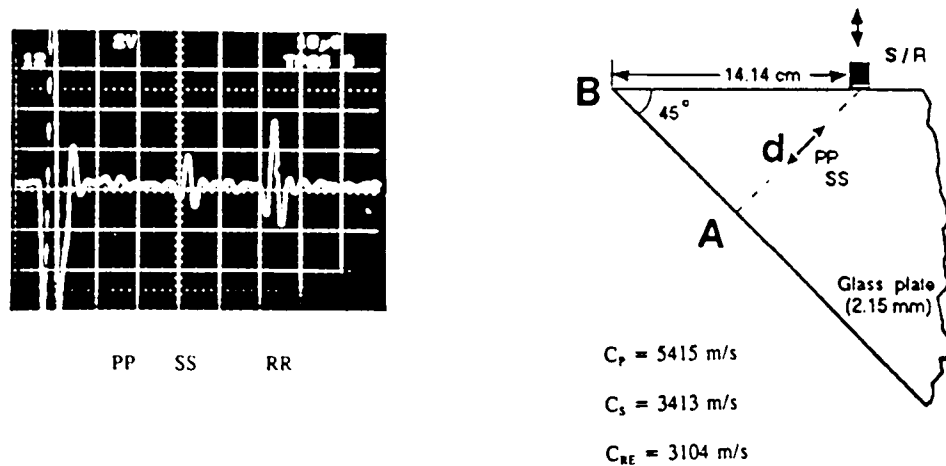


Fig. 9.3 2-D ultrasonic model simulating reflections of compressional, shear, and Rayleigh waves from 45° oblique borehole in solid half-space. Transducer placed along edge of 45° glass plate wedge.

The experiment described above was repeated using a 1 cm thick ice plate. Fig. 9.4 shows the waveform of the PP, SS, and RR wave components measured at $X = 7.07$ cm, 9.89 cm, and 14.14 cm. The measured velocities were 2916 m/s, 1886 m/s, and 1798 m/s for the plate compressional, shear, and Rayleigh waves, respectively. The horizontal time scale in Fig. 9.4 is 20 μ s/div. .

Results from a 3-D ice model are presented in Fig. 9.5. A flat horizontal surface was prepared on a large ice block, a 45° oblique hole was bored, and the source/receiver transducer was placed on the flat ice surface as shown. The horizontal distance between S/R and the hole was 4.5 cm. The source was again excited with a single broadband pulse. PP, SS, and RR waves were observed when the 45° oblique hole was created (Fig.9.5(a)) similar to the previous 2-D models results. Tiny air bubbles and inhomogeneities in the ice block contributed to the complexity of the received waveform. Fig. 9.5(b) shows the reference received waveform obtained from the ice block before introducing the 45° hole. The horizontal time scale in Fig. 9.5 is 10 μ s/div. .

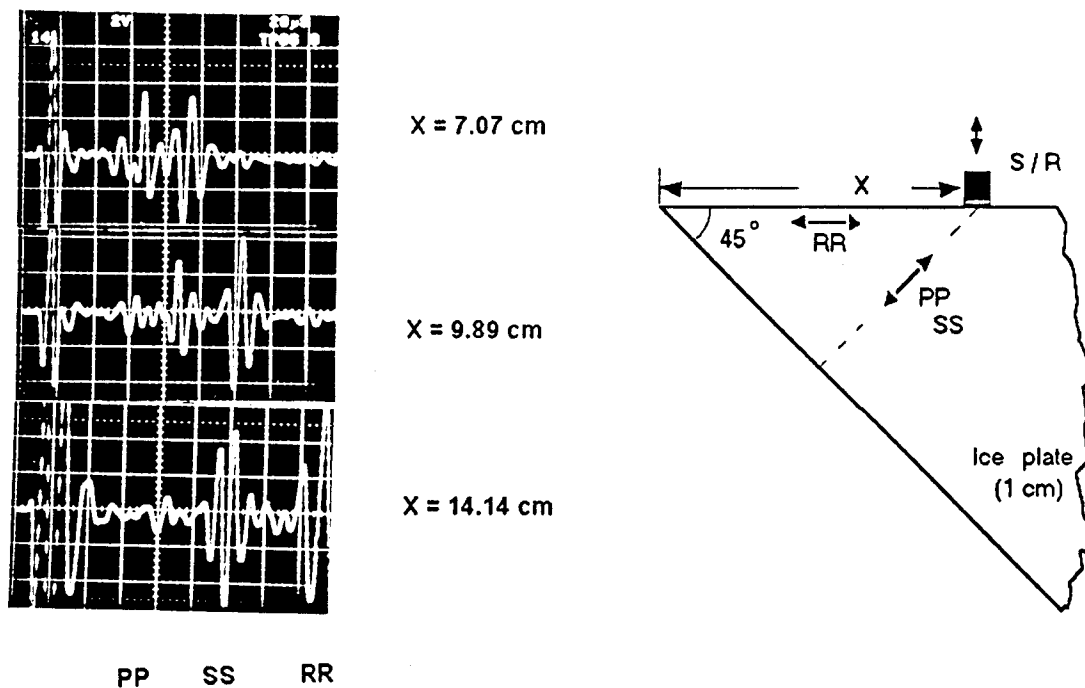


Fig. 9.4 2-D ultrasonic model simulating reflections of compressional, shear, and Rayleigh waves from 45° oblique borehole in solid half-space. Transducer placed along edge of 45° ice plate wedge.

The presence of layers and velocity variation with depth cause ray bending. Results from a layered 2-D ultrasonic model are shown in Fig. 9.6 and Fig. 9.7. The geometrical configuration of the layered model and the elastic properties are presented in Fig. 9.6(a). The model consisted of a 4 cm thick low-velocity layer ($C_{p1} = 4066$ m/s, $C_{s1} = 2207$ m/s) over a high-velocity bottom ($C_{p2} = 4857$ m/s, $C_{s2} = 2957$ m/s). The density ratio was approximately equal to 1. The received waveform is displayed in Fig. 9.6(b). The PP and SS wave components arrived at 45.3 μ s and 79.28 μ s, respectively, matching the calculated results shown in Fig. 9.7. The calculated angle of incidence at the layer bottom interface was 36.29° for the compressional wave and 31.85° for the shear wave. In the layered model, shear and compressional waves reflected from different locations along the 45° oblique boundary.

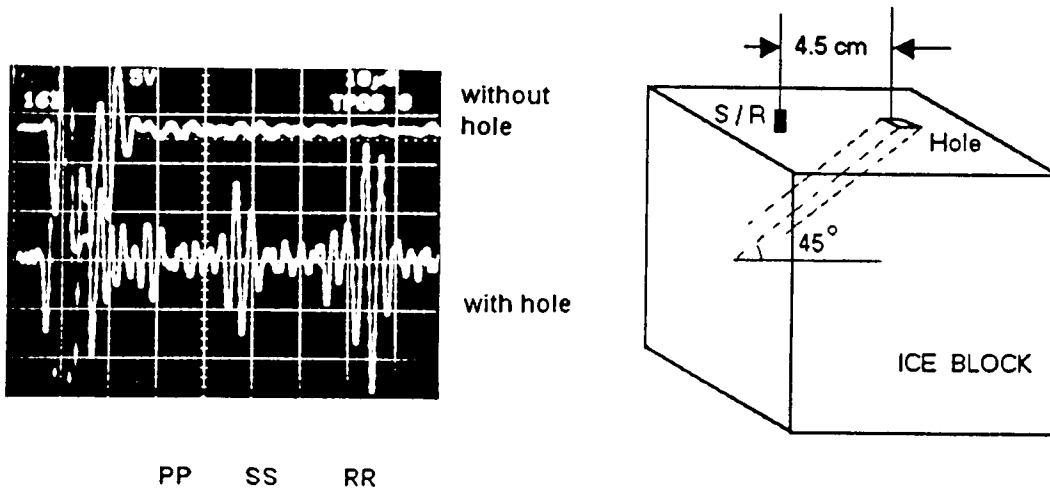


Fig. 9.5 3-D ultrasonic modeling results using 45° oblique hole in ice block.

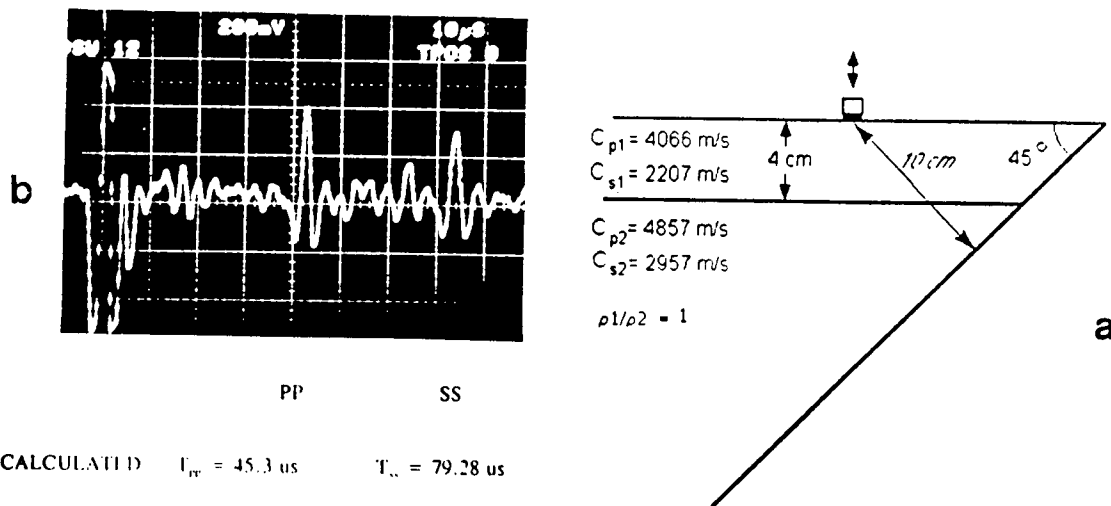


Fig. 9.6 Compressional and shear waves from 2-D layered ultrasonic model.

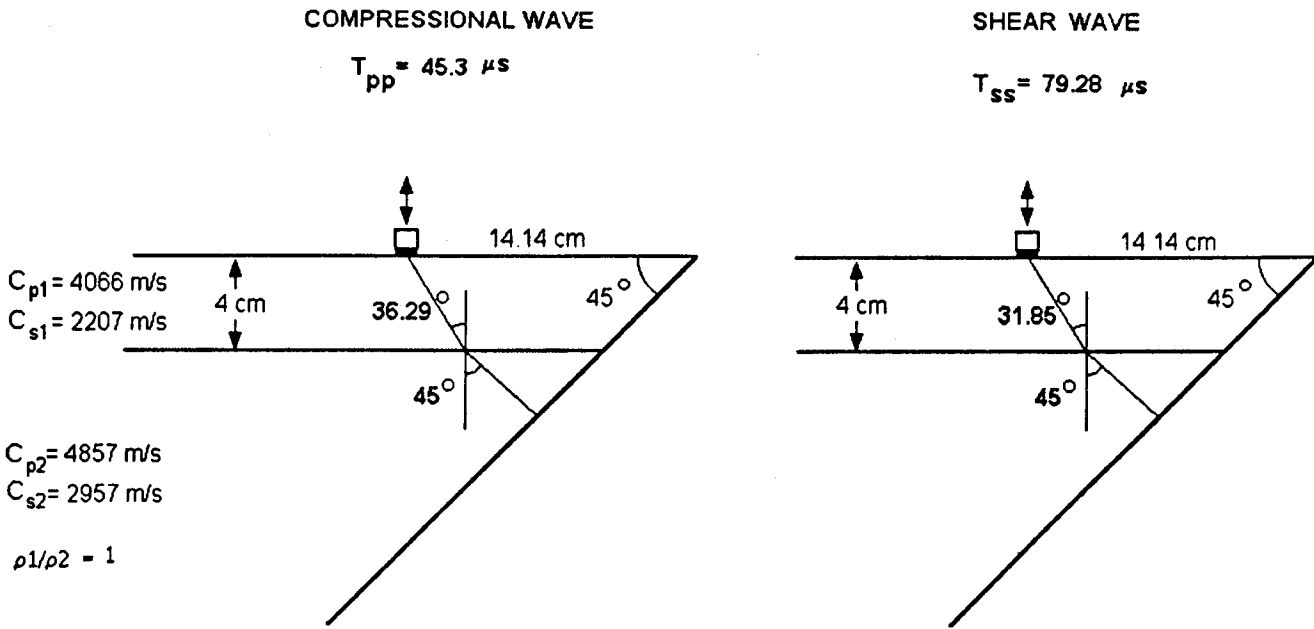


Fig. 9.7 Calculated results for layered model.

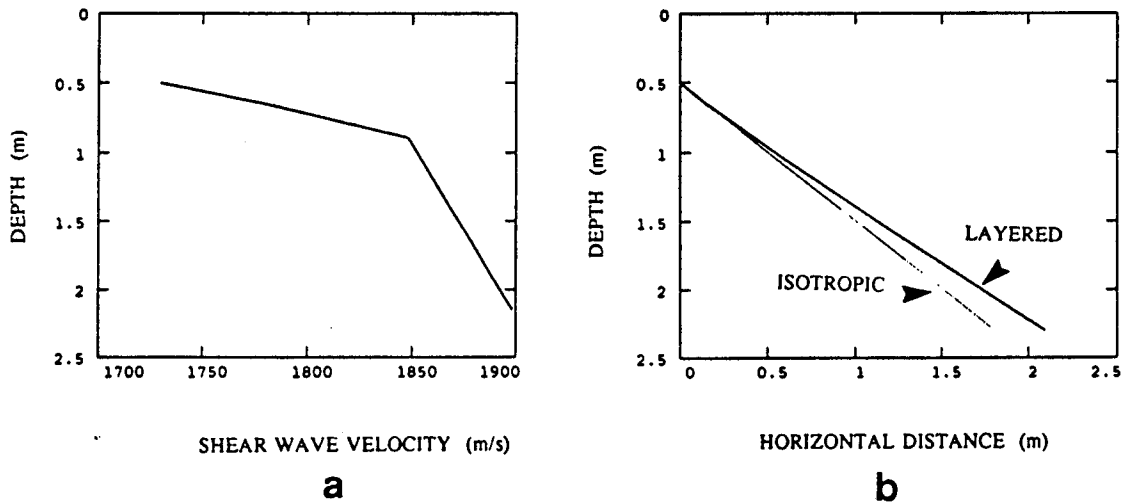


Fig. 9.8 Effect of shear wave variation with depth on ray path.

The effect of shear wave velocity variation with depth on ray bending is demonstrated in Fig. 9.8 using a simplified sea ice velocity profile. The assumed shear wave velocity profile is shown in Fig. 9.8(a). The calculated curved ray path for the depth-dependent shear wave velocity model is plotted in Fig. 9.8(b). These results indicate that shear waves in the depth-dependent model would intersect a 45° boundary at 2 m depth instead of 2.25 m which corresponds to the isotropic model. Further studies are needed to characterize layered models.

Other preliminary experimental results are also presented in this section on forward scattering from a combination of oblique and vertical cylindrical holes in Plexiglas models. An interesting configuration is shown in Fig. 9.9(a) consisting of two intersecting 45° oblique cylindrical holes forming a "V" shaped profile equivalent to a corner reflector. In an isotropic model, when the source and receiver are positioned as shown in Fig. 9.9(a), the total travel time of the waves reflected by the V boundaries is **independent** of the horizontal distance x between source and receiver. The top and bottom traces in Fig. 9.9(b) were recorded with the transducers separated by $x = 2.7$ cm and $x = 6.5$ cm, respectively. Notice the time of arrival of the compressional wave pulse did not change as x was varied.

The previous configuration shown in Fig. 9.9 required two 45° holes and two independent source and receiver transducers. Figure 9.10 presents a different configuration suitable for **monostatic** applications utilizing one 45° hole intersecting one vertical hole as shown and one source/receiver transducer.

9.3 Conclusions

A one-sided velocity profiling measurement technique for simultaneous determination of compressional, shear, and Rayleigh wave velocities using only one compressional source/receiver disc transducer and a 45° oblique cylindrical hole was introduced. Ultrasonic modeling results were presented from isotropic and layered models verifying the implementation of the proposed method.

Potential advantages of the proposed seismic profiling technique include: 1) No instrumentation needed inside the borehole. 2) Only compressional transducers are needed to determine both shear and compressional wave velocities. 3) One-sided accurate velocity measurements may be achieved. 4) Dual use of hardware and 45° oblique holes utilized in sea ice optical oceanography experiments [9.4].

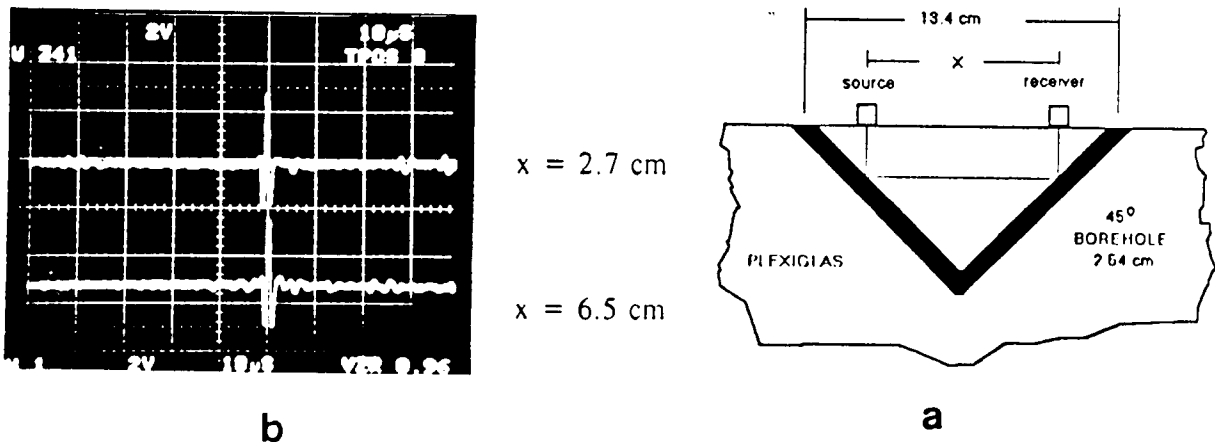


Fig. 9.9 V configuration in Plexiglas model with 45° drilled holes. Notice arrival time of compressional pulse is independent of x .

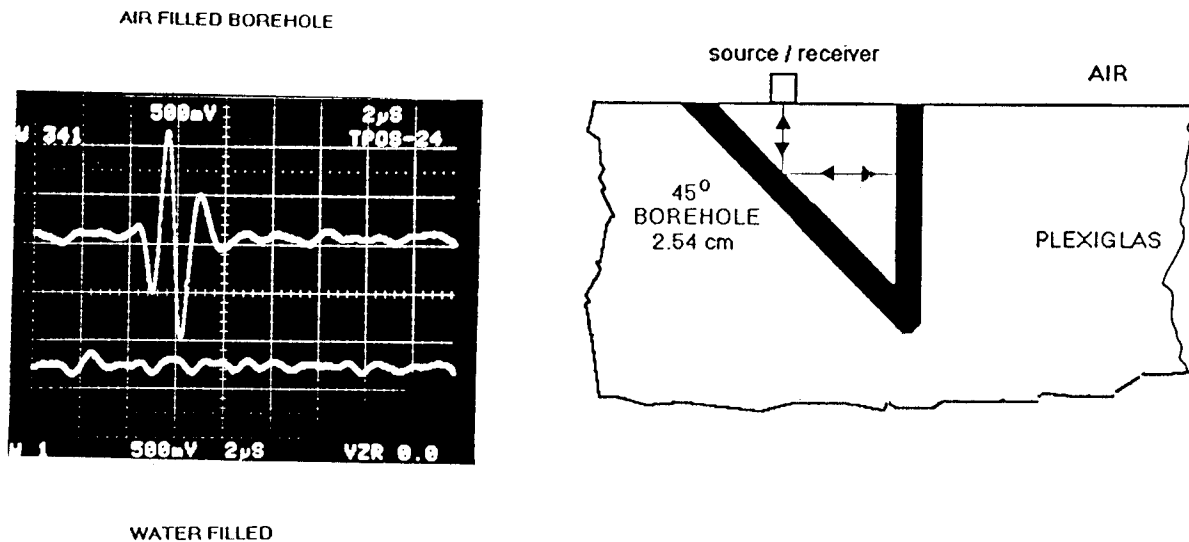


Fig. 9.10 Modified V configuration for monostatic applications. Filling the 6.3 mm dia cylindrical cavities with water drastically reduced the reflected compressional wave.

9.3 References

- [9.1] J. R. Chamuel, "Monostatic seismoacoustic scattering from 45° oblique cylindrical hole in thick floating ice plate," *J. Acoust. Soc. Am.* 95(5), Pt.2, 2883 (1994).
- [9.2] G. F. Miller and H. Pursey, "On the partition of energy between elastic waves in a semi-infinite solid," *Proc. Royal Soc.* A233, 55-69 (1955).
- [9.3] R. D. Woods, "Screening of surface waves in soils," *J. Soil Mech. Founds Div. Am. Soc. Civ. Engrs.* 94 951-979, Fig. 1, (1968). Figure copied from K. F. Graff, "Wave Motion in Elastic Solids," Ohio State University Press, page 356, Fig. 6.19, (1975).
- [9.4] W. S. Pegau, R. A. Maffione, and J. R. Zaneveld, "In-situ profiling system for the measurement of optical properties of sea ice," *Ocean Optics XII*, 13-15 June 1994, Bergen, Norway (1994).
- [9.5] R. M. White, "Elastic wave scattering at a cylindrical discontinuity in a solid," *J. Acoust. Soc. Am.* 30, 771-785 (1958).
- [9.6] P. Beattie, R. C. Chivers, and L. W. Anson, "Ultrasonic backscattering from solid cylindrical inclusions in solid elastic matrices: A Comparison of theory and experiment," *J. Acoust. Soc. Am.* 94(6) 3421-3427 (1993).

SECTION 10

10 SEA ICE FINGER-RAFTING AND ICE THICKNESS

10.1 Introduction

Sea ice finger-rafting is a periodic type of ice structure in the form of periodic parallel fractures often perpendicular to the edges of two adjacent floating thin ice plates with alternating rectilinear overthrusts and underthrusts [10.1]. The fracture pattern is at times so regular that Weeks and Anderson [10.1] mentioned that many of the rectilinear thrusts appear to have been laid out by a draftsman. Fig. 10.1 compares the finger-rafting diagram of Weeks and Anderson with that of Homes and Worthington [10.2] as reported by Dunbar [10.3]. Weeks and Anderson described the formation process as an advancing ice sheet interacting with a stationary fast ice edge, where fracturing occurs only in the moving ice sheet. Homes and Worthington described finger-rafting as fracture and interlocking of two ice edges in refrozen leads. Weber [10.4] and Green [10.5] observed finger-rafting in lakes.

Weeks and Anderson observed that there is no apparent correlation between the ice plate thickness and the width or length of the finger-rafting features. Although Weeks and Anderson did not observe the actual process of finger-rafting formation, they provided an explanation suggesting that the extremely flexible newly formed sea ice transmits water waves. The ragged edge of an advancing ice sheet is deposited on top of another ice sheet by the crest of a water wave. The deposited ice sheet tears, and part of the collapsed portion slides under the fast ice sheet during the following wave trough. The process advances to the adjacent ice edges segments under the continued action of wind and water wave pushing the offshore sheet into the shore fast ice [10.1].

Dunbar [10.3] suggested an explanation for the formation of finger rafting when the water waves move at an angle with respect to the wind direction and are obliquely incident on the adjacent parallel edges of the two ice plates. Dunbar mentioned that the finger-rafting width depends on the wavelength and angle of incidence and will bear no relation to the ice

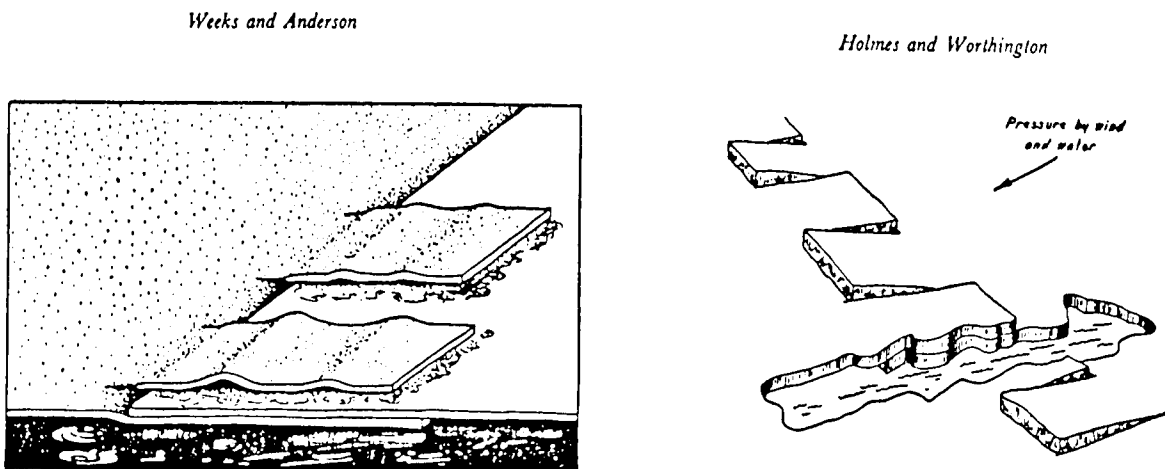


Fig. 10.1 Finger-rafting diagram by Weeks and Anderson [10.1] compared with a diagram by Homes and Worthington [10.2] as reported by Dunbar [10.3].

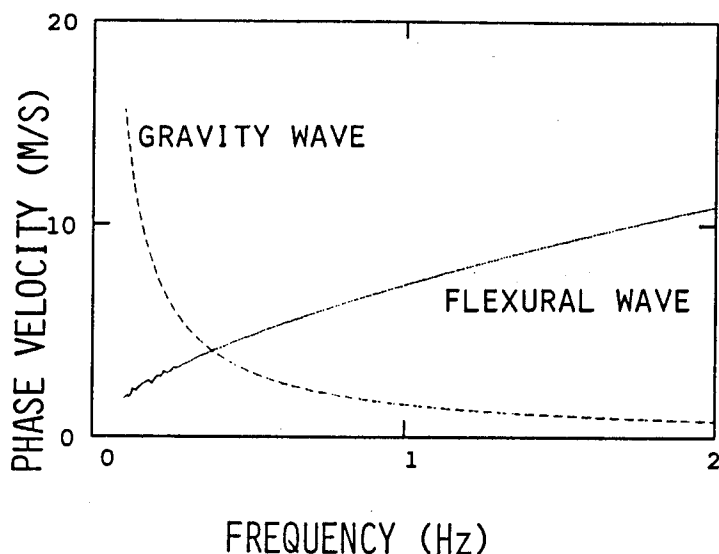


Fig. 10.2 Phase velocities of water gravity wave and flexural wave in floating sea ice plate (5 cm thick) plotted as function of frequency.

thickness. One puzzling detail in Dunbar's paper is in his Figure 10, where the fractures were sketched perpendicular to the plate edges independent of the water wave angle of incidence. Dunbar's explanation of the formation process depends on a propagating process along the ice plate edge originating from one corner of the floating plate and progressing along the edge following the water wave. Physically speaking, the edge of the plate cannot overlap the second ice plate unless the whole plate moves simultaneously along each point along the edge. The ice plate is flexible and can bend vertically, however, it may not be possible to lift one corner of the plate and at the same time elongate the plate to have it deposited on top of the second plate.

10.2 Results

The only known quantitative data on finger-raftering is a single point obtained by J. Morrison [10.7] observed in 5 cm thick sea ice where the measured periodic finger width was 5 m. R. S. Pritchard [10.7] presented a theoretical relationship between finger width and ice plate thickness. Pritchard's calculated finger-raftering-width results were smaller than Morrison's single data point by almost a factor of 5. Other qualitative Arctic field observations by T. B. Curtin (1990-1993) indicated that finger-raftering occurs over a vary wide range of ice thicknesses. For an ice thickness of about 1 m, Curtin observed finger-raftering-width between 50-100 m.

New theoretical results were obtained by the author [10.8] relating finger-raftering-width to ice plate thickness. The results were based on the assumption that when the flexural wave speed in a floating plate (neglecting gravity) is equal to the speed of a water gravity wave component, maximum coupling between the gravity wave and flexural wave occurs. The theoretical results were obtained by calculating the intersection point between the flexural wave phase velocity dispersion curve of a floating ice plate and the phase velocity dispersion curve of water gravity waves calculated at different thicknesses (Fig. 10.2). The gravity wave phase

velocity plot was obtained from the expression:

$$v(f) = g/2\pi f$$

where v is the phase velocity, g is gravity, and f is frequency.

The flexural wave phase velocity was calculated from the characteristic equation [10.9]:

$$\frac{1}{\frac{1}{G(V)} + \frac{1}{D(V)}} - \frac{\rho V^4 \sqrt{1 - \frac{V^2}{\alpha^2}}}{2\beta^4 \sqrt{1 - \frac{V^2}{C^2}}} = 0$$

where c = water compressional wave speed
 α = ice compressional wave speed
 β = ice shear wave speed
 ρ = ratio of water density/ice density

$$G(V) = \frac{4\sqrt{\left(1 - \frac{V^2}{\alpha^2}\right)}\sqrt{\left(1 - \frac{V^2}{\beta^2}\right)}}{\coth\left(\frac{\pi fH}{V}\sqrt{\left(1 - \frac{V^2}{\beta^2}\right)}\right)} - \frac{\left(2 - \frac{V^2}{\beta^2}\right)^2}{\coth\left(\frac{\pi fH}{V}\sqrt{\left(1 - \frac{V^2}{\alpha^2}\right)}\right)}$$

$$D(V) = \frac{4\sqrt{\left(1 - \frac{V^2}{\alpha^2}\right)}\sqrt{\left(1 - \frac{V^2}{\beta^2}\right)}}{\tanh\left(\frac{\pi fH}{V}\sqrt{\left(1 - \frac{V^2}{\beta^2}\right)}\right)} - \frac{\left(2 - \frac{V^2}{\beta^2}\right)^2}{\tanh\left(\frac{\pi fH}{V}\sqrt{\left(1 - \frac{V^2}{\alpha^2}\right)}\right)}$$

The intersection point between the flexural wave phase dispersion curve and the gravity wave dispersion curve yielded the desired phase velocity and frequency from which the wavelength was calculated. Finger-raftering occurs at half this wavelength. The calculated finger-raftering width was plotted as function of ice plate thickness in Fig. 10.3(a). An expanded plot is presented in Fig. 10.3(b) indicating that for 5 cm thick ice, the calculated finger-width is 5.3 m. Morison's data point and Pritchard's theoretical results were also plotted in Fig. 10.3(b) for comparison. The parameters used in the calculations were as follows: ice compressional wave velocity = 3130 m/s, ice shear wave velocity = 1670 m/s, water/ice density ratio = 1.025, water compressional wave velocity = 1440 m/s, gravity = 9.80665 m/s². Numerical results indicated that increasing the elastic parameters of the ice to

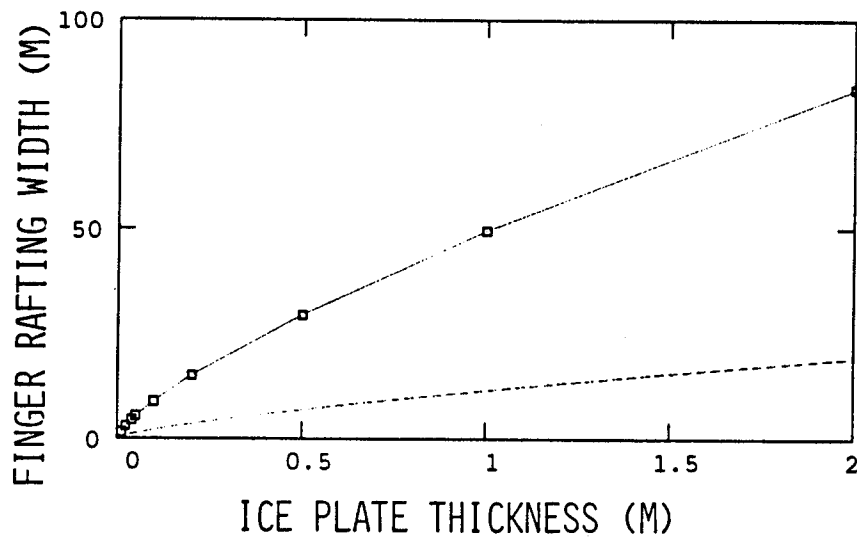
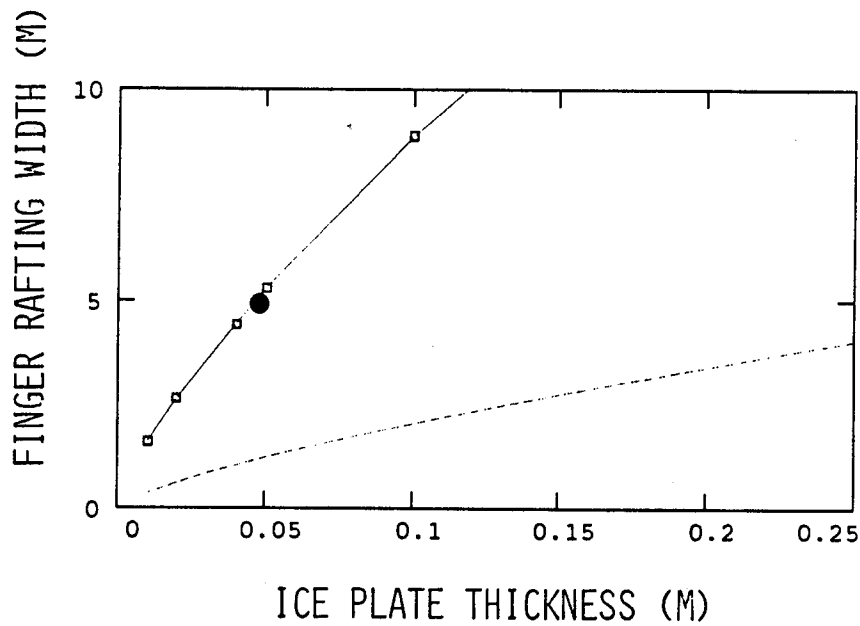
A**B**

Fig. 10.3 A) Calculated finger-rafting-width plotted as function of ice thickness. Solid line with open squares (Chamuel) and dashed line (Pritchard). B) Expanded scale showing LEADEx Arctic field data point by Morrison (solid black circle).

match hard-ice had little effect on the predicted finger-width values. For example, the predicted finger-raftering width for 1 m thick ice changed only from 50 m to 51 m as the above ice properties were replaced with corresponding hard-ice elastic properties.

An empirical equation was obtained to approximate the theoretical results relating the calculated finger-width W to ice thickness H :

$$W = 98 H^{0.74}$$

Fig. 10.4 compares the empirical and theoretical results. Finger-raftering is difficult to simulate in the laboratory using a scale model. Ice fracture in the Arctic depends on the unique properties of sea ice at the natural scale.

10.3 Conclusions

A preliminary study was conducted to provide physical insight into the formation process relating finger-raftering width to ice plate thickness. Theoretical results were obtained based on the assumption that maximum coupling between flexural waves and water gravity waves occur when their phase speeds are identical. The theoretical results were compared to other theoretical and field results.

Fundamental theoretical, field, and laboratory studies on sea ice finger-raftering are needed to complement the preliminary investigations conducted so far. Future laboratory experimental studies will characterize the action of coupled flexural waves and gravity waves in adjacent finite flexible floating plates.

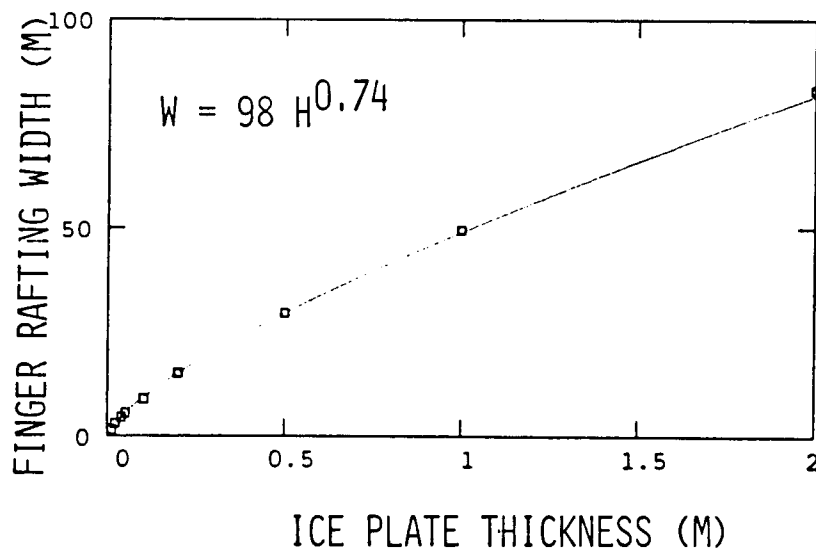


Fig. 10.4 Comparison of empirical (solid line) and theoretical (open squares) results.

10.4 References

- [10.1] W. F. Weeks and D. L. Anderson, "Sea ice thrust structures," *J. Glaciology* 3(23), 173-175 (1958).
- [10.2] J. F. Holmes and L. V. Worthington, *Oceanographic Studies on Project Skijump II*. Woodshole Oceanographic Institution, Technical Report, Ref. No. 53-23 (1953). NTIS accession No. AD11-348.
- [10.3] M. Dunbar, "Thrust Structures in Young Sea Ice," *J. Glaciology* 3(28), 727-732 (1960).
- [10.4] J. N. Weber, "Ice Thrust Structures," *J. Glaciology*, 3(24), p. 291 (1958).
- [10.5] J. C. Green, "Finger-rafting in fresh-water ice: Observations in Lake Superior," *J. Glaciology* 9(57), 401-404 (1970).
- [10.6] M. Dunbar, "Note on the formation process of thrust structures in young sea ice," *J. Glaciology* 4(32), 147-150 (1962).
- [10.7] R. S. Pritchard, "Modeling sea ice failure mechanisms", in J. Fondrk and K. Dillard, *Office of Naval Research Arctic Sciences Program Research Summaries 1992*, ONR Report No. OCNR 1125AR93-10, May 1993, pp. 68-70.
- [10.8] J. R. Chamuel, "Progress Report No. 10 / ONR Contract No. N00014-92-C-0028," Sonoquest Advanced Ultrasonics Research, Wellesley Hills, Massachusetts, document No. JRC-26-94, August 1994.
- [10.9] W. M. Ewing, W. S. Jardetsky, and F. Press, *Elastic Waves in Layered Media*, McGraw-Hill Book Co., N. Y. (1957).

SUMMARY

This report is the third in a series of publications by the author [5.5, 5.13], presenting a new collection of ultrasonic modeling findings obtained under controlled conditions on various fundamental liquid/solid seismoacoustic wave phenomena. Quantitative ultrasonic modeling results were described contributing to the physical understanding of different fundamental problems related to low-frequency seismoacoustic wave phenomena resulting from the interaction of underwater acoustic waves with penetrable heterogeneous solid boundaries. The new findings were summarized in ten independent sections covering a wide range of problems:

- 1) Backscattering of Scholte waves and grazing underwater acoustic waves by a trench at a liquid/solid interface.
- 2) Explanation for observed underwater acoustic backscatter from the Canada Basin near 73.2°N, 139°W where recent bathymetric charts do not reveal the existence of large bathymetric highs nearby.
- 3) Effect of a thin low-velocity layer underneath a floating plate on flexural wave dispersion.
- 4) Effect of viscous waves from suspended particles in a thin layer under sea ice on low-frequency underwater acoustic wave reflectivity.
- 5) Comparison of experimental and theoretical results on the dispersion of antisymmetric edge waves along apex of truncated elastic wedge.
- 6) Wave propagation along apex of free and immersed elastic wedges with range-dependent apex angle and cross section.
- 7) Shear wave coupling to ice cores.
- 8) Ultrasonic characterization of sea ice cores.
- 9) Monostatic seismic profiling using scattering from 45° oblique cylindrical hole in ice plate using one compressional transducer.
- 10) Sea ice finger-rafting and ice thickness.

The generic findings presented are applicable to the fields of underwater acoustics, acoustical oceanography, seismology, nondestructive testing, acoustoelectronic sensors, acoustic imaging, and noise reduction.